InAsSb/InAs STRAIN BALANCED SUPERLATTICES FOR PHOTODETECTOR APPLICATIONS

by

David Lackner

Dipl. Phys., Philipps Universität Marburg, 2006

THESIS SUBMITTED IN PARTIAL FULFILLMENT

OF THE REQUIREMENTS FOR THE DEGREE OF

DOCTOR OF PHILOSOPHY

IN THE

DEPARTMENT OF PHYSICS

FACULTY OF SCIENCE

SIMON FRASER UNIVERSITY

Fall 2011

APPROVAL

Name: David Lackner

Degree: Doctor of Philosophy

Title of Thesis: InAsSb/InAs Strain Balanced Superlattices for Photodetector Applications

Examining Committee: Dr. J. Steven Dodge (Chair)

Dr. Simon P. Watkins (Senior Supervisor)
Professor, Department of Physics

Dr. Patricia M. Mooney (Senior Supervisor)
Professor, Department of Physics

Dr. Michael L.W. Thewalt (Supervisor)
Professor, Department of Physics

Dr. George Kirczenow (Internal Examiner)
Professor, Department of Physics

Dr. Matthew Johnson (External Examiner)
Professor, Department of Physics and
Astronomy, University of Oklahoma

Date Approved: September 6^{th}, 2011

Declaration of
Partial Copyright Licence

Abstract

Lately, significant research efforts have been directed towards finding III-V alternatives for HgCdTe infrared detectors for optical gas sensing as well as night and machine vision applications. Despite the advantages of HgCdTe, including a tunable bandgap between 1–30 μm and a high optical absorption coefficient, difficulties in producing uniform material, which are limiting the size of detector arrays and leading to low yield, combined with challenging epitaxial growth and device processing keeps the technology expensive. Recently InAs/Ga(In)Sb type II short period superlattice detectors with cutoff wavelengths between 3 and 30 μm have been reported. However, these devices all rely on molecular beam epitaxy for the epitaxial growth, as InAs/(In)GaSb short period superlattices of high quality are extremely challenging to realize by organometallic vapour phase epitaxy (OMVPE). OMVPE growth is desirable since it is very suitable for high volume production, which would lead to a significant cost reduction. Thus we have proposed an InAsSb/InAs strain balanced superlattice detector design grown on GaSb, which is more suitable for OMVPE growth. In this thesis, structural and photoluminescence measurements of InAsSb/InAs superlattices are presented for Sb compositions between 4% and 27%. The layer structures were simulated with a state of the art electronic structure calculator based on a self consistent Poisson and Schroedinger equation solver that includes strain and band-offsets. The calculated transition energies were compared with the measured data. For the first time, the theoretically predicted type IIb alignment, where the InAs conduction band is below the InAsSb conduction band, was confirmed experimentally. The parameters obtained from the simulations were then used to predict the type II transition energies of InAsSb/InAs strain balanced superlattice absorber structures at 77 K for different compositions and periods. The optical matrix element was calculated and compared with that of InAs/(In)GaSb superlattices. The InAsSb/InAs structures can be designed with optical matrix elements

that are higher or equal to those of the more well established InAs/Ga(In)Sb superlattices. Finally, initial optical response data of an unoptimized strain balanced $InAs_{0.79}Sb_{0.21}$/InAs detector is shown. Its cutoff wavelength of 8.5 μm (0.15 eV) is in good agreement with the predicted type II transition energy.

Dedication

to my family

Acknowledgments

I would like to thank my senior supervisors Prof. Simon Watkins and Prof. Patricia Mooney for making this work possible, their support and guidance throughout the years.

Dr. Oliver Pitts deserves my gratitude, as he had worked on this project before I started, and was always a great resource when I had questions in the lab during the time we worked together on this project. He also succeeded in growing the InPSb layers which were presented in the thesis. Some initial growth experiments regarding this project were also carried out by Dr. Simin Najmi before my arrival. Prof. Michael Thewalt and his graduate students, Dr. Albion Yang and Michael Steger, measured all of the photoluminescence spectra included in this work and also worked tirelessly until I had no more detector samples to measure the response of. Also I would like to thank Prof. Michael Thewalt for helping me make sense of the optical data. Michael Steger was not only involved in taking all the optical measurements at SFU, he was also always a great source for solving LaTex problems and is a great friend which I appreciate. Dr. Alberto Basile introduced me to nextnano and was always happy to discuss device physics or anything else over a cup of coffee. Dr. Karen Kavanagh supervised the collection of the STEM data. She was also always very open for discussing the results. Milena Martine, an undergraduate student, did some of the electrical measurements presented in the n-N heterojunction chapter and was initially involved in finding a process to make "homebuilt" chip-carriers for detector measurements. Undergraduates Pawn Sandhu and Mark Xu set up the homebuilt *in situ* strain monitoring tool before my time in this lab. I also would like to thank Dr. George Kirczenow for helpful discussions regarding the calculation of the optical matrix elements.

This work would not have been possible without collaborations outside of the SFU Physics department. The research proposal was initiated by Dr. C.R. Bolognesi who at the time was a Professor in the School of Engineering Sciences, unfortunately he had left SFU

by the time I arrived. Dr. Tom Cherng (4D labs SFU) processed and taught me how to process the detector devices at SFU, while Dr. Elena Plis of the University of New Mexico also processed, and measured devices of mine electrically and optically. Also I would like to thank Y. Wang at the London Centre for Nanotechnology of the Imperial College London for taking some of the STEM images.

Finally I would like to thank my parents and my grandmother for their ongoing support. Especially I want to thank my wife Melanie who has accompanied me half way around the globe and back and who had to do without my presence during the long hours of writing this thesis.

Contents

List of Tables

List of Figures

Chapter 1

Introduction

The goal of this thesis was to develop a III-V photodetector based on InAsSb as an alternative to HgCdTe (MCT) infrared detectors at wavelengths between 2 and 20 μm. Most environmentally interesting gases e.g. CO, CO_2, O_3, NO_x, CH_4, C_2H_6 [1] have their so called spectroscopic fingerprint in this region and therefore, their concentration can be measured optically. Further at 3 to 5 μm and 8 to 12 μm there are atmospheric transmission windows. These regions can be used for long range communication and astronomy. Another major application is thermal imaging, for which multicolor focal plane arrays are desired.

MCT is an almost ideal material system for photo-detection. The band gap can be tailored to fit the entire 1–30 μm range while the Cd(Zn)Te substrate is almost lattice matched over the whole composition range (see Fig 1.1). Further, MCT has a large optical coefficient which leads to strong absorption [2]. However, difficulties in producing uniform material, which limits the size of detector arrays and leads to low yield, challenging material epitaxy and device processing, and excess dark currents due to band to band tunneling are drawbacks of this material system [3]. In addition, the high cost of the substrate material keeps the technology expensive. Thus, research towards less expensive alternative systems is in progress. Suggested techniques include quantum well detectors (intra- and interband) and quantum dot detectors. An extensive review of the different concepts can be found in [2].

Recently significant progress has been reported on InAs/Ga(In)Sb type II short period quantum well detectors. This detector type was proposed in 1987 by Smith and Mailhiot [5]. Thin quantum wells of InAs and Ga(In)Sb are grown as a superlattice stack on a GaSb wafer. InAs and GaSb form a type II band alignment (see Fig 1.2), so that the

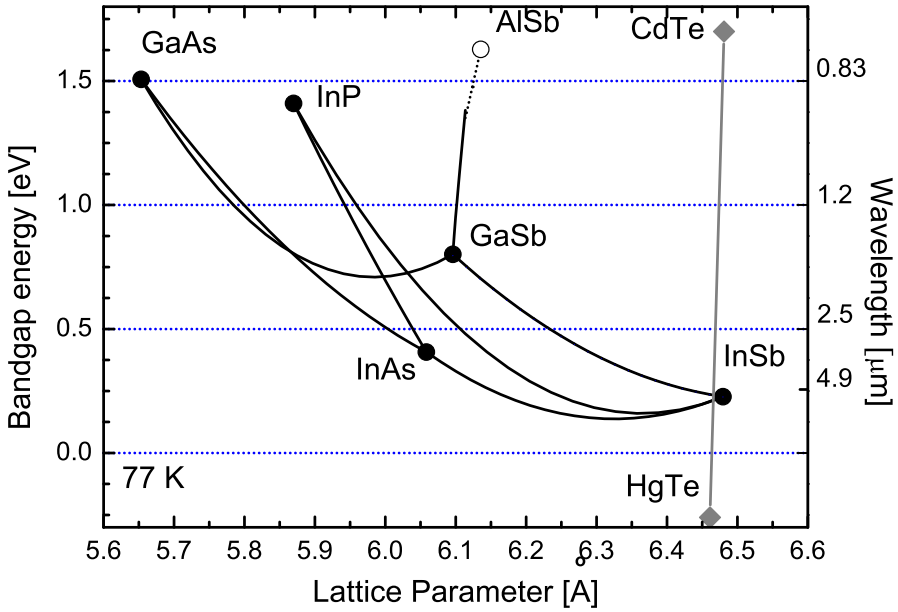

Figure 1.1: Γ-point energy gap as a function of lattice parameter for selected III-V binaries and their ternary alloys at 77 K. Solid (open) symbols and solid (dotted) lines mark direct (indirect) band gap semiconductors. Every line connecting two symbols refers to the alloy made from the binary constituents at both end points. The lattice parameter is assumed to be linearly dependent on the alloy composition (Vegard's law). For the band gap energy a quadratic correction to the linear dependence is found, referred to as band gap bowing. Data are taken from Ref. [4] with the exception of MCT data which are from Ref. [2].

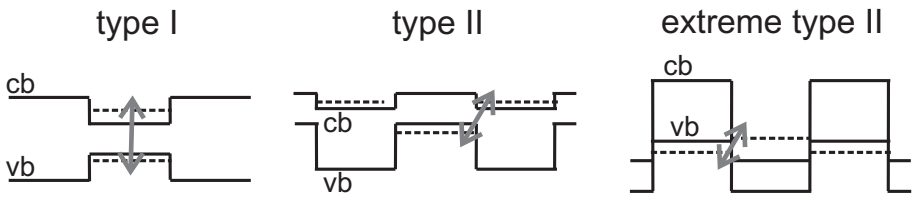

Figure 1.2: Schematic diagrams of type I and type II band offsets. The arrows mark the lowest optical transition, which is spatially indirect for a type II band alignment. Due to the confinement of the carriers, the energy levels in the wells are shifted and the ground state energy levels are shown (dashed line).

lowest conduction band to highest valence band transition, which is spatially indirect, is smaller than the band gap of any of the constituents. In this case, the alignment is extreme and due to the large band offsets, the conduction band of InAs is below the valence band of GaSb. A positive gap is only formed when growing thin layers, due to quantum confinement which shifts the energy levels. In fact, by controlling the quantum well width, the cutoff wavelength can be tuned and detectors with cutoff wavelengths between 3 and 30 μm have been demonstrated. Recently detectivities as high as MCT have been reported for a cutoff wavelength of 8.6 μm operating at 80 K [6]. Excellent spectral homogeneity across a whole wafer can be achieved [3] and certain designs have been developed for operation at room temperature [7].

Most of this progress has been made using molecular beam epitaxy (MBE), since it is very challenging to grow the monolayer interfaces needed for strain balancing by organometallic vapour phase epitaxy (OMVPE) [9]. OMVPE growth technology is desirable, since it has the advantage of higher volume production than MBE and thus the cost advantage, compared to MCT technology, would be improved significantly. We have proposed another V-III system based on InAs/InAsSb superlattices (SLs) [10], which is more suitable for OMVPE growth [9] but also much less explored. This system can be grown strain balanced on GaSb. It is possible to grow thick absorber stacks without the crystal degrading defects from strain relaxation. This work explores initial steps towards such a detector technology.

InAsSb, an alloy between InAs and InSb, has the lowest band gap of any III-V materials (see Fig 1.1) with a band gap of 0.14 eV (8.9 μm) for a composition of $InAs_{0.37}Sb_{0.63}$ [11].

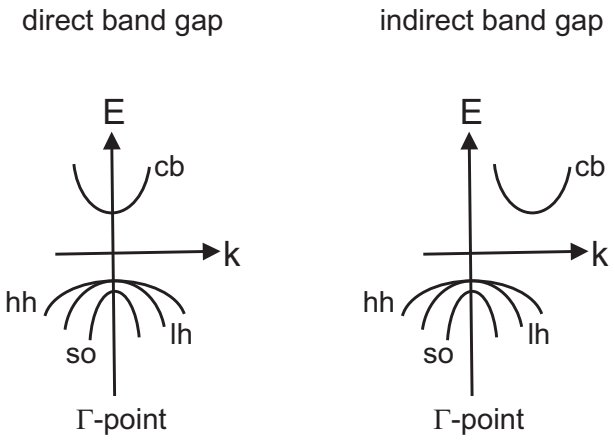

Figure 1.3: Schematic of the lowest conduction band (cb) and the three highest valence bands, heavy hole (hh), light hole (lh) and split off band (so), in zincblende semiconductors. For direct band gap semiconductors including GaAs, GaSb, InAs, InSb, the maximum of the valence band is at the same k-space position as the minimum of the conduction band, while for indirect band gap semiconductors like Si, the minima and maxima are at different k-space positions.

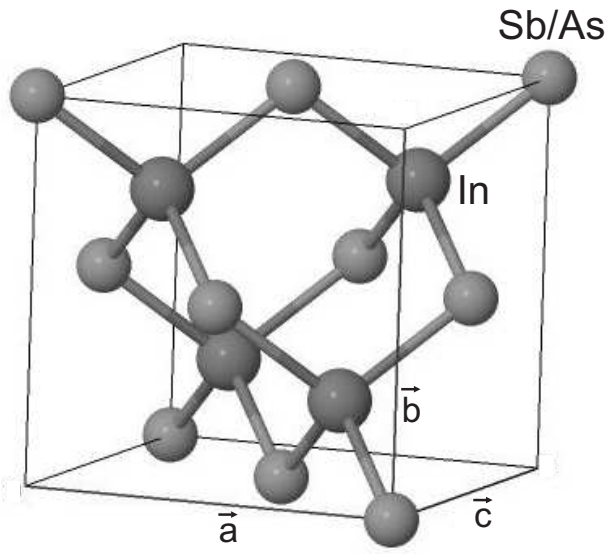

Figure 1.4: Schematic of InAs and InAsSb zincblende crystal structure. Without strain $|\vec{a}|$ = $|\vec{b}|$ = $|\vec{c}|$ and this length is called the lattice parameter. The 3D-schematic was created with Jmol [8].

Unfortunately there is no substrate with a small enough lattice mismatch, that thick absorber layers with this composition can be grown upon without introducing a significant density of misfit dislocations due to strain relaxation (see Fig 1.1). Thus, in the proposed design, InAs and InAsSb layers were alternated to form a strain balanced superlattice on GaSb substrates. The band offset is type II, as shown in this work, so that the lowest optical transition is smaller than the band gap of any of the constituents (see Fig 1.2). InAs, InSb and their alloys are direct band gap semiconductors, which means that the lowest conduction band minimum and the highest valence band maximum are aligned in k-space at **k**=0. This is schematically depicted in Fig 1.3.

The crystal exhibits a zincblende structure (illustrated in Fig 1.4), where the atoms of the two species (group III & V) occupy the lattice sites of two face centered cubic (fcc) sublattices. The two sublattices have an offset of $(\frac{1}{4}, \frac{1}{4}, \frac{1}{4})a$, where a is the length of the unit cell of the crystal. In units of a, the first species occupies positions (0,0,0), (0,$\frac{1}{2}$, $\frac{1}{2}$), $(\frac{1}{2}, 0, \frac{1}{2})$ and $(\frac{1}{2}, \frac{1}{2}, 0)$ and the second species' coordinates are $(\frac{1}{4}, \frac{1}{4}, \frac{1}{4})$, $(\frac{1}{4}, \frac{3}{4}, \frac{3}{4})$, $(\frac{3}{4}, \frac{1}{4}, \frac{3}{4})$ and $(\frac{3}{4}, \frac{3}{4}, \frac{1}{4})$ in one unit cell.

Fig 1.5 displays structures that were grown within the development process. Initially simple bulk structures were grown on GaSb and InAs substrates (Fig 1.5a) where different growth parameters were tested to optimize structural properties like surface roughness and X-ray diffraction peak width or conduct transmission electron microscopy investigations. Fig 1.5b shows the structure grown for the n-n heterojunction experiments. A lightly n-doped InAsSb layer lattice matched to the n-GaSb substrate was grown on top of an n-GaSb layer. The doping level of this layer changed for different samples and the electrical behaviour of this heterojunction was studied as a function of GaSb doping level. In the proposed detector design (Fig 1.5f), electrical contact on one side is made through the GaSb substrate. So the work on these structures was to prove that a low resistance contact between the two layers can be made and how. Then superlattice and multi-quantum well test structures were grown and structural as well as optical properties were measured and optimized (Fig 1.5a). Bulk p-n detector structures (Fig 1.5c), with a working principle based on the photovoltaic effect, were made to test the fabrication process and basic diode properties on the most simple structures. These structures were then compared to the phosphorous based heterojunction approach (Fig 1.5d), again as a simpler building block for the final structure. After having studied the optical properties and developed a growth process for the superlattices, the absorber layer of the simple homojunction design was exchanged for a superlattice absorber as shown in (Fig 1.5e). The final design (Fig 1.5f) includes an n-type InAsSb/InAs strain balanced superlattice absorber grown on an n-type GaSb wafer. The p-doped top layer, to complete the p-n junction, is made of InPSb which is lattice matched to the substrate. Unfortunately the final design could not be realized so far. The details and the results obtained at the various stages of the thesis are discussed in the remaining chapters as follows: Chapter 2 gives brief introductions to the main experimental techniques used to grow the samples and characterize epitaxial layers and devices and the interpretation of the data. Chapter 3 describes the challenges of the growth and doping of InAsSb and introduces a theory to calculate the critical layer thickness for heteroepitaxy. Chapter 4 includes an electrical and optical study of the n-InAsSb/n-GaSb heterojunctions (see Fig 1.5b), where it was found that the doping level of the GaSb layer has strong effects on the current-voltage (I-V) characteristics due to the large band offsets. The I-V characteristics can be tuned from rectifying to ohmic behaviour by varying the doping level of the GaSb. This is important knowledge for device design, as a rectifying junction at this

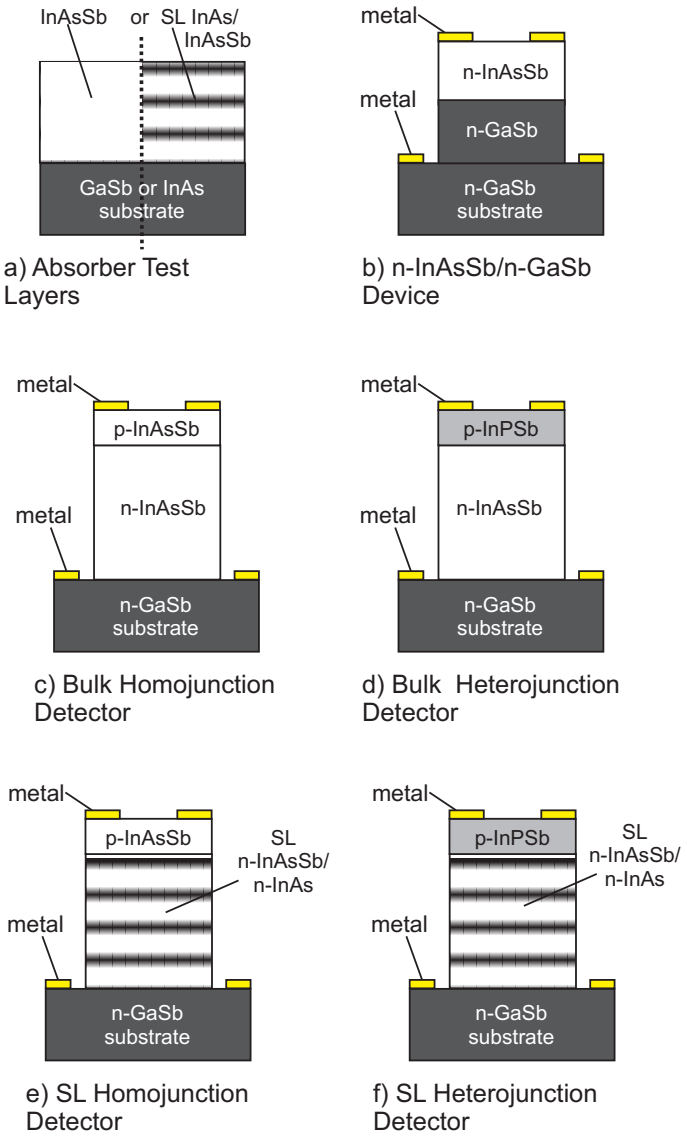

Figure 1.5: Schematic of the different stages of the detector development. Part f) shows the proposed design, that was not realized yet. Parts a) to e) show the milestones towards the ideal design as discussed in this work. Note that part a) describes four different structures: bulk layers grown on either on GaSb or InAs substrates and superlattice or quantum well structures deposited either on GaSb or InAs substrates.

interface is unwanted. Chapter 5 introduces the concept of strain balancing used in this work, followed by an introduction to the "solid-model theory" that can be used to calculate band offsets of strained semiconductors in heteroepitaxy. Those results are then compared to low temperature photoluminescence (PL) results from strain balanced multi-quantum wells. One set of parameters was found that describes the PL transition for all compositions measured and structures grown on InAs and GaSb wafers (see Fig 1.5a). In chapter 6 these parameters are used to predict the cutoff wavelength of superlattice detectors at 77 K as well as the optical matrix element as a figure of merit of the expected absorption. These results can be used as a design guide for future work. The optical response of "bulk" homojunction, InPSb/InAsSb bulk heterojunction and strain balanced superlattice (SL) homojunction detectors are presented (1.5c–e). The thesis is then summarized and a short discussion of possible future directions of this project is given.

Chapter 2

Experimental Methods

2.1 Organometallic Vapour Phase Epitaxy

Organometallic vapour phase epitaxy[1] (OMVPE) is a commonly used technique to grow thin epitaxial films on a single crystal substrate. With this technique, the species to be grown are supplied in the gas phase in the form of organometallic compounds, the precursors, and streamed over a heated substrate to form epitaxial layers.

The OMVPE reactor used for this work is a Thomas Swan (Cambridge, UK) reactor built in 1993. The reactor chamber has been refitted to a stainless steel vertical showerhead design.

In OMVPE, the sources are organometallic chemicals, usually in the liquid state and are stored in stainless steel containers called bubblers. The bubblers are placed in temperature controlled baths. An inert H_2 carrier gas[2] is "bubbled" through the precursor (see Fig 2.1). Thus, the carrier gas is enriched with the vapour of the precursor and together with the carrier gas they flow into the reactor. Inside the reactor, the gases flow laminarly over the susceptor, which is a graphite block that can be heated. The susceptor also contains the substrate holder, which can be rotated during growth to achieve homogeneous deposition. Chemicals that are not deposited are pumped into the exhaust-gas cleaning system, the so called scrubber. Gas monitoring inside the exhaust-pipe downstream of the scrubber verifies that no dangerous or toxic chemicals penetrate into the environment. The OMVPE

[1] also called metal-organic vapour phase epitaxy (MOVPE)

[2] The carrier gas needs to be extremely clean. The H_2 used is especially cleaned to be 99.99999% pure.

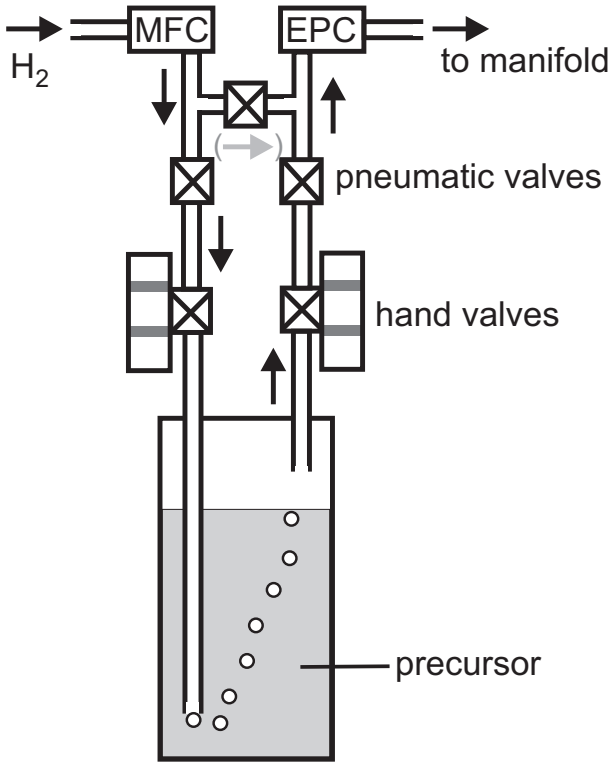

Figure 2.1: Schematic drawing of a bubbler. The H_2 flow through the bubbler is controlled by the mass flow controller (MFC) while the electronic pressure controller (EPC) downstream of the bubbler keeps the pressure in the bubbler constant.

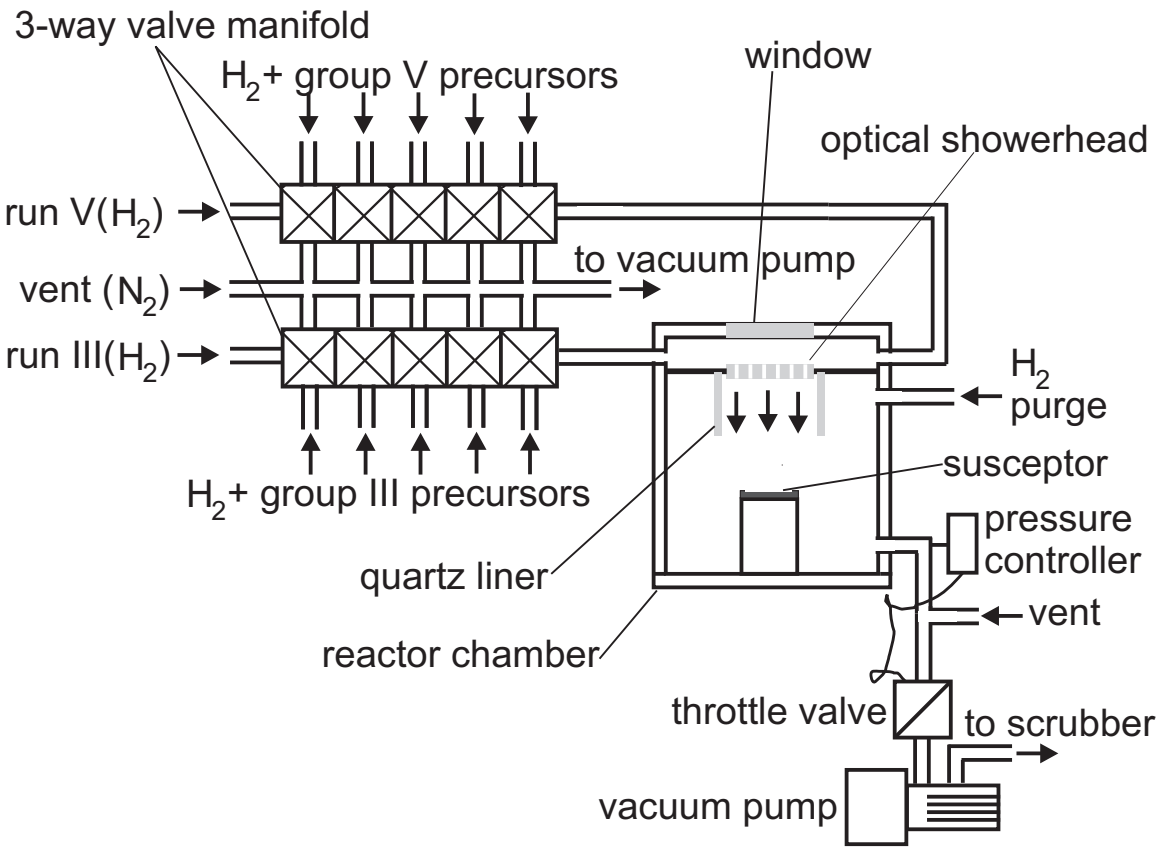

Figure 2.2: Schematic drawing of the OMVPE reactor (not to scale).

reactor is schematically drawn in fig 2.2. In order to reduce unwanted prereactions in the gas phase, the group V and group III sources have separate run lines and are only mixed in the small volume above the optical showerhead immediately before being streamed over the heated substrate. The pressure in the reactor chamber is controlled via the position of the throttle valve. In this machine a standard reactor pressure of 50 Torr was maintained during growth.

The temperature was monitored optically via a pyrometer on the backside of the susceptor and automatically controlled. This measurement was calibrated after every susceptor cleaning by inserting a thermocouple probe which was placed in physical contact on the top and center of the susceptor, while the reactor was held under standard growth conditions.

The window on the top of the reactor and the glass showerhead allows optical *in situ*

measurements to be performed during growth. The systems available on this machine are a homebuilt system to measure wafer curvature and reflectance in real time and a reflectance difference spectroscopy (RDS) unit. Unfortunately both systems can only be used when the susceptor rotation is turned off. The "optical showerhead" growth chamber was designed at SFU and details can be found in Ref. [12].

In this work, the precursors trimethylindium (TMIn), triethylgallium (TEGa) for In and Ga are used on the group III side, while tertiarybutylarsine (TBAs), trimethylantimony (TMSb) and tertiarybutylphosphine (TBP) were used for the group V elements As, Sb and P. For p-doping a diethylzinc (DEZn) source was used, while diethyltellurium (DETe) was used for n-doping. The chemical formulae of the precursors are listed in Table 2.1.

The mass flow rate of the precursor is controlled by the flow of hydrogen gas through the bubbler, as well as by the total gas pressure in the bubbler. The flow after the bubbler Q_{out} is

$$Q_{out} = Q_s + Q_{prec} \tag{2.1}$$

where Q_s is the amount of H_2 flowing into the bubbler and Q_{prec} denotes the amount of the precursor that has been picked up by the carrier gas. Of course, the amount of Q_{prec} within Q_s has to be proportional to the vapour pressure of the precursor (P_s). When the pressure in the bubbler is controlled to be P_{PC} one finds:

$$\begin{aligned} \frac{Q_{prec}}{Q_{out}} &= \frac{P_s}{P_{PC}} \\ \text{and therefore} \qquad Q_{out} &= Q_{prec}\frac{P_{PC}}{P_s} \quad . \end{aligned} \tag{2.2}$$

After inserting Eqn. (2.2) into Eqn. (2.1) one finds:

$$Q_{prec} = Q_s\frac{P_s}{P_{PC} - P_s} \tag{2.3}$$

In the growth chamber, the partial pressure of the precursor P_p and reactor pressure P_r has to equal the fraction of the precursor and the total flux to through the reactor (Q_{total}):

$$\frac{P_p}{P_r} = \frac{Q_{prec}}{Q_{total}} \quad . \tag{2.4}$$

After inserting Q_{prec} from Eqn. (2.3) into the above expression, one finds P_p as a function of Q_s and P_{PC}:

$$P_p = \frac{Q_s}{Q_{total}}\,\frac{P_s}{P_{PC} - P_s}P_r \quad . \tag{2.5}$$

abbreviation	name	chem. formula	MP [°C]	BP [°C]	a	b [K]
TEGa	triethylgallium	$(C_2H_5)_3Ga$	-82	143	8.083	2162
TMIn	trimethylindium	$(CH_3)_3In$	88.4	133.8	10.52	3014
TBAs	tertiarybutylarsine	t-$(C_3H_9)AsH_2$	-1	68	7.243	1509
TMSb	trimethylantimony	$(CH_3)_3Sb$	-87	80	7.707	1697
TBP	tertiarybutylphosphine	t-$(C_3H_9)PH_2$	4	54	7.713	1539
DEZn	diethylzinc	$(C_2H_5)_2Zn$	-30	117.6	8.280	2109
DETe	diethyltellurium	$(C_2H_5)_2Te$	N/A	137	7.99	2093

Table 2.1: OMVPE precursors used in this work. MP is the melting point and BP refers to the boiling point. The data is collected from the manufacturers product specification sheets. The coefficients a and b are measured and used to calculate the vapour pressure as a function of the temperature as defined in Eqn. 2.6

The vapour pressure can only be controlled indirectly by the temperature of the precursor, which implies that the temperature of the bubbler during an epi-run has to be carefully controlled. This is achieved by liquid temperature baths. The vapour pressure of the precursor is related to the temperature of the chemical via the empirical relation:

$$\log(P_s) = a - \frac{b}{T} \qquad (P_s[\mathrm{Torr}], T[\mathrm{K}]). \tag{2.6}$$

The coefficients a and b for the chemicals used in this work are listed in Tab 2.1.

A sketch of a bubbler is shown in Fig 2.1. All OMVPE precursors were kept in bubblers with the exception of DETe. It was used as a n-doping source and was supplied as a dilute mixture with H_2 from a pressurized gas tank.

2.1.1 OMVPE Crystal Growth

The precursors mixed with the carrier gas are streamed over the heated substrate, ideally in a laminar flow. Close to the interface, in the so called boundary layer, the gas velocity is close to zero and the molecules can diffuse to the surface. As the molecules approach the surface, they are heated and undergo pyrolysis - decomposing into their constituents. The growth species then form the epitaxial layer while leaving organic radicals behind. According to Stringfellow [13] a number of reactions can occur for different precursors. However, most of the pyrolysis reactions can be classified as one of the two types: "homolytic fission" or "β-hydride elimination", which are shown for the example of TMSb and TEGa in Fig 2.3. The exact nature of pyrolysis for some precursors, including TBAs, varies with growth conditions, since all the other precursors in the reactor as well as the heated substrate can have catalytic effects on the pyrolysis of certain precursor molecules [14].

After or during pyrolysis, the metal atoms or molecules physisorb on the surface of the heated substrate. The surface consists of terraces as no substrate is atomically flat along the full surface of the wafer. This statement can be proven by thermodynamic arguments [15], however in real wafers most steps are due to un-intentional or intentional miscuts and crystal defects. The adsorbed atoms (adatoms) are only weakly bound and can migrate over the surface until they are either desorbed back into the gas phase or are incorporated into the crystal. The preferred places for adatoms to bind to the crystal are steps or kinks, since they offer more reactive binding sites (see Fig 2.4). Thus the terraces grow until they reach the

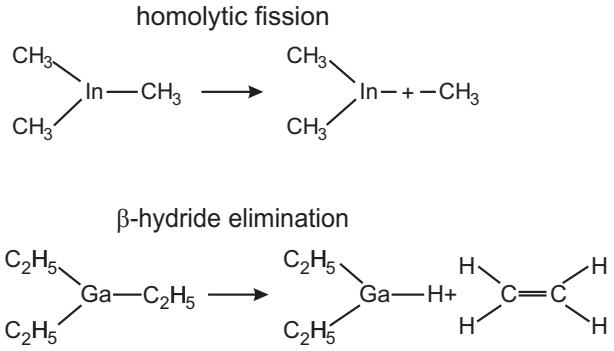

Figure 2.3: Homolytic fission and β-hydride elimination of TMIn and TEGa are shown as examples for pyrolysis reactions.

end of the wafer or merge with another step. This model is called “step flow growth” and produces smooth epitaxial layers. A detailed treatment of the growth of crystals is given in Ref [15].

The growth rate in an OMVPE reactor is determined by different factors at different temperatures: At low temperatures, the reaction kinetics close to or at the surface, where the precursor molecules have to be converted into the group III and V radicals to be incorporated into the crystal are limiting the growth. Since the decomposition of the precursors follows an exponential law until the temperature is above the temperature, where all precursors are fully decomposed, an exponential temperature dependence of the growth rate for low temperatures is found. At higher temperatures, usually between $550°\mathrm{C}$ and $750°\mathrm{C}$, the limiting factor is the amount of precursor transported through the boundary layer to the growth surface (mass transport regime). The driving mechanism here is diffusion. At the growth surface, the chemicals are adsorbed onto and incorporated into the crystal and thus their concentration in the gas-phase is reduced compared to outside of the boundary layer. This composition gradient drives diffusion through the boundary layer to the substrate surface. Since the diffusion process has only a weak temperature dependence, there is only a weak or no temperature dependence on the growth rate. In this temperature regime the growth rate typically depends linearly on the group III flow rate. This is the region where OMVPE reactors are usually operated. After further increasing the temperature, more and more adsorbed atoms desorb from the substrate before being incorporated.

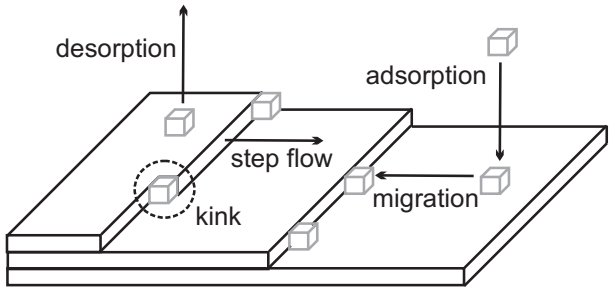

Figure 2.4: Epitaxial growth schematic. Group III and V species of the gas phase are adsorbed on the heated substrate surface. There they migrate and either desorb back to the gas phase or get incorporated into the crystal. Preferred incorporation sites are step edges or kinks. This growth mode is called step flow growth.

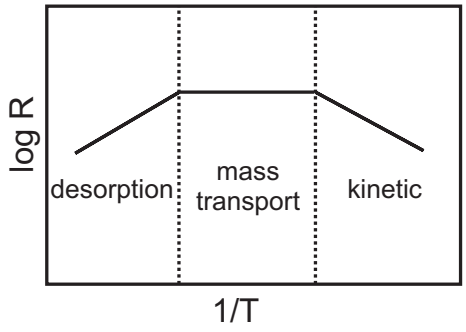

Figure 2.5: Schematic semi-logarithmic plot of growth rate as a function of inverse temperature. The three growth regimes are shown. Usually OMVPE reactors are used in the "mass transport" regime.

Thus, the growth rate decreases exponentially. Further, unwanted predeposition reactions like growth on the reactor sidewall and ceiling or particle formation can also occur and can be the reason for a decreased growth rate. The growth rate dependence on substrate temperature is schematically plotted in Fig 2.5.

Note that the group V species are more volatile (incongruent desorption) than the group III species and thus to grow a defect-free crystal the V/III ratio has to be equal or greater to unity. Usually it is chosen to be significantly higher. Arsenides like GaAs can be grown in a wide range of V/III ratios with decent crystal quality (1 to <100). However, for antimonides, a high V/III ratio leads to formation of Sb crystals on the wafer surface. This unwanted phase separation can occur for V/III ratios as low as 2 [16]. A more comprehensive treatment of the MOVPE process and the chemicals involved can be found in textbooks by Herman-Richter-Sitter [17] or G.B. Stringfellow [13].

2.2 High Resolution X-ray Diffraction

High resolution X-ray diffraction (HR-XRD) is a standard tool to analyze epitaxial films. It is used to gain information regarding the lattice mismatch and strain and thus the composition, in the case of ternary layers as well as the layer thickness. In the following sections the XRD diffraction techniques are presented. Then the equipment used for XRD measurements is introduced. This is followed by a practical introduction on how the collected spectra were analyzed.

2.2.1 X-ray Diffraction

Semiconductor crystals are periodic structures with a lattice spacing on the order of angstroms. In a similar way as light is diffracted by optical gratings, x-rays are diffracted by crystal lattices. The angles where maxima will occur due to constructive interference for a given wavelength (λ) is described by Bragg's law (see Fig. 2.6),

$$2d_{hkl}\sin\theta = n\lambda \tag{2.7}$$

where θ denotes the incidence angle and d_{hkl} the distance between the lattice planes having the Miller indices h, k, l and n is a positive integer. In cubic lattices, like most III-V

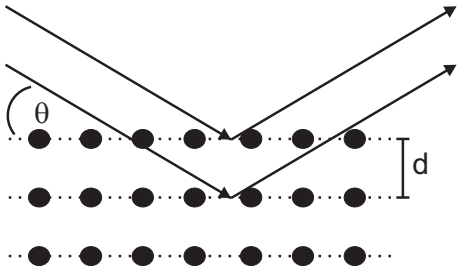

Figure 2.6: Schematic diagram of Bragg diffraction.

semiconductors, this distance is related to the lattice parameter (a) of the crystal by the relation [18]:

$$d_{hkl} = \frac{a}{\sqrt{h^2 + k^2 + l^2}} \tag{2.8}$$

The diffraction condition as described above can also be stated in reciprocal space coordinates. The reciprocal lattice vectors ($\vec{b_i}$) can be calculated from the lattice vectors ($\vec{a_i}$, see Fig 1.4) [18]:

$$\vec{b_i} = \frac{\vec{a_j} \times \vec{a_k}}{\vec{a_i} \cdot (\vec{a_j} \times \vec{a_k})} \tag{2.9}$$

The reciprocal lattice vector is defined here according the standard in crystallography, without the factor 2π, which is often included in solid state textbooks. Note that for zincblende crystals, $\vec{b_i}$ is parallel to $\vec{a_i}$ for all i.

In reciprocal space, the Laue condition, which is equivalent to Bragg's Law, Eq 2.7, states that peaks will only occur when the change in momentum of the diffracted x-ray beam ($\Delta\vec{k}$) is an integer multiple of the reciprocal lattice vector ($\vec{Q}$):

$$\Delta\vec{k} = \vec{k_f} - \vec{k_0} = \vec{Q} \qquad \text{with} \qquad \vec{Q} = h\vec{b_1} + k\vec{b_2} + l\vec{b_3}. \tag{2.10}$$

Since the reflection is elastic, the length of the reflected ($\vec{k_f}$) and the incident wavevector ($\vec{k_0}$) is the same:

$$||\vec{k_f}|| = ||\vec{k_0}|| = \frac{1}{\lambda} \tag{2.11}$$

Again the wave vector is defined without the factor 2π. The Laue condition is sketched in Fig 2.7.

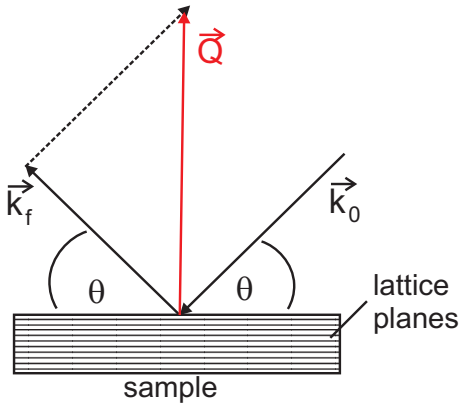

Figure 2.7: Schematic diagram of the Laue diffraction condition. Diffraction maxima only occur where the momentum difference of the incoming ($\vec{k}_0$) and outgoing wave-vector ($\vec{k}_f$) equals a reciprocal lattice vector ($\vec{Q}$).

2.2.2 X-ray Instrumentation

To conduct the HR-XRD measurements two machines were used: a Bede D3 triple axis diffractometer and a Panalytical XPert Pro system. The x-rays are generated with a high voltage source that accelerates electrons into a copper target. The rapid deceleration in the copper anode produces the broad "Bremsstrahlung" as well as the sharp characteristic lines due to electron transitions between energy levels of the inner shell in the atoms. For diffraction purposes, only the strongest line, the Cu $k_{\alpha 1}$ ($\lambda = 1.540598$ Å) of the spectrum is selected. The monochromator of the Bede D3 consists of two channel-cut Ge crystals with two asymmetric 220 reflections per crystal per channel. The Panalytical X'Pert pro system is fitted with a hybrid monochromator, consisting of a parabolic focussing mirror for high output power plus a two-bounce Ge monochromator crystal. The x-ray mirror is placed before the two Ge crystals, where the (220) asymmetric reflection is employed. Angular limiting apertures are usually also placed in the beam path to collimate the beam (see Fig 2.8). Elements that cut the beam width are called slits, while masks limit the beam height.

The sample is mounted strain free on the goniometer sample stage, where it can be rotated around ω, ϕ and ψ and moved in x-, y-, and z-directions (see Fig 2.8 and 2.9). These angles need to be aligned for every sample to perform a measurement. All x-ray

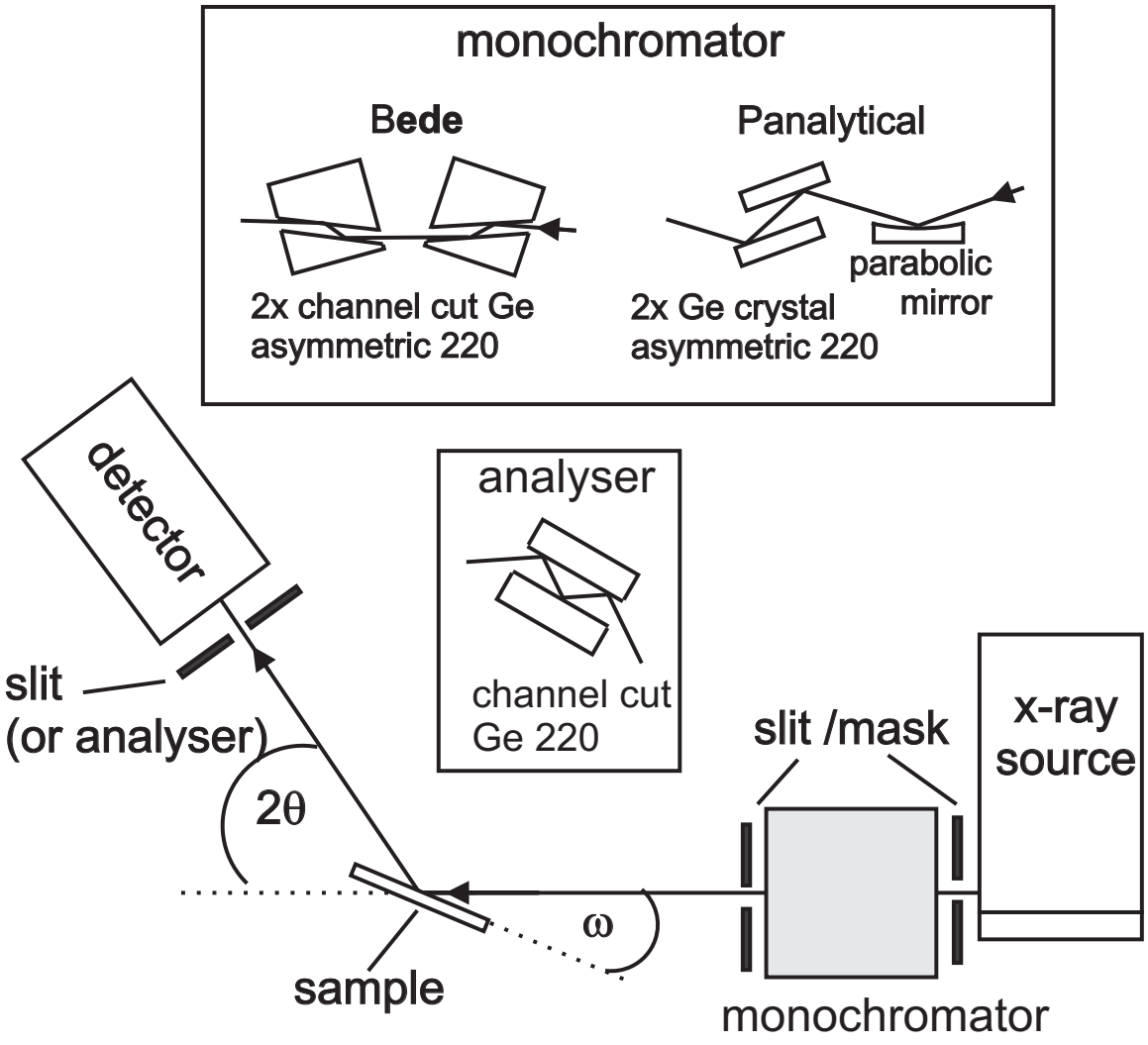

Figure 2.8: Schematic diagram of the high resolution x-ray diffractometer. The insets show details of the monochromator used on the different machines as well as the analyser crystal used for triple axis measurements.

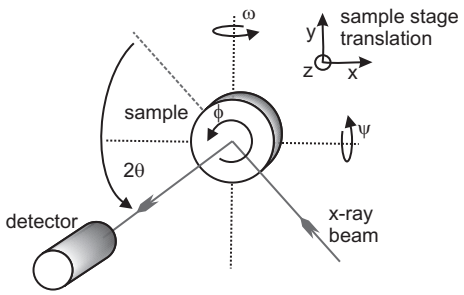

Figure 2.9: Schematic diagram of rotational and translational axis of the goniometer sample stage. ω and 2θ are rotations in the plane formed by the incident and reflected beams, and Ψ is a rotation perpendicular to this plane.

scans displayed in this thesis are $\omega - 2\theta$ scans. For such a measurement, ω, 2θ ψ and if needed ϕ, e.g for miscut wafers or asymmetric scans, are adjusted to give maximal intensity at the desired substrate peak, e.g. 004. Then ω is scanned over a certain angular range above and below the optimized position. At the same time, together with ω, θ is moved by twice the angle of ω. In this way, the weaker peaks due to the epilayer features are observed.

After diffraction from the sample, the scattered radiation is detected by an x-ray detector. In the Bede machine a scintillation detector is used, while Panalytical employs a proportional counter. Typically a 1 mm slit is mounted in front of the detector for rocking curve measurements on coherently strained samples, to suppress the background scattering. A triple bounce channel cut analyzer crystal (Ge 220) can be introduced into the beam path instead of the slit. This reduces the 2θ acceptance angle to 12 arcsec. This is done to eliminate broadening from mosaic effects. Mosaicity can occur when strain relieving misfit dislocations locally distort the lattice planes. Fig 2.10 shows x-ray measurements of the symmetric 004 reflection from an InAs substrate for the different machines and settings. The FWHM of the peak is lowest for the BEDE system (17 arcsec) due to the 2 double bounce channel cut monochromators. The FWHM of the InAs substrate measured with the X'Pert system is 29 arcsec and is reduced to 25 arcsec after substituting the detector slit with the analyser crystal. Measurements with the analyser crystal in place are often referred to as "triple axis scans" as opposed to "rocking curves", where there is only a slit or nothing in front of the detector.

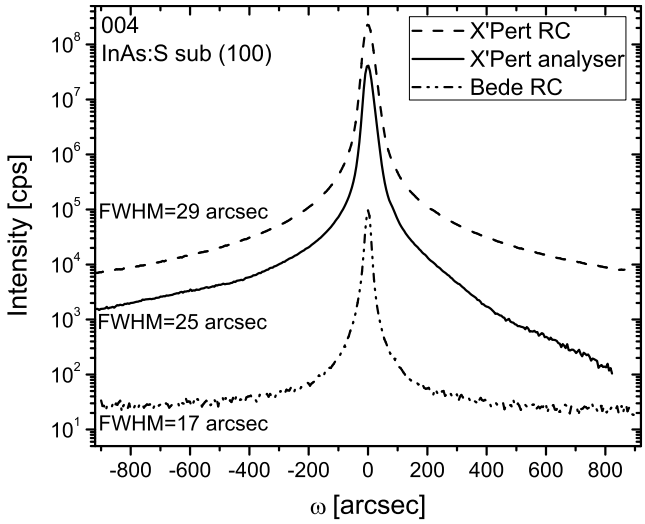

Figure 2.10: $\omega - 2\theta$ scan of the symmetric (004) reflection of a (100) InAs substrate with the two different machines. For the rocking curve measurements (RC) a 1 mm slit was placed in front of the detector. In the case of the scan denoted by analyser, the slit in front of the detector is replaced with an analyser crystal.

2.2.3 Rocking Curve Analysis

The following will give a short overview of how x-ray rocking curves can be interpreted with the kinematical theory as given by Bragg's law (Sec 2.2.1). Kinematical theory is purely based on geometrical considerations, while other effects like absorption are ignored. However, due to its simplicity it is easy to interpret for simple structures. A more general and especially detailed treatment can be found in Bowen and Tanner [19]. The approach of Ref. [19] on x-ray diffraction data analysis was followed below.

Ternary Layer Composition

X-ray diffraction can be used to measure the lattice parameter, and thus the composition, of a ternary heteroepitaxial layer and the layer thickness. In the following, for simplicity, an example of a GaInAs pseudomorphic (not relaxed) epitaxial layer on a GaAs (001) substrate is considered. In that case, the GaInAs lattice is compressively strained on the GaAs substrate (see Fig 2.11).

Using a symmetric reflection (e.g. 004), the spacing of lattice planes perpendicular to the growth direction i.e. the out of plane lattice constant ($a_\perp$) can be measured. In the case of GaInAs on GaAs, those will be spaced slightly larger than the substrate and a layer peak will appear on the negative side of the substrate peak in a relative scan (see fig 2.12). For small angle separations of layer and substrate peak, Bragg's law (Eqn 2.7) can be approximated to first order by taking the total derivative,

$$\begin{aligned} \Delta d \sin\theta + d\Delta\theta\cos\theta &= 0 \\ \text{therefore} \qquad \frac{\Delta d}{d} &= -\frac{\Delta\theta}{\tan\theta} \end{aligned} \tag{2.12}$$

where $\Delta\theta$ is the angle difference between the layer and the substrate peak, d is the substrate's lattice plane spacing of the chosen refraction condition and Δd the difference between the lattice plane spacings of layer and substrate. When the hkl indices values of both layer and substrate are the same, then $\Delta d/d$ is related to the lattice parameters due to Eqn 2.8 by

$$\frac{\Delta d}{d} = \frac{\Delta a}{a} = \frac{a_{L,\perp} - a_s}{a_s} \tag{2.13}$$

where $a_{L,\perp}$ is the lattice constant perpendicular to the surface of the layer, while a_s is the lattice constant of the substrate.

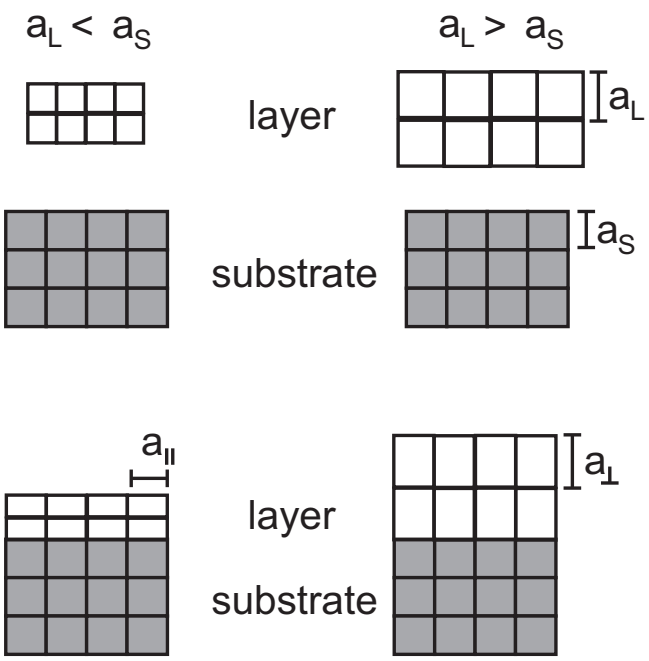

Figure 2.11: Schematic diagram of tensile and compressively strained heteroepitaxial layers.

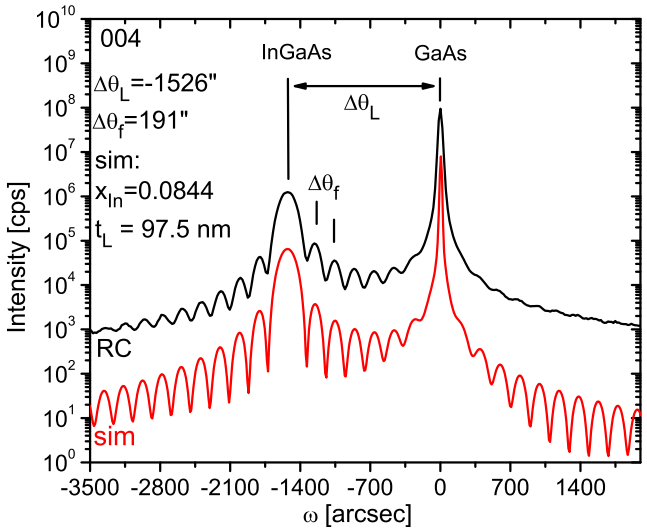

Figure 2.12: (004) $\omega - 2\theta$ scan of an InGaAs layer on a GaAs (100) substrate.

Parameter	GaAs	AlAs	InAs	InSb	GaSb
a [Å]	5.65325	5.6611	6.0583	6.4794	6.0959
c_{11} [GPa]	1221	1250	832.9	684.7	884.2
c_{12} [GPa]	566	534	452.6	373.5	402.6

Table 2.2: Elastic constants and lattice parameters at 300 K for selected III-V materials. Values taken from [4]

In the given example, the epitaxial layer is 100% strained (see Fig 2.11), which means that the lattice constant of the layer parallel to the surface ($a_{L,\|}$) is equal to a_s, which is the definition of pseudomorphic growth:

$$a_{L,\|} = a_s \tag{2.14}$$

To calculate the unstrained lattice parameter of the layer (a_L) the Poisson ratio of the material (σ_0), which is the ratio of the fraction of the expansion (compression) of the layer lattice parameter perpendicular to the growth surface divided by the compression (expansion) in a direction parallel to the growth surface:

$$\sigma_0 = -\left(\frac{a_{L,\perp} - a_L}{a_L}\right)\left(\frac{a_{L,||} - a_L}{a_L}\right)^{-1} \tag{2.15}$$

is used in a first order approximation:

$$\sigma_0 \approx \frac{a_{L,\perp} - a_L}{a_s - a_L} \tag{2.16}$$

$$\frac{a_L - a_s}{a_s} = \left(\frac{1}{1+\sigma_0}\right)\frac{a_{L,\perp} - a_s}{a_s} \quad . \tag{2.17}$$

σ_0 can be calculated with the elastic constants (c_{xy}) which are properties of the semiconductor

$$\sigma_0 = \frac{c_{12}}{c_{11} + c_{12}} \tag{2.18}$$

The unstrained lattice constant of the layer in a ternary III-V material is related linearly to its composition (Vegard's law):

$$a_{ABC} = x a_{AB} + (1-x) a_{BC} \tag{2.19}$$

This can be solved for x and the composition can now be calculated by combining equations (2.12) until (2.19) and solving for x. In the case of the $In_xGa_{1-x}As$ layer on GaAs substrate example this leads to:

$$x_{InAs} = \frac{c_{11} + c_{12}}{c_{11} + 2c_{12}} \frac{\Delta\theta}{\tan\theta} \frac{a_{GaAs}}{a_{GaAs} - a_{InAs}} \tag{2.20}$$

In the case of relaxed or partly relaxed epitaxial layers, the in-plane lattice constant is not equal to that of the substrate. Thus a second rocking curve of an asymmetric reflection has to be measured, allowing the in-plane lattice constant to be calculated. The definition of an asymmetric reflection is that the diffraction planes are not parallel to the surface of the wafer. Therefore, ω, the angle between the incoming beam and the sample surface, differs from θ, 1/2 of the angle between the incoming beam and the detector. ω is related to θ by $\omega = \theta + \delta$. δ describes the offset due to the choice of diffraction planes and possible wafer miscuts. Also, relaxation can introduce a tilt of the epitaxial layer relative to the substrate. Thus the symmetric scan should be repeated with ϕ rotated to 180°. $\Delta\theta$ can then be calculated:

$$\Delta\theta = \frac{\Delta\omega_{\phi=0} + \Delta\omega_{\phi=180}}{2} \tag{2.21}$$

where $\Delta\omega$ refers to the difference of the ω position of the sample holder (see Fig 2.8 and 2.9) of the Bragg peaks of the substrate and the layer. Further, the asymmetric scan should also be measured for two positions of ϕ: ϕ=0° and ϕ=180°, to account for possible tilts, similar to those of the symmetric case.

Layer Thickness Determination

In Fig 2.12 multiple periodic peaks are located around the layer peak. These are called thickness fringes (or pendellosung fringes) and arise from similar physics as optical interference fringes on thin films. Their periodicity can be used to calculate the thickness according to [20]:

$$\Delta\theta_f = \frac{\lambda \sin\bar{\theta_f} \pm \delta}{t \sin 2\bar{\theta_f}} \tag{2.22}$$

Here $\Delta\theta_f$ is the angle difference between two thickness fringes and $\bar{\theta_f}$ denotes the center between the angle of the two fringes in question. δ is the angle between the surface and the lattice planes, where the positive sign applies to glancing incidence and the negative sign to

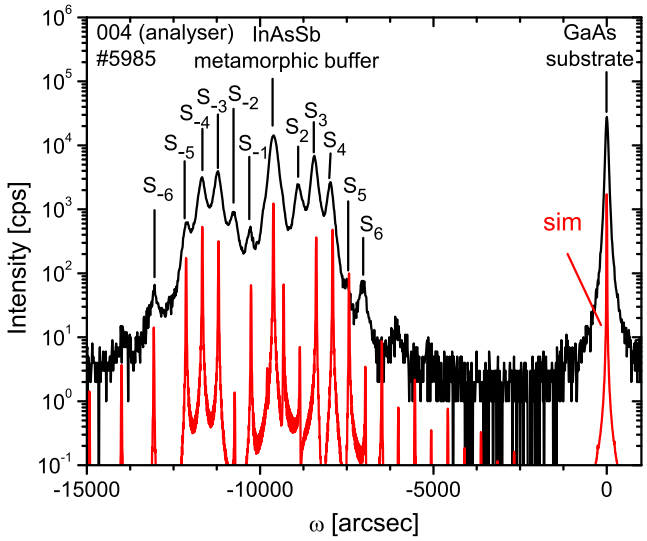

Figure 2.13: (004) triple axis scan of an $InAs_{0.79}Sb_{0.21}$/InAs SL layer on an InAsSb metamorphic buffer lattice matched to GaSb on a GaAs (001) substrate. The analyser crystal was placed in front of the detector to eliminate broadening due to mosaic effects. The satellite peaks due to the SL periodicity are labeled by their order. Note that the 0^{th} and the 1^{st} satellite are hidden in the metamorphic buffer. The simulated x-ray spectrum of the structure is shown below the measurement. It was offset for clarity.

glancing exit in case of an asymmetric reflection. For a symmetric reflection, where $\delta = 0$, the above equation can be simplified and solved for the layer thickness (t):

$$t = \frac{\lambda}{2\Delta\theta_f \cos\bar{\theta}_f} \tag{2.23}$$

However, thickness fringes will only appear clearly in high quality layers with smooth surfaces and sharp interfaces and, when there is no significant diffuse scattering due to e.g. misfit dislocations. Usually for relaxed layers the above described method cannot be applied to measure the layer thickness.

Superlattices

If further periodicity is introduced into the sample structure by growing a periodic multi quantum well (MQW) structure or a super lattice (SL) structure, further fringes, called

satellite peaks, appear in the spectrum. Fig 2.13 displays the (004) reflection of a 25 period SL structure with a period of 40 nm. The SL is grown on a metamorphic buffer layer of $InAs_{0.9}Sb_{0.1}$, which is lattice matched to GaSb, grown on a GaAs (100) substrate. The satellite peaks are centered around the 0^{th} order satellite peak, which appears where one would expect a Bragg peak with average lattice plane spacing ($\bar{d}^{hkl}$) of one period of the SL:

$$\bar{d}^{hkl} = \frac{\sum^i t_i d_i^{hkl}}{\sum^i t_i} \tag{2.24}$$

where t_i is the thickness and d_i^{hkl} the lattice plane spacing of the ith layer within one period of the SL. However, for thin SL structures < 0.25 μm the 0^{th} satellite peak does not appear [21].

The period (m) of the SL is related to the spacing of the satellite peaks [21] via:

$$m = \frac{S_i - S_j\lambda}{2(\sin\theta_i - \sin\theta_j)} \tag{2.25}$$

where S_i and S_j are two satellite peaks and $\theta_{i/j}$ the corresponding angle.

However, the XRD spectra of SL structures are often hard to interpret, since there can be missing satellite peaks and the 0^{th} order peak often is not obvious. Thus, such complex structures are better interpreted with simulation programs. It is of great help though to use the equations above for a rough estimate that can serve as a starting point for the simulation.

X-ray Spectrum Simulation

Section 2.2.3 is based on the kinematical X-ray theory, which is a simplification as only one reflected beam is considered. However, in reality, the reflected beam also undergoes another (forward) Bragg reflection (now parallel to the incoming beam) and again this beam is reflected. Secondary reflections are very weak, but in sufficiently large and high quality crystals, they build up and have to be taken into consideration. Also absorption of x-rays by the crystal has to be considered. The full treatment of the electromagnetic wave in a periodic potential, including all scattering and absorption mechanisms is called the dynamical theory. Within this framework it is possible to predict peak shapes and intensity distributions. An introduction can be found in Warren [22].

X-ray spectra of multiple layers including superlattices can become very complicated due to the superposition of all the fringes and peaks of every single layer. The best way

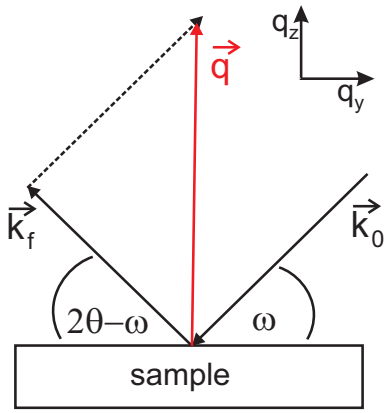

Figure 2.14: Schematic of x-ray reflection of a sample. Incident x-rays photons are represented by the wavevector $\vec{k_0}$ and are reflected off the sample ($\vec{k_f}$). The change in momentum $\Delta\vec{k}$ can be regarded as a vector ($\vec{q}$) in reciprocal space. A signal appears only if this vector equals a reciprocal lattice vector.

to analyze these is to use commercially available simulation programs that fully apply the dynamical theory. These will calculate the x-ray pattern of a given layer structure as shown in Fig 2.12. Those programs are also able to fit the spectra. However, the fitting typically only works satisfactorily when the parameters of the starting simulation are close enough to the actual values. All thicknesses and compositions extracted from the HR-XRD measurements were found through simulations. Data recorded with the Panalytical X'Pert system were usually analysed with the "Expert Epitaxy" program by Panalytical, while the data generated with the Bede system was analysed with the help of Bede's "RADS" program.

2.2.4 Reciprocal Space Maps

As shown in the Laue condition (see Eq 2.10 the scattered vector $\Delta\vec{k}$ can be interpreted as a vector in reciprocal space ($\vec{q}$). Based on the geometry shown in Fig 2.14, the components of $\vec{q}$ can be calculated from angles ω and 2θ of the diffractometer (see Fig 2.8) using

equation 2.11:

$$q_y = \frac{1}{\lambda}[\cos(2\theta - \omega) - \cos\omega] \quad (2.26)$$

$$q_z = \frac{1}{\lambda}[\sin(2\theta - \omega) + \sin\omega] \quad (2.27)$$

The above relationship shows how an area around a lattice reflection can be scanned and a reciprocal space map can be generated, by offsetting ω and then performing an $\omega - 2\theta$ scan and then repeating this procedure for a range of ω offsets (ω_{offset}). Note that 2θ is scanned over the same range for each scan, but with different center values of ω_{offset}. In this procedure a very small detector acceptance angle is needed and thus the maps are recorded with the analyser crystal in front of the detector. An example of the raw data for a symmetric reflection is shown in Fig 2.16.

Fig 2.15 and 2.16 show examples of reciprocal and angle space maps of an asymmetric as well as a symmetric reflection of the sample discussed in Sec 2.2.3. A full (004) triple axis scan of that structure is shown in Fig 2.13. In Fig 2.15 the reciprocal space area around the metamorphic buffer layer peak is shown for a (115) diffraction condition. The SL satellite peaks as well as the metamorphic buffer layer peak are clearly visible and are at the same value on the Δq_y axis, which corresponds to the in-plane lattice spacing in real space. This shows that every single layer of the SL is completely strained on the metamorphic buffer layer. Further, the degree of relaxation of the metamorphic buffer layer can be calculated from the exact position of the diffraction spot relative to the substrate, which is outside the reciprocal space area depicted in the figure.

In order to distinguish between mosaic and compositional broadening, an angle space area around a symmetric diffraction spot needs to be recorded. Fig 2.16 shows a two dimensional area around the (004) diffraction spot of the metamorphic InAsSb buffer layer. In this case it is possible to deconvolute broadening due to mosaicity and broadening due to layer composition and possibly for a SL, period variation. Broadening along the ω_{offset} axis is due to locally slightly different orientation of the lattice planes due to the formation of strain relieving misfit dislocations, which is called mosaicity. The mosaicity strongly visible in this sample is due to the way the InAsSb buffer layer has relaxed.

In general, recording reciprocal space maps is a very powerful, yet time consuming tool to study semiconductor samples. For example, the single 004 scan was recorded in 30 min

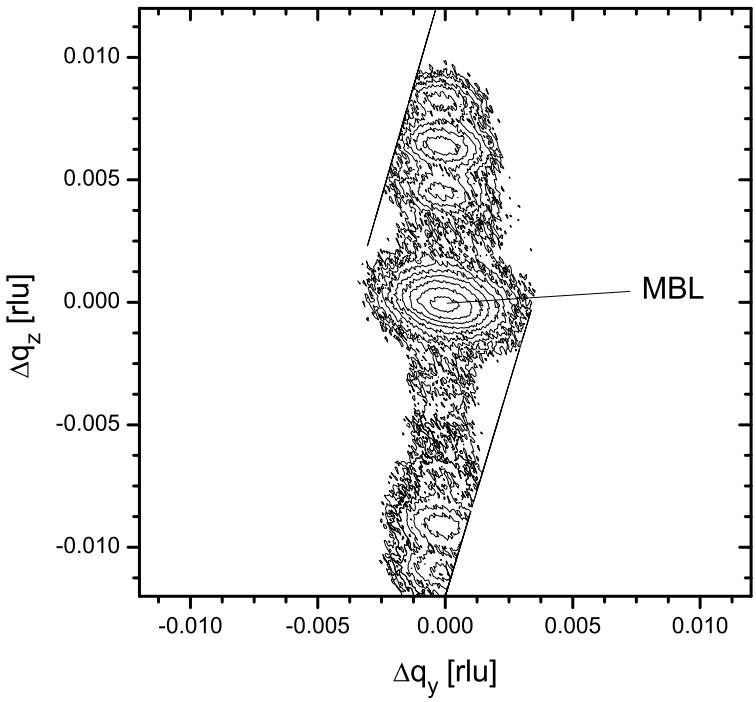

Figure 2.15: Reciprocal space map around 115 reflection of an InAsSb/InAs SL structure on GaAs. The SL structure is strain balanced around a 1 μm metamorphic InAsSb buffer layer lattice matched to GaSb but grown on a GaAs substrate. Only the area around the metamorphic buffer layer (MBL) is shown and relative reciprocal space coordinates are used. For a full 004 triple axis scan of this structure see Fig 2.13. All SL-peaks are on the same Δq_y coordinate, which means that the metamorphic InAsSb buffer and the SL have the same in-plane spacing. Thus the SL is fully strained.

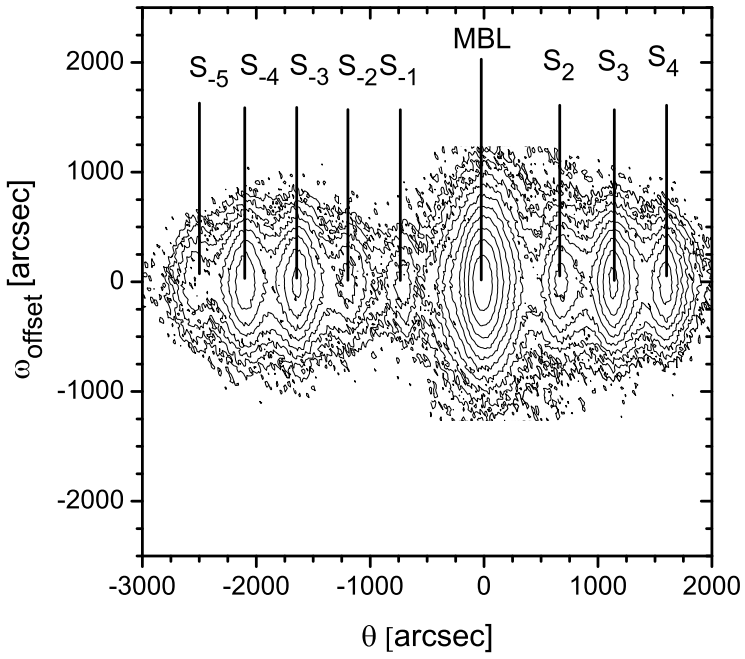

Figure 2.16: Angle space map around 004 reflection of InAsSb/InAs SL structure on GaAs. For a full 004 triple axis scan of this structure see Fig 2.13. Only the area around the InAsSb metamorphic buffer layer (MBL) is shown in relative coordinates. The asymmetry of every diffraction spot shows that the complete strain relaxation of the InAsSb buffer layer has resulted in mosaic structure with a FWHM of tilt angles of 662 arcsec, which is much larger than the FWHM of 215 arcsec in the $\omega - 2\theta$ direction.

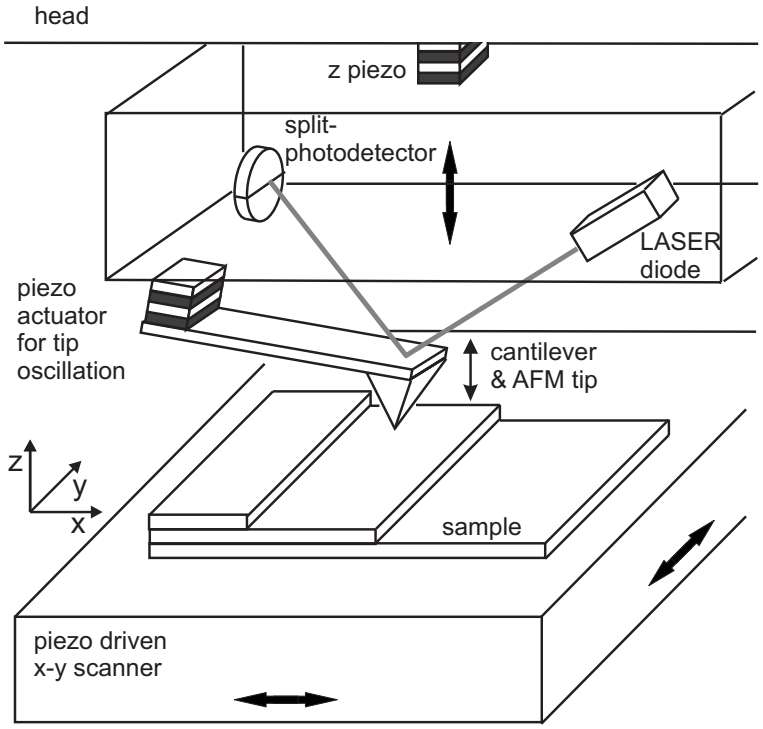

Figure 2.17: Schematic drawing of an AFM. The deflection of the AFM-tip is measured by the deflection of a laser beam from the backside of the reflective cantilever. The sample is mounted on a stage that can be precisely moved in x- and y-direction via a piezo-electric position control. The z-direction piezo-electric position control is mounted in the head above the AFM-tip.

while it took 16 h to collect the data shown in the (004) space map of only about 1/3 of the range along the $\omega - 2\theta$ axis.

2.3 Atomic Force Microscopy

The atomic force microscope (AFM) is a tool that can quickly give information on the topology of surfaces with a resolution in the order of Angstroms. The MFP-3D^{TM} AFM used in this work was built by Asylum Research.

A sharp tip on a cantilever is slowly brought close to the sample surface until it interacts

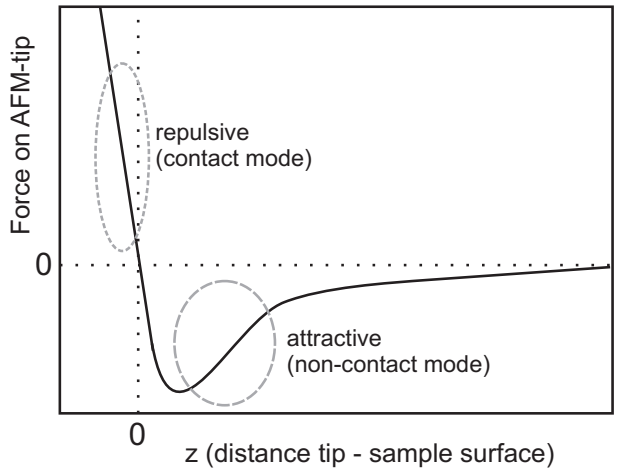

Figure 2.18: Schematic drawing the interaction force between the AFM-tip and the sample surface as a function of separation between tip and sample [23].

with the surface via interatomic van der Waals forces. The position of the tip is measured by the deflection of a laser beam from the backside of the tip. The sample is mounted on a piezo-motorized stage which is used to scan over the region of interest on the sample. Via a feedback loop, distance between the tip and the surface is held constant by a piezo-electric control in the z-direction. The feedback signal is read out and gives the height information of the sample. A schematic of an AFM is shown in Fig 2.17.

Fig 2.18 shows a schematic plot of the force acting on the front of the tip as a function of the separation between the tip and the sample surface. The two main ways of operating an AFM are a) contact mode, the tip touches the sample, and thus the force on the tip is repulsive, and b) non contact mode the sample, the tip is in the attractive region as marked in the graph.

Contact Mode

The AFM-tip is brought slowly down until it touches the surface and the cantilever is deflected to a certain degree. The deflection is measured as the difference in signal of the two photodiode areas. The sample stage is now moved along the x-direction and via a feedback loop controlling the z-direction, the deflection of the tip is kept constant. The z-movement

is read out and directly gives the height information. The sample is scanned line by line.

Non-Contact Mode

In non contact mode, the AFM cantilever is driven by the piezo actuator in resonance, so that the tip is oscillating above the sample. Then the tip is slowly lowered into the attractive force regime until in this particular AFM type the amplitude of the oscillation is reduced to a predefined set-point of the tip-surface interaction. As the sample is scanned along the x-axis, the amplitude is kept constant, by moving the tip along the z-axis via a feedback loop. The z-axis position is read out and determines the height information. This is repeated for different positions on the y-axis and a square area of the sample is rastered line by line. The non-contact mode has the advantage that the tip is less likely to damage the surface or pick up dirt. Thus, the tips tend to stay usable for a greater number of scans than in contact mode. This mode was chosen for the AFM measurements for this work.

2.4 I-V & C-V Measurements

Current versus voltage (I-V) and capacitance versus voltage (C-V) measurements were performed on device structures using a two point probe station. The instruments were controlled and data were recorded via a Labview program on a personal computer.

In the case of I-V measurements a Keithley 230 programmable voltage source was in series with a Keithley 195A digital multimeter (current measuring mode) and the sample. The voltage across the sample was measured with a Keithley 175 autoranging multimeter. The current was then plotted as a function of the measured voltage across the device.

This technique was used to evaluate some properties of the fabricated semiconductor diodes, specifically rectification, leakage current and the product of area and resistance at zero bias value (R_0A). R_0A was calculated by fitting a linear slope to a narrow voltage range around zero bias in the I-V curve. The inverse slope was then multiplied by the diode area.

In the case of the C-V measurements, the sample was connected to a Boonton 72BD capacitance meter, operating at 1 MHz. A Keithley 230 programmable voltage source was connected to the capacitance meter to provide a voltage across the sample. This voltage

was stepped with the Labview program. The voltage and the measured capacitance of every voltage step were recorded and plotted.

2.4.1 Carrier Concentration from C-V Measurements

Capacitance-Voltage (C-V) measurements can be used to determine the doping and the built-in potential (V_{bi}) of a diode. The short discussion of the interpretation of a C-V measurement given here is combining treatments by Schroder [24] and Streetman [25].

The capacitance C is defined as:

$$C = -\frac{\mathrm{d}Q}{\mathrm{d}V} \quad , \tag{2.28}$$

where Q is the charge and V the voltage. Within the depletion approximation of a one-sided abrupt p-n or a Schottky junction (see Fig 2.19), the charge is given by

$$Q \approx -qA \int_0^W N_D \mathrm{d}x \quad , \tag{2.29}$$

assuming the depletion occurs here in an n-type semiconductor. Here q denotes the elementary charge, A the junction area, W the width of the space charge region and N_D the donor density assuming all donors in the depletion region are ionized. The charge increment $\mathrm{d}Q$ is due to a slight increase of the space charge region, so:

$$C = -\frac{\mathrm{d}Q}{\mathrm{d}V} = qA\frac{\mathrm{d}}{\mathrm{d}V}\int_0^W N_D \mathrm{d}x = qAN_D(W)\frac{\mathrm{d}W}{\mathrm{d}V} \quad , \tag{2.30}$$

assuming N_D is constant over the distance $\mathrm{d}W$. W for such junctions can be approximated by [26]:

$$W \approx \sqrt{\frac{2k_s\epsilon_0}{qN_D}\left(V_{bi} - V\right)} \quad , \tag{2.31}$$

where k_s describes the dielectric constant, ϵ_0 is the vacuum permittivity and V_{bi} is the built-in potential. When taking the derivative of W with respect to V of equation 2.31 and inserting the expression into equation 2.30 together with expression 2.31, the capacitance is then given by:

$$C = \frac{A\sqrt{2qN_Dk_s\epsilon_0}}{\sqrt{V_{bi} - V}} = \frac{k_s\epsilon_0 A}{W} \quad . \tag{2.32}$$

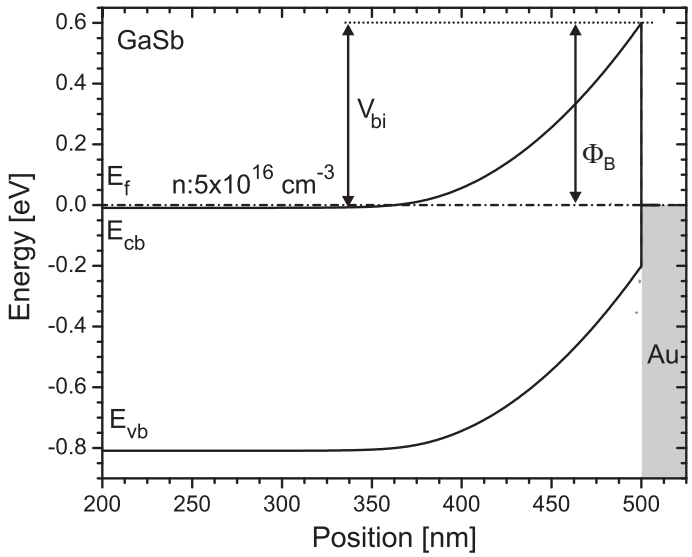

Figure 2.19: Simulation of the band line-up for a n-GaSb/Au Schottky-junction at 77 K. The doping of GaSb is 5×10^{16} cm^{-3}. The dot-dashed line represents the Fermi level. The Schottky barrier height (Φ_B) was assumed to be 0.6 V according to Ref [27].

This leads directly to the expression for $1/C^2$:

$$\frac{1}{C^2} = \frac{1}{2qN_D k_s \epsilon_0 A^2}\,(V_{bi} - V) \tag{2.33}$$

Thus, when plotting ($1/C^2$) as a function of V, the slope is related to the donor (or acceptor) concentration (see Eq 2.33). Also, the voltage-axis intercept can be interpreted as the built-in potential V_{bi}. For illustration, the band line-up and built-in potential of a Schottky diode is shown in Fig 2.19. Actual measured C-V curves are shown in Fig 3.12 and Fig 4.5.

2.5 Hall Effect Measurements

To carry out doping calibrations, Hall measurements were conducted at room temperature and at 77 K. By measuring the Hall voltage in a magnetic field and the sheet resistance of a semiconductor layer, the carrier type, density and the carrier mobility can be determined.

The measurement was done using the van der Pauw technique [28] with B fields between 0.1 and 0.5 Tesla. A general introduction to Hall measurements can be found in [29].

The contacts were made of In dots in case of n-doping and InZn dots for p-doped layers. The contacts were annealed under a N_2 environment by heating until the melting of the metal was visible. The metal to make the contacts was precleaned in acetone and isopropanol before being deoxidized with diluted HCl (HCl:H_2O=1:10). The layers for Hall effect measurements were grown on GaAs semi-insulating wafers. A typical Hall sample was a square with side lengths of 1 cm.

2.6 Experimental Methods by Collaborators

This thesis also includes results by experimental methods that were obtained through various collaborations. Details regarding specific experimental conditions can be found in the respective chapters where the results are discussed.

The photoluminescence (PL) and optical detector response were measured by Fourier transform (FT) spectroscopy by the group of Dr. M. Thewalt at SFU. The operating principles of FTPL spectroscopy are discussed in detail in, e.g., Ref [30, 31].

Transmission electron spectroscopy (TEM) measurements were carried out at the Nanoimaging Facility at SFU and at the London Centre for Nanotechnology of the Imperial College London under the supervision of Dr. K. Kavanagh. Detailed insights regarding transmission electron microscopy can be found in Ref [32].

Semiconductor diodes were fabricated by Dr. Y.T. Cherng at 4D labs at SFU and by Dr. E. Plis at the Center for High Technology Materials at University of New Mexico, where temperature dependent I-V measurements and variable array diode analysis (VADA) were also carried out.

Chapter 3

Morphology and Growth

Antimonides are used for technical applications in high speed devices due to their high mobilities or in infrared lasers or detectors because of their low bandgap energy. Antimonides are typically more challenging to grow epitaxially in high quality compared to arsenides. One reason for this is the low vapour pressure of Sb. When the V/III ratio is too high, Sb which is not incorporated tends to float on the surface and can lead to Sb crystallites appearing on the surface. A V/III ratio below 1 will always cause the III-metal to form islands on the surface and thus the V/III ratio needs to be controlled carefully. Further the low melting temperature of InSb (525°C) limits the growth to temperatures far below the typical growth temperatures of arsenides (550°C– 650°C). A more detailed review of the MOCVD growth of antimonides can be found in [16].

This chapter describes the studies regarding the epitaxial growth of InAsSb and InAsSb/InAs superlattices and challenges met. Further, scanning transmission electron microscopy (STEM) investigations are presented showing a Ga diffusion from the GaSb wafer into the initial InAsSb layer. Matthews and Blakeslee's approach to calculate the critical thickness of heteroepitxial layers is introduced and used to calculate the critical thickness of InAsSb on GaSb (InAs) as a function of Sb composition. The last section of this chapter discusses the doping of the material. Parts of this chapter were published in [10].

3.1 OMVPE growth of InAsSb

For the growth of InAsSb on GaSb, the native oxide on GaSb was removed by wet chemical etching immediately prior to loading the substrate into the reactor. The GaSb wafers were submerged in hydrochloric acid (37%) for 2 minutes followed by three rinses in isopropanol and a N_2 blow-dry. In the reactor, the substrates were heated to 400°C under H_2 and then to growth temperature, typically 500°C, under TMSb stabilization. Note that GaSb cannot be stabilized under TBAs as this causes significant roughening of the surface. In order to reduce developing costs, only a 1/4 wafer of GaSb was grown on at a time. Epilayers were initially grown on a regular 2 inch wafer susceptor with masking pieces of GaAs to keep the substrate in the center and later with a specially designed susceptor that had a 1/4 wafer pocket. For all device growths, the substrate was rotated at 15 rpm in order to increase the homogeneity of the deposition.

Fig 3.1 shows the distribution coefficient $k = ([Sb]/[As])_{sol}/([Sb]/[As])_{vap}$ of Sb in InAsSb. $([Sb]/[As])_{sol}$ is the molar ratio of Sb atoms to As atoms in the solid and $([Sb]/[As])_{vap}$ is the nominal molar ratio of Sb atoms to As atoms in the gas-phase during the growth. Thus x_{Sb}(vapour) is defined as: $([Sb]/([Sb]+[As])_{vap}$. There is a strong preferential incorporation of InAs into the crystal, as InAs is more stable than InSb. This results in a distribution coefficient dependence on the V/III ratio. In this work, for a V/III ratio close to 4 and a growth temperature (T_{growth}) of 500°C, k is equal to 1. For a V/III ratio of 6, k is between 0.4 and 0.5. Note that the given V/III ratios are the ratios of the precursors sent into the reactor. These can differ from the actual growth species ratios at the substrate due to incomplete decomposition of the precursor molecules at low substrate temperatures or prereactions. The low growth temperature is in fact problematic for InAsSb growth with the TMSb precursor, which only starts to dissociate around a temperature of 450°C. TBAs in comparison is 50% decomposed at 300°C [16]. Thus the Sb composition is also dependent on growth temperature for temperatures around 500°C. Also, on InAs substrates, the Sb incorporation is slightly lower than on GaSb substrates under similar growth conditions as shown in Fig 3.1 (compare × with ★).

Further, changing the H_2 carrier flow in the reactor from 3 to 6 SLM, which results in an increased flow rate, also decreases the Sb incorporation slightly (Fig 3.1 compare ■ and ★). The change from 3 SLM to 6 SLM, the standard operation condition, was introduced in

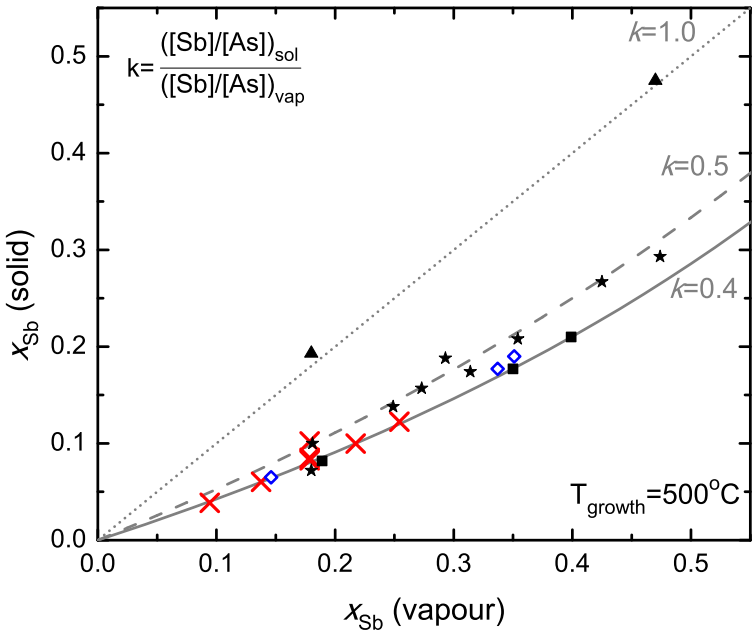

Figure 3.1: Sb mole fraction in solid InAsSb (x_{Sb} (solid)) as a function of nominal Sb mole fraction in vapour (x_{Sb} (vapour)) for different growth conditions and substrates at a growth temperature of 500°C. Layers grown at a carrier flow of 3 SLM on a GaSb miscut substrate at a V/III ratio of 3.8 (▲) and V/III ratio of 6 (★) fall on a distribution coefficient (k) curve of 1 and 0.5. Layers grown on InAs exact substrates at a carrier flow of 3 SLM and a V/III of 6 (×) and layers grown on both GaSb miscut (■) and exact substrates (◇) with a carrier flow of 6 SLM and a V/III ratio of 6 follow a distribution coefficient of 0.4.

order to reduce Sb memory effects in MQW structures, assuming that a higher carrier flow can purge the system faster from excess Sb on the surface during a growth interrupt after an InAsSb quantum well. Increasing the carrier flow also leads to an unwanted decrease in growth efficiency, as the precursor partial pressures in the reactor are reduced (see Eqn 2.5). However, at a later time it was found that coating of the reactor with GaSb or GaAs before the run has a much larger effect on Sb memory, than the change in carrier flow. This led to the practice of coating the susceptor with GaAs prior to each growth. Note that the best devices as determined by optical response measurements were grown under the 6 SLM conditions. Susceptor coating runs also decreased the incorporation coefficient fluctuations significantly. Having to do costly coating runs in order to grow reproducible layers is strong evidence for an Sb memory effect, caused Sb adsorbed on the susceptor and/or the reactor walls. Turbulent flow patterns may also be responsible. The memory effect could be reduced by an improvement in the reactor design and the use of full wafers, where a smaller area of the susceptor is exposed. Further when growing antimonides, after typically a few microns of growth or about every two weeks, visible defects and roughening would appear on the epilayers which would be present under all growth and coating conditions, until the susceptor was taken out of the reactor and cleaned in aqua regia ($HCl:HNO_3$ = 3:1). For comparison, when growing arsenides, the susceptor was cleaned about every 6 months.

Due to the incomplete thermal decomposition of the TMSb precursor and because of the general trend of increased carbon incorporation at low temperature growth, a higher growth temperature is desirable. However any increase of growth temperature always led to a significant broadening of the XRD-spectrum indicating compositional variations in the layer. The measured X-ray rocking curves for samples with a layer thickness of around 100 nm grown at temperatures of 500°C, 520°C and 540°C are displayed in Fig 3.2. Thus the increase in growth temperature was abandoned and instead the V/III ratio was increased. The latter often decreases the incorporation of impurities like C and O in OMVPE grown materials.

Historically, the project started with growth on GaSb (100) substrates miscut by 2^0 towards (111)B. However, epilayers with less surface roughness and also narrower XRD-peaks could be grown on InAs (100) exact wafers. Because of the growth success on InAs (100) exact wafers, the growth on GaSb (100) exact wafers was tested. For thin layers, surface roughness values (root mean square, RMS) of typically 3 Å were observed and

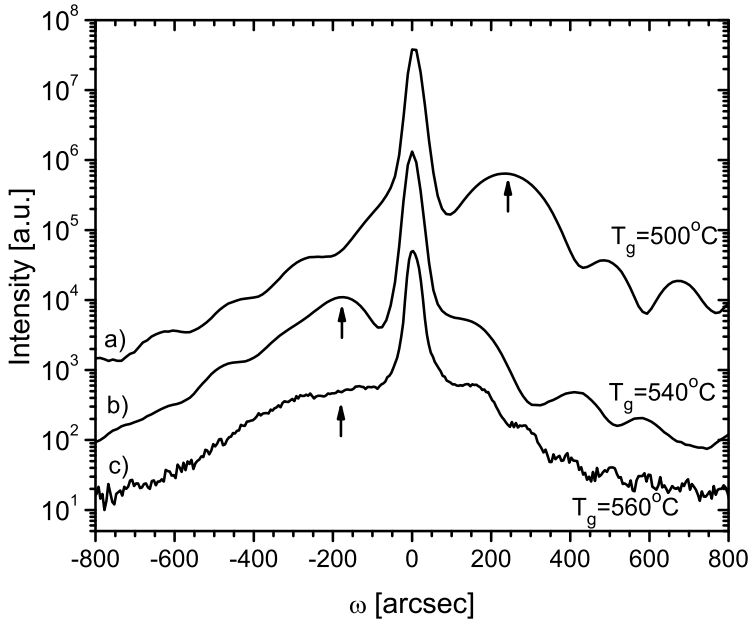

Figure 3.2: HR-XRD $\omega - 2\theta$ scans of an InAsSb layer close to lattice matched composition on GaSb miscut substrates for different growth temperatures. With increasing temperature, the InAsSb peak (marked by arrows) becomes broader and the pendellosung fringes weaker. Sample a:T_g=500°C; x_{Sb}=0.074; 78 nm. Sample b:T_g=540°C; x_{Sb}=0.1; 87 nm. Sample c:T_g=560°C; x_{Sb}=0.1; 140 nm. The layer parameters were extracted from rocking curve simulations.

monosteps are visible in the AFM images (see 3.3b) but for layers above ≈250 nm, the roughness increased by a factor of 10 to 100 and haziness was often visible to the naked eye. It is possible that without Sb stabilization during the substrate heat up, this could be improved, as suggested by Huang et al., who have successfully grown InAsSb on GaSb exact substrates with RMS values below 2 Å in a very recent work [9]. AFM images of typical InAsSb surfaces on different substrates are shown in Fig 3.3. On GaSb miscut wafers, RMS values of a few nm are typically found with a "sand-dune" like structure, which is possibly due to atomic step bunching. Surfaces with RMS values below 0.5 nm are achieved on InAs exact substrates where monosteps are clearly visible. Similar, but with more fuzzy edges, is the AFM image for InAsSb on GaSb exact substrates for thin layers. Unfortunately no growth conditions were found for which this surface was stable. Fig 3.3d shows the surface of a homojunction device on a GaAs exact substrate. Here the roughness is comparable to growths on GaSb miscut wafers, despite the fact that the 1 μm InAsSb buffer layer is completely relaxed.

3.1.1 Structural Results of InAsSb/InAs MQWs on GaSb Substrates

Good structural properties of the epitaxial layers are a prerequisite of quality devices. Electrical properties of semiconductor layers are tied to structural properties. For example, crystal defects like dislocations reduce the carrier mobilities. Another example is segregation in QW structures which leads to different QW shapes and thus to different quantized energy levels from those intended. In this section MQW InAs/InAsSb structures grown on GaSb were investigated with transmission electron microscopy where atomic scale resolution can be achieved. With this technique, strain fields, and interface roughness on an atomic level can be made visible.

Test structures were grown, consisting of six periods with three layers each: a 10 nm $InAs_{1-x}Sb_x$ QW, followed by a 20 nm InAs barrier layer; the final layer of each period was again a 10 nm $InAs_{1-x}Sb_x$ QW with the same composition than the first layer. Thus, the total number of layers (excluding the GaSb buffer) is 13. A schematic of the sample structure is shown in Fig 3.4. The MQW samples discussed in this section are summarized in Table 1. Sample 1 achieved an Sb mole fraction of $x = 0.15$ as determined from XRD simulations. Samples 2 and 3 achieved an Sb mole fraction of 0.21. Sample 3 was identical

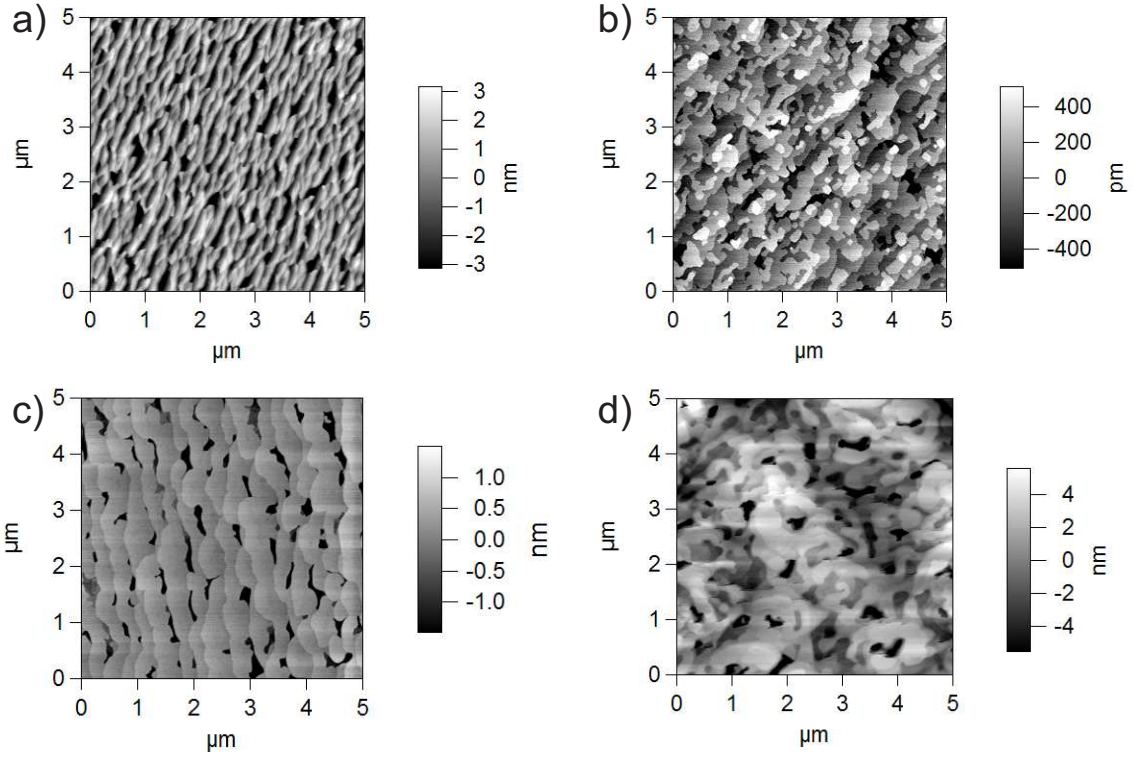

Figure 3.3: AFM images of InAsSb films on different substrates. The Sb composition is close to lattice matched on GaSb for all cases. a) GaSb miscut substrate; RMS=1.5 nm. b) GaSb exact substrate; RMS=0.25 nm. c) InAs exact substrate; RMS=0.46 nm. d) GaAs exact substrate; RMS=2.5 nm.

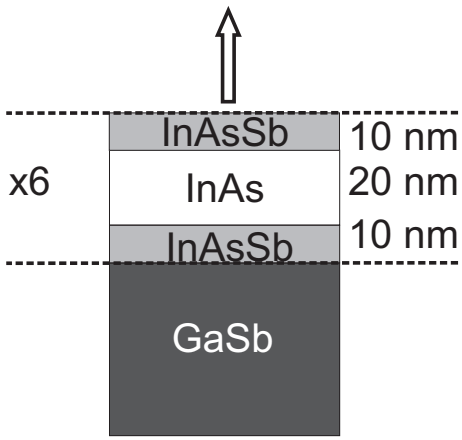

Figure 3.4: Schematic of sample structure discussed in this section. Only the first of 6 periods is depicted. Nominal layer thicknesses are shown.

sample	substrate	x_{Sb}
1	GaSb	0.15
2	GaSb	0.21
3	GaSb	0.21

Table 3.1: MQW samples discussed in the text. Sample 3 differed from the other samples in that a GaSb buffer was grown and then the system was cooled to room temperature before reheating for the subsequent growth of the InAsSb/InAs layers.

to sample 2 with the exception that the GaSb buffer layer was grown in a separate growth step and cooled to room temperature before the subsequent InAsSb growth. This was done in order to rule out gas phase memory effects, as will be discussed later. The GaSb was grown at 540°C with TEGa as Ga precursor.

For transmission electron microscopy, a FEI field emission Tecnai 20 (200 keV) or a monochromated FEI Titan 80-300 (300 keV) system was used. In scanning mode, a high angle annular dark field (HAADF) detector as well as energy-dispersive x-ray spectroscopy (EDS) were used in order to obtain high resolution compositional information. Cross-section samples were prepared by manual thinning and additional ion-milling with liquid nitrogen cooling at a milling angle of 15°.

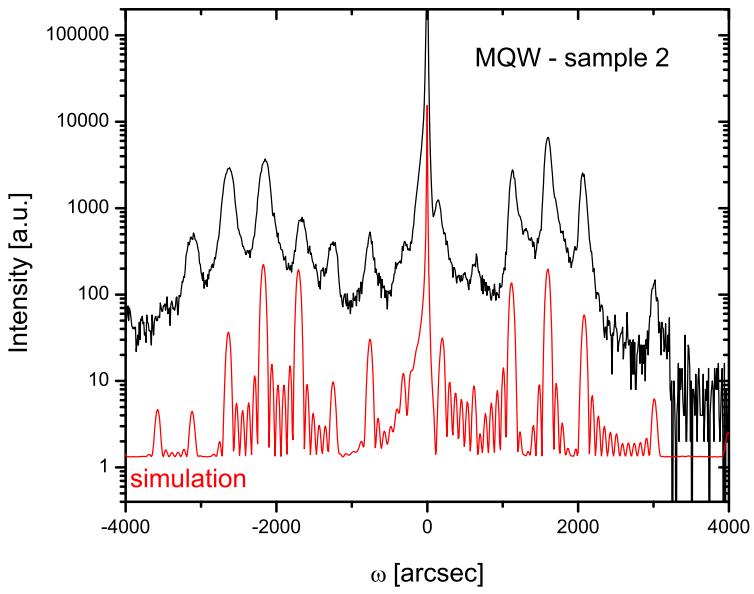

Figure 3.5: XRD $\omega - 2\theta$ scan of the MQW sample 2 (top) and simulation (bottom). The simulation used an InAsSb layer thickness and composition of 20 nm and $x_{Sb} = 0.21$ respectively. The InAs layer thickness was 19 nm

A 004 XRD scan of the MQW sample 2 is presented in Fig. 3.5. The fact that satellite peaks are clearly visible and are sharp reveals good overall agreement with the intended structure. In particular, the observation of sharp satellite fringes and thickness fringes rules out appreciable relaxation by dislocation formation. Curve fitting to each spectrum verified the QW thicknesses (20 nm) and the Sb composition in the InAsSb quantum wells (x_{Sb} = 0.21). The slight broadening of the measured spectrum compared to the simulation is probably due to Ga and Sb intermixing effects discussed later(see Fig. 3.7).

The XRD data indicate good but not perfect agreement with the dynamical diffraction simulations based on the intended structures. We performed high resolution TEM in order to further investigate the cause of this remaining discrepancy. The interface between the GaSb and InAsSb was studied in detail for sample 2. Figure 3.6 displays a 300 keV STEM-HAADF image showing contrast predominantly associated with the atomic number differences between the first InAsSb quantum well and the GaSb buffer layer. The interface is planar on an atomic scale with no dislocations or stacking faults evident in this image.

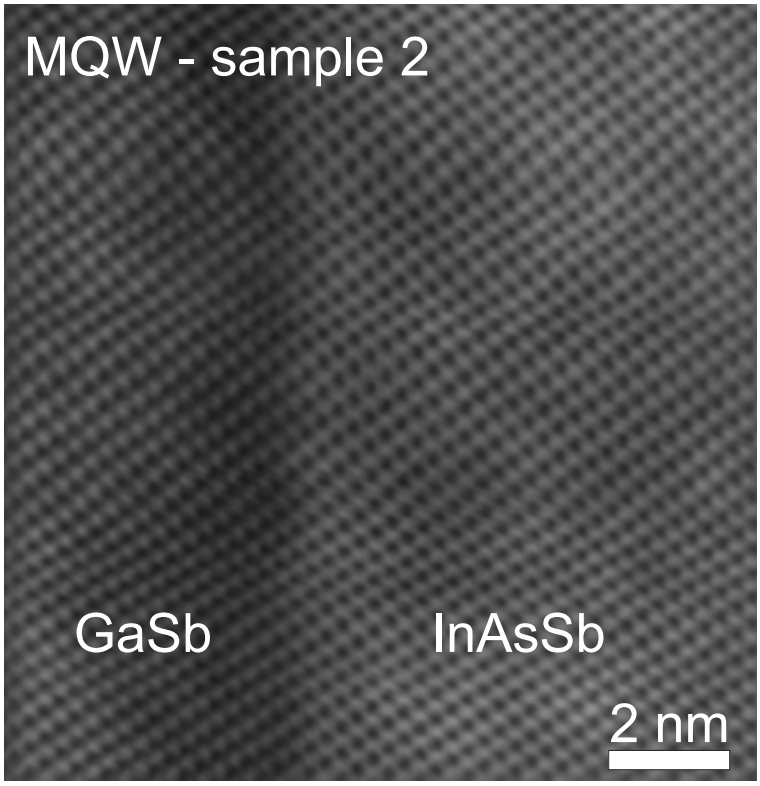

Figure 3.6: HAADF-STEM (300 keV) image of the GaSb/$InAs_{0.79}Sb_{0.21}$ interface of the first QW of the continuously grown sample 2 along the 110 direction. The image clearly shows the ordered lattice as well as the absence of dislocations or stacking faults within the viewed area. The slight waviness is due to the beam stability of the STEM.

While the STEM image shows the interface to be planar, EDS linescans show that there is some intermixing at the GaSb/InAsSb interface and at the subsequent InAs/InAsSb interfaces. For an EDS linescan the electron beam of the STEM is scanned across the sample. As the electron beam interacts with the atoms, electron-electron collisions between the electrons from the beam and electrons from the inner shell of the atoms occur and core electrons are removed from their shells. When those levels are being refilled by electrons from outer shells, x-ray photons with characteristic energies are produced. By detecting this characteristic radiation as a function of energy and intensity, the elements can be identified by the energy position of the peaks and quantitative composition analysis can be concluded from the peak intensity ratios. An EDS linescan for sample 2 is shown in Fig. 3.7. This figure indicates a carryover of Ga into the first InAsSb layer for approximately 6-10 nm. In addition, there is a noticeable asymmetry between the bottom and top interfaces of the InAsSb wells. The bottom InAs/InAsSb interface is abrupt to within the resolution of the EDS measurements (approximately 2.5 nm) while the top InAsSb/InAs interfaces show noticeable grading over a length scale of $\approx$10 nm. This is most likely a surface segregation effect and has been reported previously by several groups [16]. The lower surface energy of InSb results in a tendency for Sb rich layers to float on InAs layers, resulting in unintentional Sb incorporation during subsequent InAs growth. This leads to an asymmetry in QW interfaces for materials with large differences in surface energy.

The Ga memory effect observed here, where Ga atoms were detected in the InAsSb layer above the GaSb layer, has not been reported to our knowledge. There are a couple of possible reasons for it: (1) carryover of Ga from the pipework following gas switching between the GaSb and InAsSb layers growths (2) carryover of Ga adsorbed on the sample holder (susceptor). In order to distinguish between these two possibilities, we grew an additional sample 3 with $x_{Sb} = 0.21$ by a two step procedure in which the GaSb buffer layer was grown, and the sample was then cooled to room temperature in order to completely purge the gas lines. The InAsSb/InAs MQW layers were then grown under conditions in which there could be no Ga gas phase memory effects. EDS data for sample 3 were very similar to that of the continuously grown sample 2, verifying that the cause of the Ga carryover was not due to gas switching effects.

TEM measurements of the $x = 0.21$ MQW samples 2 and 3 were obtained under both 002 and 220 diffraction conditions. Fig. 3.8 shows results for sample 3. Similar images

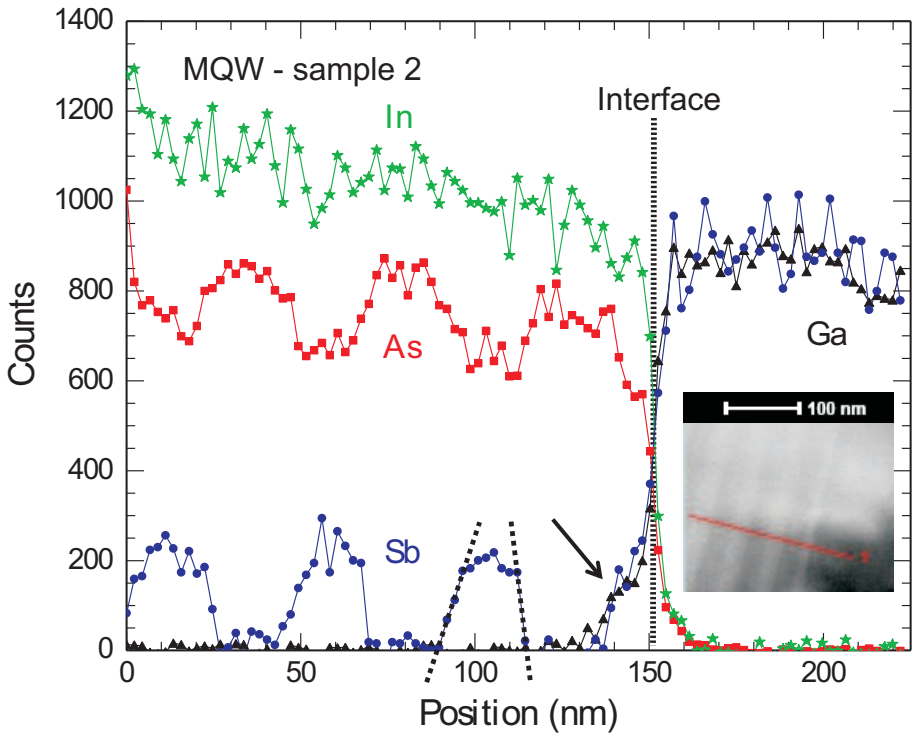

Figure 3.7: EDS analysis of the MQW sample 2. The scan was done along the line in the inset (across the GaSb/InAsSb interface perpendicular to the QWs). A plateau of Ga after the GaSb/InAsSb interface is clearly seen, as well as an Sb segregation effect into the InAs layers indicated by the asymmetric on and off behavior of the quantum wells. The change of the In signal level with position is due to the gradual change in TEM sample thickness.

were obtained for sample 2. Using 004 bright field (BF) conditions at 200 keV (Fig. 3.8a) the QWs appear to be smooth with sharp interfaces and constant thickness in agreement with results from the XRD simulations. When studying the same interface with a TEM under 220-bright-field (BF) conditions (Fig. 3.8b), which is a reflection that is much more sensitive to strain, lateral strain fluctuations were detected. The strain fields have a mean lateral distance of $\approx$ 5 nm and reach about 20 nm into the InAsSb/InAs. The strain fields are detected in the two step growth sample (3) as well as the continuously grown one (2). Similar results were obtained for an InAsSb sample lattice matched to GaSb. The most likely cause of these strain fluctuations is the Ga carryover observed in Fig. 3.7 since they have a similar length scale as the Ga memory observed in EDS. We have shown that the carryover does not originate from nonideal gas switching. It is most likely that it originates from Ga adsorbed on the susceptor.

3.2 Critical Thickness Calculation

When growing a strained layer heteroepitaxially on a substrate, the layer will grow to a certain thickness without the formation of misfit dislocations. After a certain thickness, which depends on the lattice mismatch between the substrate and the epitaxial layer, the epitaxial layer will relax by forming misfit dislocations. These crystal defects can have negative effects on the electrical and optical properties of the crystal, as they reduce the carrier mobility due to increased scattering [33] and can act as non-radiative recombination centers [34].

In this work, an important design criterion to know is the critical thickness of InAsSb as a function of Sb composition, as every layer has to be below the critical thickness. A model, developed by Matthews and Blakeslee [35] was used to predict the critical thickness for the superlattice layers. The Matthews and Blakeslee argument will be reproduced below and then employed to discuss InAsSb grown on GaSb and on InAs substrates.

It is assumed that strain relaxation occurs through a rectangular array of noninteracting edge dislocations which form when dislocations already present in the substrate or half-loop dislocations which originate on the growth surface “glide” along the interface. In this model, the critical layer thickness (h_c) is reached when the force exerted on the dislocation (F_H) due to misfit stress is equal to the tension in the dislocation (F_D) which can then be

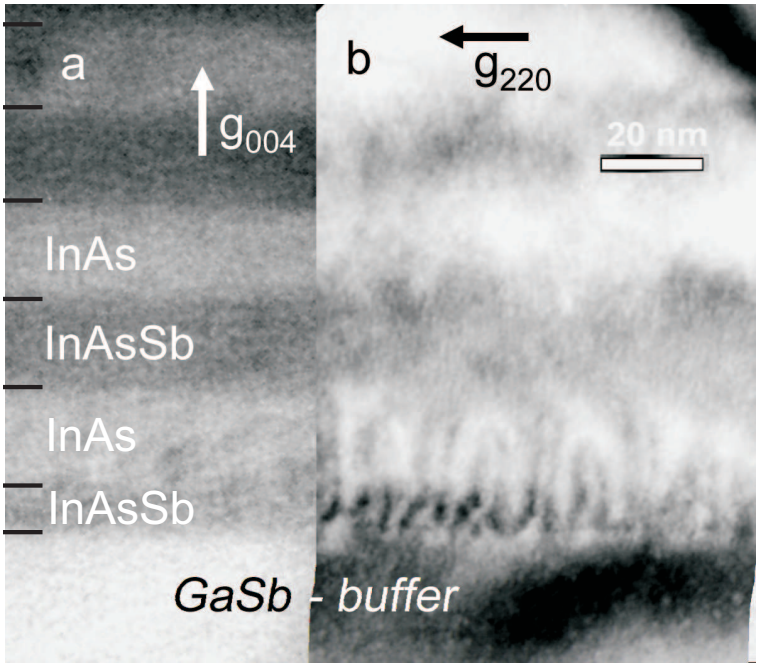

Figure 3.8: Bright field TEM images of the start of the 2 step growth MQW structure (sample 3) for diffraction conditions: (a) (004) and (b) (220). The GaSb buffer and the first MQW layers (starting with a 1/2-layer of InAsSb) are shown. The short black lines on the left indicate the layer interfaces. The strong contrast fluctuations in b) are due to lateral strain fluctuations that originate at the GaSb-InAsSb interface. The scale marker is identical for both images.

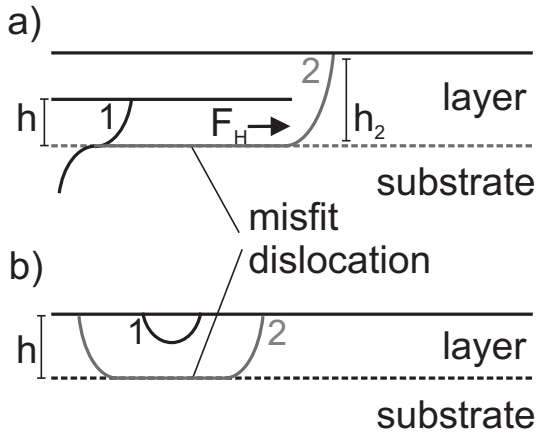

Figure 3.9: Schematic of the Matthews and Blakeslee model for the critical thickness calculation. a) threading dislocations (1) are elongated along the substrate-layer-interface to form a misfit dislocation (2). (b) half-loop dislocations formed on the surface (1) grow towards the interface. Once they have reached the interface they form a misfit dislocation (2). The schematic is reproduced after [36].

pushed along the surface to form a misfit dislocation (see Fig 3.9).

According to Matthews and Blakeslee, F_H and F_D are given by [35]:

$$F_H \simeq G\left(\frac{1+\nu}{1-\nu}\right) bh|f| \tag{3.1}$$

$$F_D \simeq \frac{Gb^2}{4\pi(1+\nu)}\left[\ln\left(\frac{h}{b}\right)+1\right] \tag{3.2}$$

where G is the shear modulus, ν the Poisson ratio (≈ 0.3) and b is the Burgers vector of the dislocation which was assumed to be a 60° dislocation along one of the (110) crystal directions with $b = a_{InAsSb}/\sqrt{2}$. f describes the misfit given by $f = (a_{layer} - a_{sub})/a_{sub}$, where a_{layer} and a_{sub} is the unstrained lattice parameter of the epitaxial layer and the substrate. For $F_H = F_D$ the critical condition is met for the thickness h_c:

$$h_c \simeq \left(\frac{b}{4\pi|f|(1+\nu)}\right)\left[\ln\left(\frac{h}{b}\right)+1\right] \tag{3.3}$$

Equation (3.3) can be solved numerically and the result for InAsSb on GaSb substrates as a function of Sb composition is plotted in Fig 3.10. For the composition lattice matched

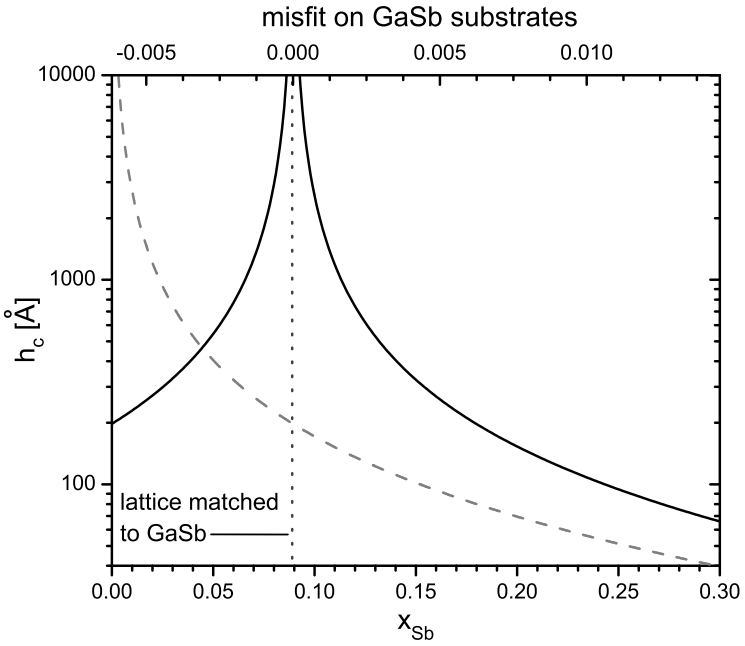

Figure 3.10: Critical thickness calculation for InAsSb as a function of x_{Sb} on a GaSb substrate (solid line) and on an InAs substrate (dashed line). The top axis shows the misfit of InAsSb on a GaSb substrate. The dotted line indicates the alloy composition with the same lattice constant as GaSb.

to GaSb, $x_{Sb} \approx 0.09$, the critical thickness is ∞, while for InAs it is ≈20 nm and for $InAs_{0.75}Sb_{0.25}$ it is ≈10 nm. However, the experimentally determined critical thicknesses are typically higher than those calculated by Eq 3.3, especially at the low growth temperatures used here, where dislocation glide velocities are low. Under the present growth conditions InAs on GaSb could be grown as thick as 26 nm within a strained balanced superlattice without detection of any relaxation by XRD, AFM or TEM. At the same time one has to note, that in XRD misfit dislocations densities can only be detected when the density is high enough to lead to a peak shift in the spectra. AFM and TEM measurements are in principle able to detect single dislocations, but the for AFM measurements the surface has to be smooth to the scale of mono-layers and with TEM only very a small sample area is probed at a time.

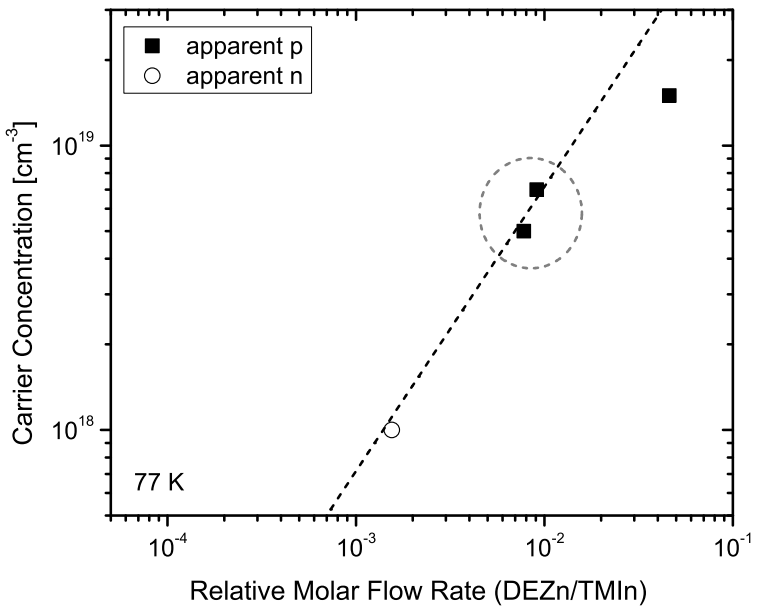

Figure 3.11: 77 K Hall measurements of InAsSb:Zn layers grown on GaAs semi-insulating miscut substrates. The measured carrier concentration is plotted as a function of relative DEZn molar flow. The dashed line is a linear fit through the origin of the data points in the circled area, and was used to extrapolate the flows needed for lower doping values. The carrier concentration saturates at really high doping levels $> 1 \times 10^{19}$ cm^{-3}. Due to the electron accumulation layer on the surface, p-type layers appear n-type below a certain carrier concentration, as the surface layer dominates the conduction.

3.3 Doping of InAsSb

Doping calibrations of InAsSb were always carried out on GaAs semi-insulating substrates, as GaSb typically is not electrically insulating enough. Thus the layers for doping calibration are fully relaxed and their carrier mobility is decreased. Hall measurements on InAsSb are challenging as InAsSb forms an electron accumulation layer at the surface. This accumulation layer can dominate the Hall results, especially for p-type material having lower hole mobilities. Even heavily doped p-type layers can appear as n-type. Typically the accumulation layer has a sheet density of 1×10^{13} cm^{-2} and a mobility of 2000 cm^2/(Vs) [37]. For example, at room temperature a p-type layer with a doping of 1×10^{17} cm^{-2} and a mo-

bility of 300 $cm^2/(Vs)$ needs to have a thickness > 7 μm to have a conductivity comparable to the surface sheet conduction. For 77 K, the bulk mobility increases, while the mobility of the accumulation layer is expected to stay the same and thus measurements at liquid nitrogen temperature were also conducted. When the mobility and carrier density of the surface layer are known, the bulk values can be calculated from the apparent or measured values according to the 2 channel model of Nedoluha and Koch [38]. The bulk and surface layer properties can also be determined by a series of Hall measurements at different B-fields in addition to magneto resistance measurements [37].

In this work however, a series of highly doped samples with thicknesses between 0.6 μm and 1.2 μm were grown and the DEZn flows for lower doping calibrations were linearly extrapolated as shown in Fig 3.11. Note that for doping levels above 1×10^{19} cm^{-3}, the Zn incorporation saturates and the carrier concentration versus DEZn flow deviates from the linear relationship. Below a certain doping and thickness combination the values will again deviate from the linear relationship according to the Hall measurements, when the surface layer conductivity is approached. Often n-type behaviour is measured despite the fact that the bulk layer is doped p-type as shown by the open symbol in Fig 3.11.

InAsSb is typically n-type when grown by OMVPE even without deliberate doping.In this work this is referred to as non-intentionally doped (nid). In the diode designs tested initially, the n-doping level was supposed to be as low as possible and thus nid InAsSb layers were grown. Again, measuring the bulk carrier concentration for low doping levels by Hall is challenging due to the surface conduction layer. Thick layers are needed even though the reported mobilities for n-type doping levels of 1×10^{16} cm^{-3} typically exceed 1×10^4 $cm^2/(Vs)$ at 77 K [39]. However, the carrier concentration could be determined with a C-V measurement of a p^+InPSb/n^-InAsSb heterojunction diode (for details see chapter 6). A carrier concentration of n=1.7×10^{15} cm^{-3} was determined at 77 K. Note that the non linear C-V curve for negative bias values is not a sign of a change in the doping level here. It is due to full depletion of the InAsSb layer between the p-InPSb and the electron accumulation layer in InAsSb at the n-InAsSb/n-GaSb heterojunction. A band diagram of this structure is plotted in Fig 6.2.

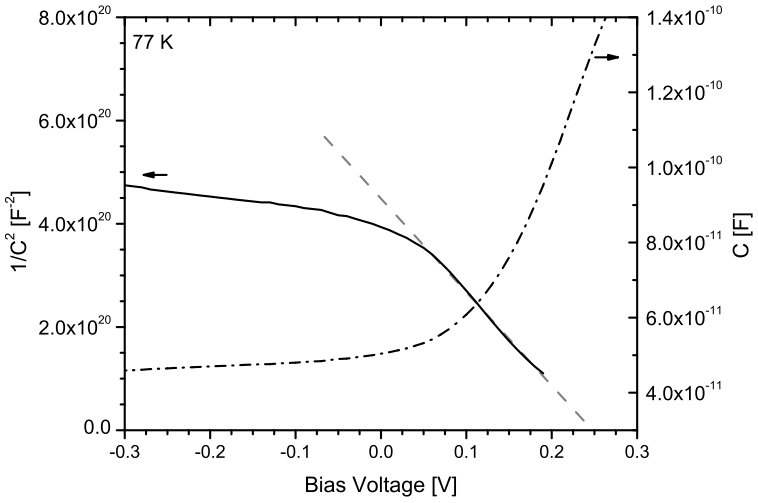

Figure 3.12: 77 K C-V measurement of a p^+InPSb/n^-InAsSb heterojunction diode. The device is a square mesa structure with a side length of 410 μm. The InAsSb nid layer is depleted, thus $1/C^2$ can only be interpreted by the standard method (Sec 2.4.1) in the low positive bias range. For higher positive biases, the current is too high for the capacitance meter. The dashed line is a fit to the linear part of the curve. The C-V measurement results in a doping level of the InAsSb of n=1.7×10^{15} cm^{-3}. The dash-dotted line shows the capacitance as a function of bias voltage.

Chapter 4

n-InAsSb n-GaSb Heterojunctions

The InAsSb/InAs strain-balanced detector superlattice is grown on an InAsSb buffer layer which is lattice matched to the GaSb substrate. Due to the extreme band offset between $InAs_{0.91}Sb_{0.09}$ and GaSb, a parasitic rectifying junction can be formed under certain doping conditions as shown earlier by Srivastava et al. [40] or by Mebarki et al. [41]. For the superlattice detector concept presented in this work, a rectifying junction at the wafer interface is not desired (for a SL detector schematic see Fig. 1.5e&f). In this chapter, the junction properties are explored as a function of the GaSb n-doping level. The main results presented here have previously been published in Lackner et al. [42].

4.1 I-V Characterizations & Band Line-up Simulations

The samples were grown on GaSb:Te 2° miscut towards (111)B wafers. A 500 nm GaSb:Te layer was grown at 540°C, then the wafer was cooled to 500°C under a low TBAs flow, and a 500 nm layer of non intentionally doped (nid) $InAs_{0.91}Sb_{0.09}$ was grown lattice matched to GaSb (see Fig 1.5b). The growth rate for both layers was 3 Å/s and the V/III ratio was 4.5 in the case of GaSb and and 6 for the InAsSb layer where the TMSb/V ratio was 0.18.

Three device structures, grown with different GaSb doping levels of 8×10^{16} cm^{-3}, 5×10^{17} cm^{-3} and 2×10^{18} cm^{-3}, were studied. The doping of the nid InAsSb layers is n-type and was determined to be $\leq 5 \times 10^{16}$ cm^{-3} by Hall measurements of InAsSb grown on GaAs under similar conditions. The n-n heterojunction devices were processed into circular mesas using standard photolithography and etching methods. The InAsSb layer

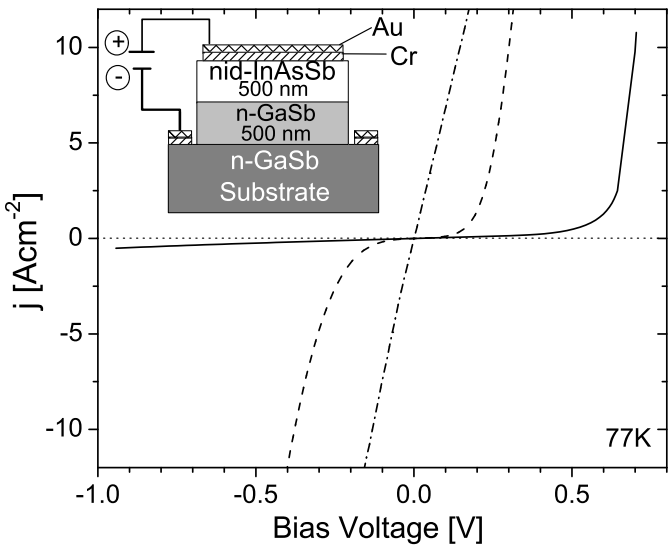

Figure 4.1: I-V curves for three different n-GaSb doping levels (solid: 8×10^{16} cm^{-3}, dash: 5×10^{17} cm^{-3}, dash-dot: 2×10^{18} cm^{-3}) at 77 K. The junction area is 9×10^{-4} cm^2. The inset shows a schematic drawing of the measured devices.

was etched with a citric acid based etch (citric acid:H_2O_2(30%) = 2:1),while the GaSb layer was etched with a tartaric acid based etchant ($C_4H_4KNaO_6$:H_2O:HCl(37%):H_2O_2 = 15 g:200 ml:160 ml:14 ml) as described in detail by Dier et al. [43]. The citric acid was gained by mixing 1 ml H_2O with 1 g of citric acid crystals. No surface passivation treatment was used. Annealing of the evaporated Cr/Au (50 nm/150 nm) contacts at 200°C for 5 min ensured ohmic contacts to both semiconductors. A schematic view of the device is shown in the inset of Fig 4.1.

For the photoresponse measurements, a Bomem DA8 Fourier transform spectrometer with a globar light source was used. The devices used for the optical measurements have a window in the metal contact on top of the InAsSb layer. The photo-generated current was converted to a voltage and recorded as a function of photon energy.

The electrical behaviour of this junction is controlled by the doping level of the GaSb layer. Fig 4.1 shows the I-V curves at 77 K for the differently doped samples. The lightly doped sample (8×10^{16} cm^{-3}) shows strong rectification, while the highly doped sample (2×10^{18} cm^{-3}) shows a linear current dependence on the voltage.

GaSb doping (cm^{-3})	R_0A (Ωcm^2)	
	77 K	300 K
8×10^{16}	4540	143
5×10^{17}	1.4	0.6
2×10^{18}	0.02	0.0005

Table 4.1: Typical R_0A values for the different GaSb doping levels

To quantify the rectification here, the zero-bias resistance area product (R_0A) was measured. R_0A is defined as:

$$R_0A = \left(\frac{\mathrm{d}j}{\mathrm{d}V}\right)^{-1}_{|V=0} \tag{4.1}$$

with j being the current density and V the voltage applied to the device. At 77 K, typical values of R_0A range from 4500 Ωcm^2 for the lowest GaSb doping concentration to 0.02 Ωcm^2 for the highest doping concentration. The R_0A values are tabulated in Table 4.1. At room temperature, values range from 143 Ωcm^2 to 0.0005 Ωcm^2 in case of the highest doping. For comparison, the R_0A at 300 K of a Zn-diffused p^+-n GaSb unpassivated photodiode with a n-type doping of $3-5\times10^{17}$, was measured to be 46 Ωcm^2 [44].

The behaviour of these devices can be understood by simulating their band structure. Energy band diagrams were computed using a self-consistent energy band simulation code: Nextnano^3 [45]. Standard input parameters were used, with the exception of the InAsSb bowing parameter of the split-off band, which was set to zero, according to Cripps et al. [46]. In the simulation, all doping atoms were forced to be ionized. The band offsets were computed within the program according to the model-solid theory as described by van de Walle [47]. A more detailed description of this approach can be found in Sec. 5.2 and the parameters are summarized in Table 1.

Due to the staggered type II band alignment, which is plotted in Fig 4.2, an accumulation layer is formed on the InAsSb side of the junction and a depletion region occurs on the GaSb side. The band line-up for the lightly doped GaSb layer (8×10^{16} cm^{-3}) is plotted in Fig 4.3. The InAsSb n-type carrier concentration was assumed to be 5×10^{15} cm^{-3}.

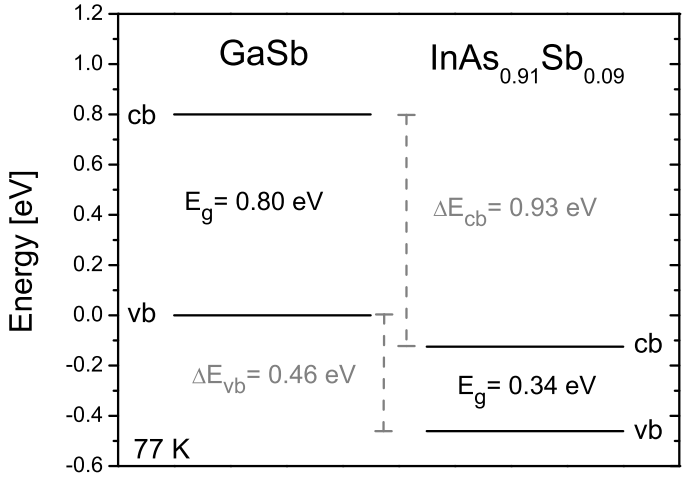

Figure 4.2: Energy gaps and bandoffsets for $InAs_{0.91}Sb_{0.09}$ and GaSb at 77 K are shown.

This band line-up is very similar to the case of a n-GaSb/Au Schottky-diode as depicted in Fig 2.19 and thus similar properties such as rectification are expected and were measured. In the n-InAsSb/n-GaSb case, the height of the electron barrier, and more so, the width are governed by the GaSb doping level. With increasing doping of the GaSb side, the barrier is reduced and narrows, and the tunneling current becomes dominant, which eventually results in a linear I-V dependence. In Fig 4.4 the band-structure simulation for the highly doped GaSb layer (2×10^{18} cm^{-3}) is shown.

4.2 C-V Characterization

Figure 4.5 shows the C-V measurement results for the 8×10^{16} cm^{-3} doped sample at liquid nitrogen and at room temperature. For the samples having higher doping levels, the leakage current was too high for the capacitance meter to operate. When plotting the inverse of the squared capacitance as a function of bias voltage, the data points should form a straight line when the doping level is constant. The intercept of this line with the voltage axis is the built-in potential (V_{bi}, see section 2.4.1). In Table 4.2, the measured values are compared to the simulated ones and to previous results found in literature.

The measured built-in voltages agree reasonably well with the simulation, although the

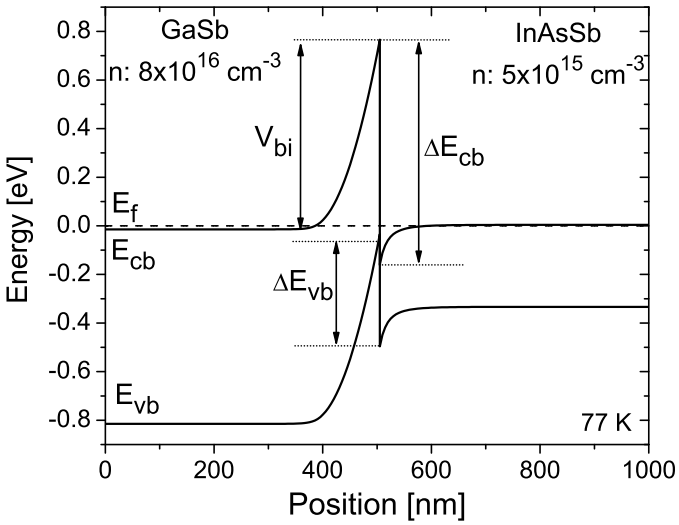

Figure 4.3: Simulation of the band line-up for the GaSb/InAsSb heterojunction at 77 K. The doping of the GaSb layer is 8×10^{16} cm^{-3} and the substrate is not included in the simulation.

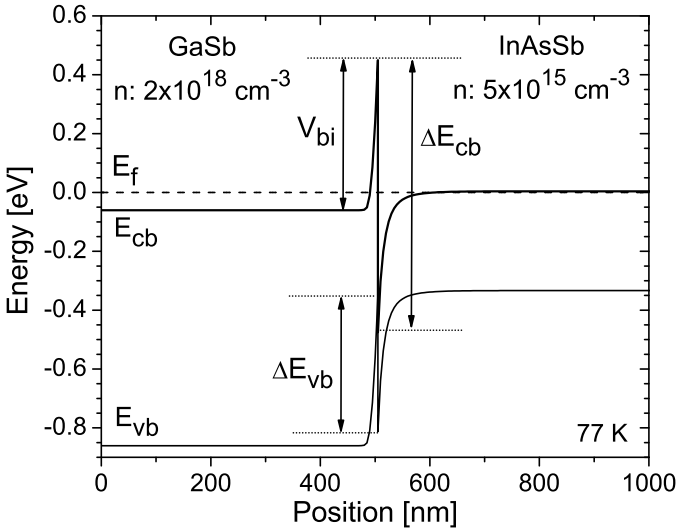

Figure 4.4: Simulation of the band line-up for the GaSb/InAsSb heterojunction at 77 K. The doping of the GaSb layer is 2×10^{18} cm^{-3} and the substrate is not included in the simulation.

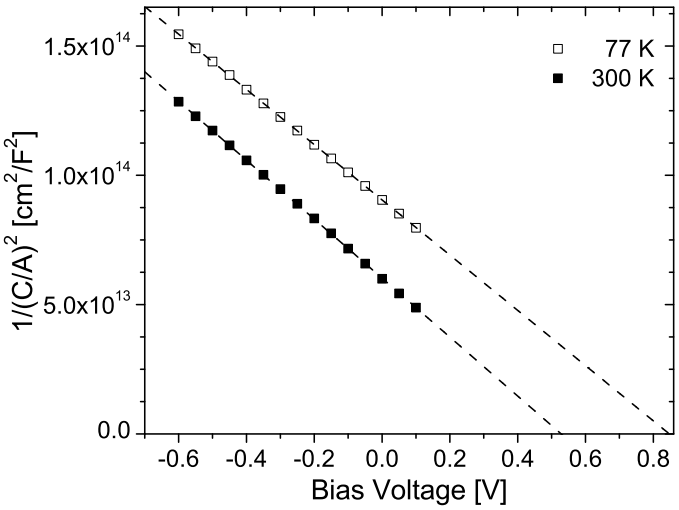

Figure 4.5: C-V measurement of the lowest doped device (8×10^{16} cm^{-3}) at 300 K (filled squares) and 77 K (open squares) at 1 MHz. The junction area is 9×10^{-4} cm^2. The voltage axis intercepts of the linear fits are at 0.53 V (300 K) and 0.85 V (77 K).

GaSb	V_{bi} (V)					
doping	measured		simulation		Mebarki [41]	Srivastava [40]
(cm^{-3})	77 K	300 K	77 K	300 K	77 K	300 K
8×10^{16}	0.85±0.02	0.53±0.02	0.78	0.60	-	-
5×10^{17}	-	-	0.65	0.57	0.82±0.02	0.77±0.02
2×10^{18}	-	-	0.51	0.45	-	-

Table 4.2: Comparison of V_{bi} results of C-V measurements and simulation

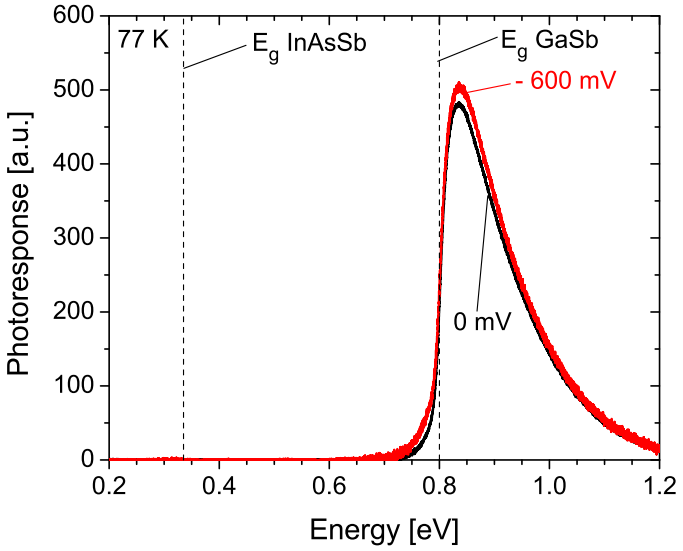

Figure 4.6: Detector response as a function of optical excitation energy at 77 K under zero bias and reverse bias conditions of a sample with a junction area of 5.7×10^{-3} cm^2 and a GaSb:Te doping level of 8×10^{16} cm^{-3}. Dashed vertical lines indicate the energies of the InAsSb and GaSb band-gaps. No response from the InAsSb layer is detected.

simulation slightly underestimates the temperature dependence. Previous measurements of V_{bi} at higher GaSb doping levels by Mebarki et al. [41] and Srivastava et al. [40], shown in Table 4.2, gave significantly higher values compared to the simulation. A reason for this could be the interface between the GaSb and InAsSb layer. In both cases, the InAsSb was grown directly on the GaSb substrate, and therefore contamination, especially with oxygen, is extremely likely. In the present experiment, this was avoided by the growth of the epitaxial GaSb layer. However, the heterojunction interface is still problematic and hard to grow abruptly by OMVPE. In chapter 3, strain fields due to Ga segregation into the first few monolayers of the InAsSb were reported.

4.3 n-InAsSb n-GaSb Heterojunctions Photoresponse

We have measured the sample with the lowest doping level (8×10^{16} cm^{-3}) in a photodetector setup under different bias conditions at 77 K. As discussed above, the bias definition

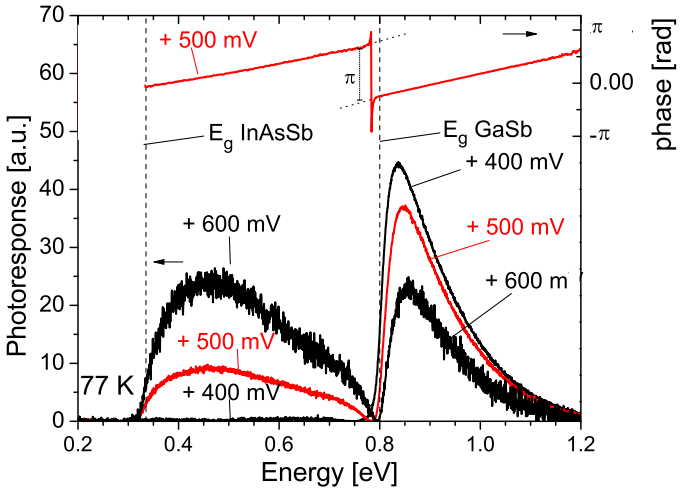

Figure 4.7: Detector response as a function of optical excitation energy at 77 K under high forward bias condition of a sample with a junction area of 5.7×10^{-3} cm^2 and a GaSb:Te doping level of 8×10^{16} cm^{-3}. Dashed vertical lines indicate the energies of the InAsSb and GaSb band-gaps. Above, connected to the right axis, the phase information of the Fourier transform of the +500 mV data is plotted. The phase jump of π close to the GaSb band-gap is experimental evidence that the photogenerated currents from the InAsSb and the GaSb layers have opposite signs.

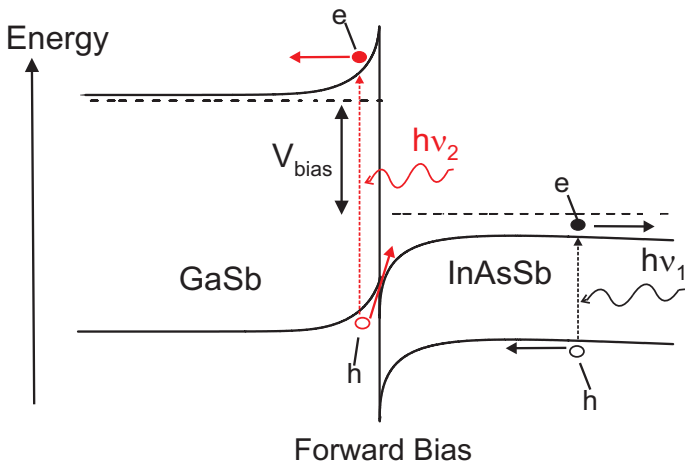

Figure 4.8: Schematic of the proposed two color detection mechanism at forward bias.

is analogous to the usual convention of a metal/n-GaSb Schottky device. Here, the InAsSb accumulation layer acts like the metal layer and so the positive terminal is connected to the InAsSb layer for forward bias. Sharabani et al. [48] found that by changing the bias voltage [1] in an n-GaSb/n-InAsSb heterojunction device with a GaSb doping of 1×10^{18} cm^{-3}, the device can be used as a two color detector. We report qualitatively similar behavior here, but with a much simpler explanation. Fig 4.6 shows the detector response at 77 K under zero and negative bias conditions. No photoresponse from the InAsSb layer can be detected. This is expected from the band diagram (see Fig 4.3), as there is no built-in field to extract the carriers from the InAsSb layer. However, due to the built-in potential in the GaSb layer, the device is expected to work in a manner similar to a metal semiconductor Schottky photodetector. Note that photo-generated holes are swept to the heterojunction interface and can recombine at equal energy with electrons in the InAsSb. This explains the photovoltaic current response above 0.7 eV that is slightly increasing with increasing negative bias voltages.

With increasing forward bias, shown in Fig 4.7, the photocurrent from the GaSb layer decreases as the potential barrier is lowered. At bias voltages above +400 mV, response from the InAsSb layer can be detected, with the photocurrent increasing with increasing forward bias voltage. This behavior indicates that there are different photocurrent mecha-

[1] Note that their bias definition is opposite to the usual convention.

nisms in the two different materials. It is assumed that, as for reverse bias, the photocurrent in the GaSb is due to the photovoltaic effect. This current gets weaker as, the effective potential and also the depletion width are reduced with increasing forward bias. Above a certain forward bias voltage, the InAsSb layer acts as a photoconductor. Here, both the accumulation layer of electrons in InAsSb at the junction and the barrier for the holes travelling towards the GaSb are reduced, so electron-hole pairs generated optically in the region before the accumulation layer at the junction are swept out by the weak external field in the InAsSb region. This is schematically depicted in Fig 4.8. Thus the direction of the photogenerated current from the InAsSb region is opposite to the one generated in the GaSb, but is in the same direction as the forward bias diffusion current.

The change in sign of the current is not reflected in the photoresponse at the bottom of Fig 4.7, since the Fourier transform software assumes the signal to be an intensity, everywhere positive, and generates a phase versus energy file which is used during the Fourier transform to produce this result. This phase versus energy information is plotted at the top of Fig 4.7. Its sudden change by π radians just below the GaSb bandgap, where the photoresponse dips to zero, verifies that the current changes sign at this energy. The signal drops to zero just below the GaSb bandgap, since at this point both currents have reached equal magnitude but cancel due to opposite directions. Thus under high forward bias, the junction can be driven as a two color detector. Unfortunately due to the high current, in the forward bias condition, the signal is very noisy. The explanation of the two color detector mechanism given here is completely different from the one given by Sharabani et al. [49], where both photogenerated currents would have the same direction.

In Summary, the important point of this chapter is that an unwanted rectifying junction at the n-InAsSb/n-GaSb interface can be avoided only when the InAsSb bulk or superlattice detector structure is grown on highly doped n-type GaSb ($> 5 \times 10^{17}$ cm^3). Then contacts can be made to the GaSb substrate and the p-doped top layer.

Chapter 5

Photoluminescence Results

In this chapter photoluminescence (PL) results from InAsSb/InAs superlattice samples are discussed. First it is shown how strain balancing can be achieved. The so called "model-solid" theory is reviewed since it presents a way to calculate the band-offsets between different semiconductors and include the effects of strain on the band energy levels. Then the theory is compared to the experimental results. Parts of the experimental PL results presented in this chapter were previously published in Ref. [50].

5.1 Strain Balancing

One advantage of the strain balanced superlattice approach is the fact that it is possible to grow thick layer structures (several microns) without dislocations due to strain relaxation. Further, in the case of InAsSb/InAs on GaSb, strain balancing can be achieved for Sb compositions $> 9\%$. As every single layer is highly strained, the first constraint is that every single layer thickness must be below the critical thickness. In the case of InAs on GaSb, that limit is just above 20 nm and for InAsSb it depends on the composition as described in chapter 3.

The strain balancing concept applied here, is that the weighted average lattice constant $\overline{a}$ over one period is equal to the lattice constant of the substrate a_{sub}.

$$a_{sub} = \overline{a} = \frac{\sum_i t_i a_i}{\sum_i t_i} \qquad \text{with} \qquad \sum_i t_i = P, \tag{5.1}$$

where t_i is the thickness of the i-th layer within one period and P denotes the thickness of one period. The lattice parameters a_x for the different binary materials can be found in table 2.2 and the ternary lattice constant is calculated by the linear interpolation between the lattice constants of the binary constituents InAs and InAsSb. For example, for a superlattice with an $InAs_{0.821}Sb_{0.179}$ and an InAs layer, equation 5.1 is fulfilled when the two layers have the same thickness.

For the case of an $InAs_{1-x}Sb_x$ strain balanced superlattice on GaSb, this leads to a simple expression for the thickness of the InAsSb (t_{InAsSb}) as a function of the antimony content (x) and period (P) :

$$t_{InAsSb} = \left(\frac{a_{GaSb} - a_{InAs}}{a_{InSb} - a_{InAs}}\right)\left(\frac{P}{x}\right) = 0.090\left(\frac{P}{x}\right) \tag{5.2}$$

When growing the superlattice, it is more stable to start with a half layer, so that the average lattice mismatch as a function of thickness oscillates around zero, rather than from zero to the extreme value and back.

The strain balancing concept is graphically displayed in Fig 5.1. Here, an optical *in situ* wafer curvature measurement during a 6 period SLS layer growth on GaSb is plotted. The change in wafer curvature due to the misfit stress has opposite sign for the different materials. Growing a strained layer on the substrate results in an asymmetric stress relative to the bottom and the top surface of the wafer which results in bending the wafer. For perfect strain balancing, the average slope would be zero. Here however, the Sb composition of 0.22 is slightly too high for the chosen layer thickness ratio of 1, which resulted in the the slight upward slope on average.

5.2 Calculation of Band Offsets

It is extremely important to be able to predict the band discontinuities, or band offsets between the layers of different materials, for complex optical devices or, as in our case, to simulate the optical transition energy of a strain balanced superlattice. A successful and practical way to calculate band lineups in most semiconductors is the so-called “model-solid theory” proposed by Van de Walle [47]. It is based on the idea, that an absolute energy position of the valence band of the bulk material, the so called vacuum level of the valence band, can be calculated by performing density-functional calculations for every

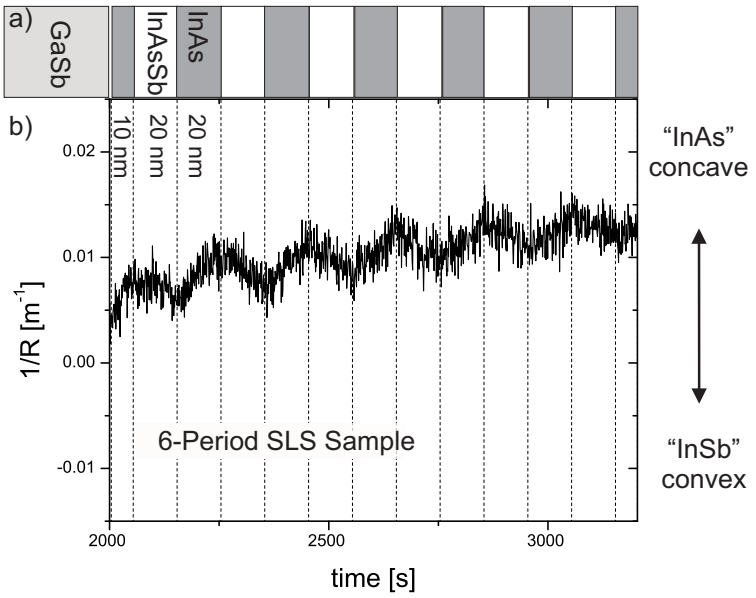

Figure 5.1: a) Layer schematic of a 6 period SLS structure with x_{Sb}=0.22 in the InAsSb layers and a period of 40 nm and. The InAsSb and InAs layers have equal thicknesses. b) *In situ* curvature measurement: The inverse curvature radius is plotted as a function of growth time which is proportional to the layer thickness. The plot shows the strain balancing, as the slopes of the two different layers have opposite signs. However, since the graph has a positive slope on average, it is evident that, there is too much Sb in the InAsSb layers or the layer thicknesses need to be adjusted.

binary semiconductor in its unstrained state. The position of the conduction band is derived from measurements of the bandgap, which is regarded as more precise than the calculated bandgap. To calculate the exact valence band edge, the interaction of the three valence bands and the influence of strain is included afterwards. A short description of how to calculate the band gaps and offsets for an InAsSb/InAs SL strained on a GaSb substrate based on the van de Walle picture [47] is provided below.

The band diagram simulations presented within this work were calculated with the simulation program nextnano^3 [45] which makes use of the van de Walle formalism to determine the band discontinuities. The material parameters used are listed in Table 1. Also original band offset calculations based on the treatment below, which are in agreement with the results from the simulation tool, will be presented later.

5.2.1 Strain Calculation of Pseudomorphic Layers

Pseudomorphic growth results in strained layers in most cases. This strain results in energy band shifts which can be calculated based on the strain tensor in conjunction with the deformation potentials of the materials. Note that the treatment below is only carried out for zincblende crystal materials grown along the (001) crystal axis which will be referred to as z-direction. The biaxial strain of the grown layer can be described by the strain tensor (ϵ_{ij}).

$$\epsilon_{ij} = \begin{pmatrix} \epsilon_{xx} & 0 & 0 \\ 0 & \epsilon_{yy} & 0 \\ 0 & 0 & \epsilon_{zz} \end{pmatrix} \tag{5.3}$$

To calculate the components of ϵ_{ij} of the grown material, the strained lattice parameters of the epilayer have to be determined. For pseudomorphic growth, the lattice parameter of the epilayer parallel to the growth surface is the same in the x-direction (a_{Lx}) and the y-direction (a_{Ly}) and identical to the lattice parameter of the substrate (a_s). The unstrained lattice parameter of the epitaxial layer is denoted as a_L. The out-of-plane lattice component (a_{Lz}) can then be calculated by

$$a_{Lx} = a_{Ly} = a_s \tag{5.4}$$

$$\text{and} \qquad a_{Lz} = a_L \left(1 - D_L^{001} \left(\frac{a_s - a_L}{a_L}\right)\right) \tag{5.5}$$

where the constant D^{001} depends on the elastic constants of the material of the layer through

$$D^{001} = 2\frac{c_{12}}{c_{11}}. \tag{5.6}$$

The elastic constants of the materials as well as the lattice parameters used in this work are tabulated in Table 2.2.

Now the components of the strain tensor can be computed as

$$\epsilon_{xx} = \epsilon_{yy} = \frac{a_s - a_L}{a_L} \tag{5.7}$$

$$\epsilon_{zz} = \frac{a_{Lz} - a_L}{a_L} \quad . \tag{5.8}$$

5.2.2 Calculation of the Valence Band Edges

In the case of an unstrained layer, the top of the valence band at the Γ-point (E_v) is degenerate and consists of the heavy and light hole bands. Since the spin-orbit coupling was not included in the calculation of the vacuum valence band level of the valence band ($E_{v,vac}$), E_v is calculated from $E_{v,vac}$ together with the spin-orbit splitting (Δ_0):

$$E_v = E_{v,vac} + \frac{\Delta_0}{3} \quad . \tag{5.9}$$

For a strained layer, $E_{v,vac}$ is shifted due to the biaxial strain in the xy-plane, which corresponds to a volume change of the unit cell ($\Delta\Omega$). The change in $E_{v,vac}$ is given by:

$$\Delta E_{v,vac} = a_v \frac{\Delta\Omega}{\Omega} \tag{5.10}$$

Note that a_v here describes the hydrostatic deformation potential of the valence band and not a lattice parameter. The relative change in unit cell volume is related to the strain tensor ϵ_{ij} by [47]:

$$\frac{\Delta\Omega}{\Omega} = Tr(\epsilon_{ij}) = \epsilon_{xx} + \epsilon_{zz} + \epsilon_{zz}. \tag{5.11}$$

In addition the effect of the band splitting needs to be taken into account. In the case of compressive strain, the heavy hole (hh) band moves up and the light hole (lh) moves down,

while for tensile strain the opposite happens and thus the light hole band becomes the highest valence band. The energy shifts of the heavy hole, light hole and split-off band, including the spin orbit coupling, relative to the strain adjusted vacuum level ($E_{v,vac} + \Delta E_{v,vac}$) are [47]:

$$\Delta E_{v,hh} = \frac{1}{3}\Delta_0 - \frac{1}{2}\delta E_{001}, \tag{5.12}$$

$$\Delta E_{v,lh} = -\frac{1}{6}\Delta_0 - \frac{1}{4}\delta E_{001} + \frac{1}{2}(\Delta_0^2 + \Delta_0\delta E_{001} + \frac{9}{4}\delta E_{001}^2)^{1/2}, \tag{5.13}$$

$$\text{and} \qquad \Delta E_{v,so} = -\frac{1}{6}\Delta_0 - \frac{1}{4}\delta E_{001} - \frac{1}{2}(\Delta_0^2 + \Delta_0\delta E_{001} + \frac{9}{4}\delta E_{001}^2)^{1/2}. \tag{5.14}$$

δE_{001} is given by:

$$\delta E_{001} = 2b(\epsilon_{zz} - \epsilon_{xx}) \tag{5.15}$$

where b is the shear deformation potential of the semiconductor.

For the binary materials of interest in this work, the lattice parameters and elastic constants are listed in Table 2.2, while all other material parameters are in Table 5.1.

To calculate the valence band lineup, one calculates the absolute energy level of the band edge E_v starting from the vacuum level of the conduction band $E_{v,av}$ as listed in Table 5.1 and either adds the effects of the spin orbit coupling (Eqn. 5.9) for the unstrained case or the effect of the biaxial strain on the vacuum level (Eqn. 5.10) and the band shifts (Eqn. 5.12) as follows:

$$E_v = E_{v,vac} + \frac{\Delta_0}{3} \qquad \text{unstrained} \tag{5.16}$$

$$E_v = E_{v,vac} + \Delta E_{v,vac} + \Delta E_{v,hh} \qquad \text{compressive strain} \tag{5.17}$$

$$E_v = E_{v,vac} + \Delta E_{v,vac} + \Delta E_{v,lh} \qquad \text{tensile strain} \tag{5.18}$$

$$\tag{5.19}$$

The valence band discontinuity ΔE_v between semiconductors A and B can now be computed:

$$\Delta E_v = E_v^B - E_v^A \tag{5.20}$$

The sign convention is that if $\Delta E_v > 0$, then the valence band of B is higher in energy than the valence band of A.

	Δ_0 [eV]	$E_{v,vac}$ [eV]	a_v [eV]	$E_{g,0}$ [eV]	α [meV/K]	β [K]	a_c [eV]	b
GaSb	0.76	-6.25	-0.8	0.812	0.417	94	-7.5	-2
InAs	0.39	-6.67	-1	0.417	0.276	93	-5.08	-1.8
InSb	0.81	-6.09	-0.36	0.35	0.32	170	-6.94	-2

Table 5.1: Parameters for band offset calculations. The parameters are taken from Ref. [4] with the exception of $E_{v,vac}$ from Ref. [47]. The values for $E_{g,0}$ are at 0 K and the full temperature dependence can be calculated with the Varshni parameters:$E_g(T) = E_{g,0} - \alpha T^2/(T+\beta)$.

5.2.3 Calculation of the Conduction Band Edge Energies

The absolute energy level of the conduction band minimum E_c for the unstrained material is found by adding the experimentally determined low temperature band gaps (E_g) to the energy of the valence band maximum:

$$E_{c,vac} = E_{v,vac} + \frac{\Delta_0}{3} + E_g \tag{5.21}$$

In the case of a strained layer, the conduction band shifts similarly to the vacuum level of the valence band by the amount:

$$\Delta E_{c,vac} = a_c \frac{\Delta\Omega}{\Omega} \tag{5.22}$$

The hydrostatic deformation potential of the conduction band a_c for the different semiconductors used here are also shown in Table 5.1. The energy position of the conduction band can be calculated by:

$$E_c = E_{c,vac} + \Delta E_{c,vac} \tag{5.23}$$

The band discontinuity of the conduction band is then found in similar manner to the valence band (Eqn. 5.20).

5.2.4 Band Discontinuities of Ternary Layers

In the case of ternary layers, the parameters are interpolated between the two binary constituents. The interpolation is assumed to be linear for most parameters e.g. the lattice constant. However some parameters, like the bandgap, are known to undergo bowing. For a parameter C_{ABC} of a ternary material made of a fraction x of binary AB and $(1-x)$ AC this leads to:

$$C_{ABC} = xC_{AB} + (1-x)C_{AC} - bx(1-x) \tag{5.24}$$

where b is the bowing coefficient. Note that the bowing is defined with a negative sign, thus a positive bowing parameter lowers the value compared to a linear transition.

In this work, a bowing parameter of $b_{Eg} = 0.67$ [4] is used for the bandgap of InAsSb. Unfortunately it is often not known how the bowing is divided between the valence and conduction band levels. Note that if the bowing occurs in the valence band, the sign of the bowing coefficient changes. In section 5.3 it will be shown that the best agreement

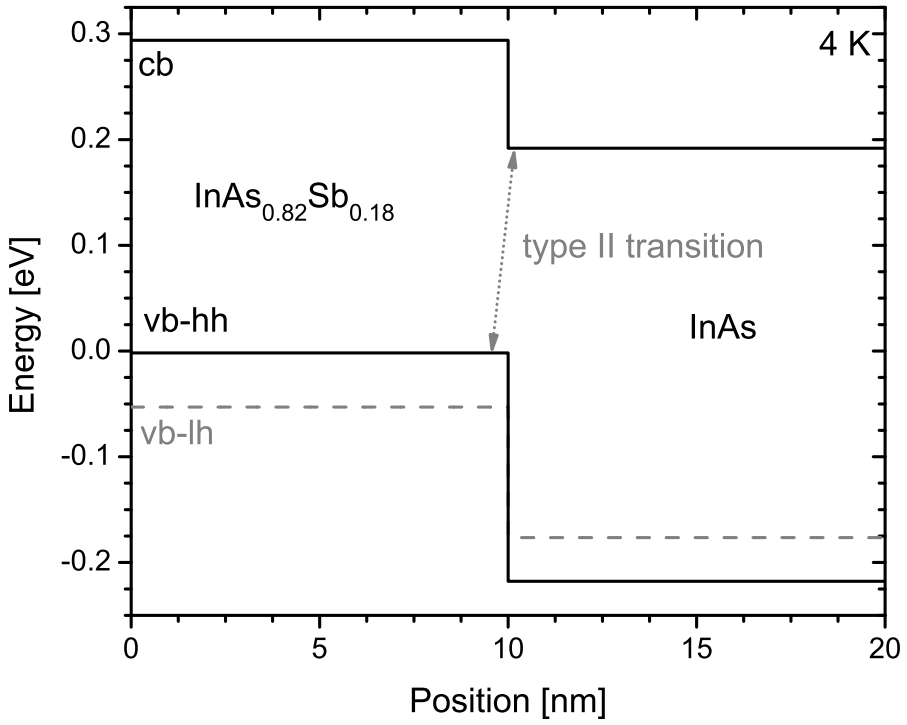

Figure 5.2: Simulated band line-up of $InAs_{0.82}Sb_{0.18}$ and InAs grown pseudomorphically on GaSb at 4 K.

with the presented data for InAsSb can be found when assuming that 30% of the bowing occurs in the conduction band and 70% in the valence band. The calculated band alignment of $InAs_{0.82}Sb_{0.18}$ and InAs at 4 K, strained on a GaSb substrate, is depicted in Fig 5.2 as calculated with nextnano[3]. The theoretical prediction for this band alignment is type II, with the InAsSb bands above the InAs bands (see Fig 5.2).

Originally the calculations regarding the band offsets and thus the type II transition energies were computed directly with the van de Walle procedure as described earlier. Later nextnano[3] was used as it has the van de Walle calculation built-in. It can also solve the Schroedinger equation for the carriers, so that the quantization levels are conveniently calculated as well. Further, the temperature dependence of the lattice parameters is included into the simulation program which was neglected in the original calculations. In Fig. 5.5 both methods are compared to experimental results and a good agreement between the methods and the experiment is found.

5.3 Photoluminescence Results

InAsSb/InAs multi quantum well (MQW) structures grown on InAs and GaAs have been investigated by several groups primarily for emitter applications. However, there are several conflicting reports of the relative band offsets [51–53]. Before this work there were no prior reports of InAsSb/InAs superlattices on GaSb substrates. Also, by measuring the PL energies for several Sb compositions of the InAsSb layers, information regarding the expected cut-off frequency of such a SL detector can be gained.

5.3.1 Photoluminescence of Samples grown on GaSb Substrates

The samples were grown by low pressure OMVPE on GaSb (001) substrates at 500°C. Detailed growth conditions were described in chapter 3. Table 5.2 shows a summary of the samples discussed in this section. All superlattice structures were grown after the deposition of a 50 nm lattice matched $InAs_{0.91}Sb_{0.09}$ buffer layer. The basic repeat period of the superlattices is shown in the inset in Fig. 5.3. It consists of 6 periods of a compressively strained InAsSb layer, typically 20 nm, sandwiched between two half layers of tensile strained InAs, typically 10 nm (samples 1-5). For this combination of layer thicknesses,

sample	x_{Sb} (%)	1/2 t_{InAs} (nm)	t_{InAsSb} (nm)	$\overline{\epsilon}_{xx}$ (%)
1	13.8	10	20	0.14
2	15.7	11	22	0.08
3	16.8	10	21	0.03
4	17.4	10	20	0.02
5	20.8	10	21	-0.11
6	26.7	13	13	0.01

Table 5.2: Summary of the samples investigated. t denotes the layer thickness, while $\overline{\epsilon}_{xx}$ is the average strain per period. A sample schematic is shown in the inset of Fig 5.3.

perfect strain balance should be achieved at 18% Sb mole fraction in the InAsSb layer. Sample 6 had an InAsSb composition of x=0.267 (Sb) and a reduced layer thickness of 12 nm to avoid strain relaxation. The thickness of the InAs 1/2 layers was increased to 13 nm to achieve approximate strain balance. The average strain of the superlattice structures is given in the last column of table 5.2. The structural quality, thickness and composition of every sample were determined from HR-XRD measurements.

A Bomem DA8 Fourier transform spectrometer with a liquid nitrogen cooled HgCdTe photodetector (12 μm cutoff wavelength) and a KBr beamsplitter was used to obtain the PL spectra. The samples were mounted strain free in liquid He at 4.2 K. The PL spectra were collected using a frequency doubled Nd:YVO_4 laser excitation at 532 nm and 200 mW of CW power in a 3 mm diameter spot size. Blackbody radiation was rejected by chopping the laser at 3 kHz and using a phase sensitive detector as input to the interferometer.

In order to determine the compositional range over which the strain balanced approach can be applied, we have performed a Matthews-Blakeslee calculation [35] of the critical thickness for a single InAsSb QW. The result is shown in Fig 5.3. The limiting factor is the critical thickness of InAs on GaSb which is calculated to be $\approx$20 nm. This calculation is usually found to underestimate the critical value and with the growth conditions as described we have produced InAs layers with a thickness of 27 nm without misfit dislocations. The samples are plotted on this figure (crosses). None of the samples showed crosshatch, a rectangular pattern on the surface due to misfit dislocations, by AFM or broadening in XRD scans despite the fact that several of the samples contained InAsSb layers with thicknesses

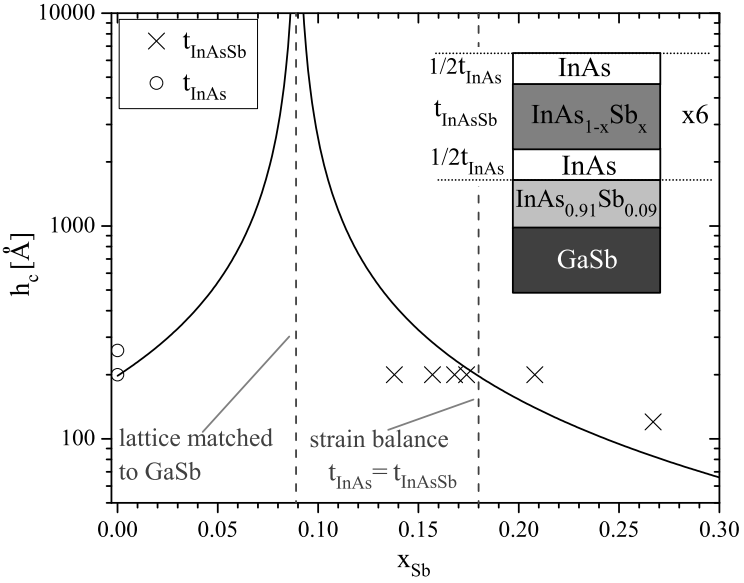

Figure 5.3: Matthews-Blakeslee calculation [35] of the critical thickness for InAsSb grown on a GaSb substrate as a function of Sb content. The individual layers of the superlattices discussed here are marked. The inset shows a schematic of the layer structure.

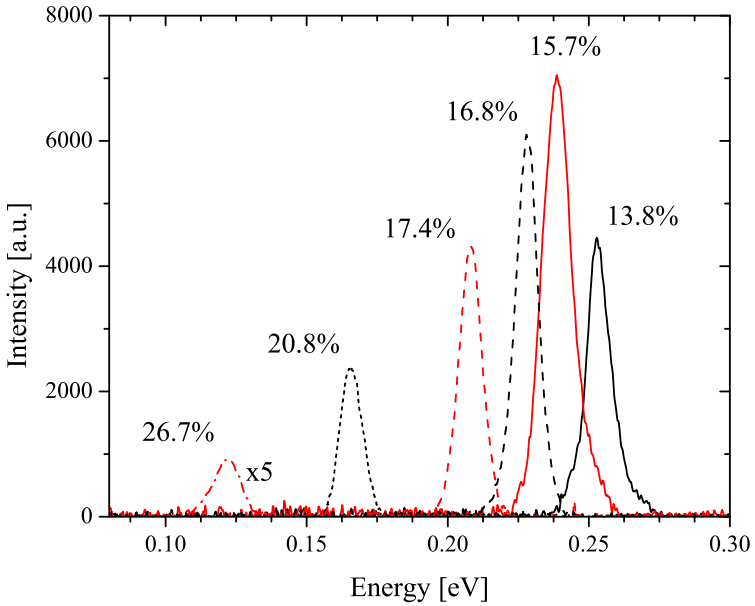

Figure 5.4: The figure shows the PL spectra for every sample at 4 K. The Sb composition of the InAsSb QWs is shown. There is a trend for the peak intensity to decrease with increasing Sb mole fraction with the exception of the sample with 13.8% Sb.

somewhat above the Matthews-Blakeslee criterion.

Fig. 5.4 shows the PL spectra for every sample at 4 K. Every peak is denoted by the Sb mole fraction in the InAsSb layers of the InAs/InAsSb superlattice. The sample with 26.7% Sb wells shows a remarkably low emission energy of 0.122 eV, corresponding to a wavelength of 10 μm. In Fig. 5.5 the experimental PL peak energies are plotted versus the Sb content. These are compared to the calculated band gap of unstrained InAsSb [11] (solid line). The calculated strained bandgap (E_c-E_{hh}) for compressively strained InAsSb (x_{Sb} >0.09) and (E_c-E_{lh}) for tensile strained InAsSb (x_{Sb} <0.09) of InAsSb pseudomorphically grown on GaSb substrates is plotted as a dotted line. The change of the bandgap with strain was calculated using nextnano^3 [45] with the parameters as tabulated in Table 1. It is obvious that the experimental values lie significantly below the band gap of InAsSb strained on GaSb (dotted line). Note that for the 27% Sb sample the detected transition energy of 122 meV is lower than the minimum band gap of the bulk InAsSb alloy ($x_{Sb} \approx 60\%$). This cannot be due to an atomic ordering induced reduction of the band gap,

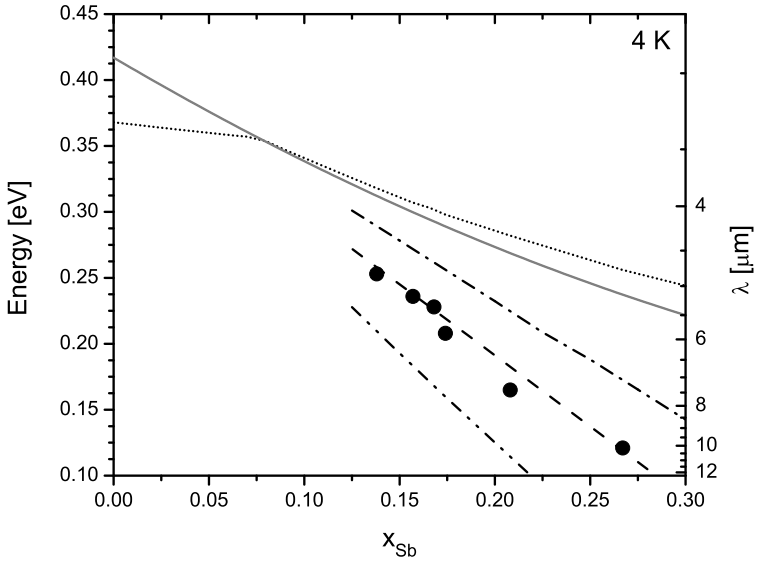

Figure 5.5: The PL peak energies measured at 4 K are plotted as a function of Sb content in the InAsSb QWs. Also included are the calculated energy-gap of unstrained InAsSb (solid line) and strained on GaSb (dotted line). Further included is the predicted type IIb transition (dashed line). A good agreement with the measured data can be achieved when assuming that 30% of the bandgap bowing in InAsSb occurs in the conduction band, and 70% in the valence band. The type II transition energies are calculated with nextnano[3]. Strain, temperature effects on band gap and lattice parameters, as well as quantization effects within the effective mass theory are included. Also included are the type II transitions for the cases where the band gap bowing is 100% in the conduction band (dash-dotted line) and 100% in the valence band (dash-dot-dotted line) as originally calculated directly with the solid model theory (Sec 5.2).

as ordering in InAsSb is only observed to be significant for Sb mole fractions on the order of 50% [54]. Also, the maximum reported bandgap reduction due to ordering in this material for highly ordered samples is typically 40 meV [54, 55], while the difference between the calculated curve and the measured sample is ≥ 80 meV for $x_{Sb} \geq 0.174$. As the transition energies are roughly linearly dependent on Sb fraction and do not follow the strained band gap, this behaviour cannot origin from impurity-to-band transitions. According to the trend in Fig. 5.5, the PL emission should reach 0 eV at an Sb mole fraction of ≈0.37. The most plausible explanation for these PL results is to assume a type II band alignment. This also agrees with the trend of reduced intensity with increasing Sb in the QWs (see Fig 5.4); as the band edge offset between the InAs and InAsSb increases, the overlap of electrons in the InAsSb and holes in the InAs decreases and thus the PL signal decreases. Tang et al. also observed similar very long wavelength emission from InAs/InAsSb superlattice light emitting diode structures grown on GaAs substrates [56]. The long emission wavelength was attributed to type IIa band alignment (electrons confined to InAsSb). In that work, the layers were obviously highly defective due to strain relaxation, making them unlikely to be suitable for use in photodetectors.

Figure 5.5 shows the results of our calculations of the transition energies for the present structures based on the method of Van de Walle for calculating band offsets [47]. How to incorporate the band bowing of this material system into this formalism is still discussed in literature. Some reports state that for low Sb mole fractions the bowing should occur only in the valence band (VB) with the conduction band (CB) varying linearly [57], while other authors expect only the conduction band to undergo bowing [47, 51, 58]. The predicted band alignment in any of those references is type IIb (see Fig. 5.2). In Fig. 5.5 those two extreme cases were directly calculated with the van de Walle formalism (see Sec 5.2): the case for the bowing of the conduction band is shown as dash-dotted line and in the case of the bowing is assumed to be only in the valence band is plotted as dash-dot-dotted line. The dashed line in Fig. 5.5 was computed with nextnano^3 assuming that 30% of the bowing occured in the conduction band and 70% in the valence band. This assumption agrees well with the measured data. Also Huang et al. [9] have assumed more of the bowing to occur in the valence band (45% CB, 55% VB) to achieve agreement between optical absorption edge data at 77 K and determination of the transition energy with optical ellipsometry measurements at room temperature for InAs/InAsSb superlattice structures on

a GaSb substrate with a period of ≈10 nm for Sb fractions of 0.25 and 0.4 in the InAsSb layers. Liu et al. [59] compared a series of InAsSb/InAs MQWs on InAs substrates (0.06< x_{Sb} <0.16) and also found the bowing to be predominantly in the valence band (40% CB, 60% VB). The theoretical curves also include small corrections due to the electron and heavy-hole quantum confinement energies. However, the exciton binding energy was not included in the simulation. It can be described as an effective Rydberg ($Ry^{\star}$):

$$Ry^{\star} = \frac{m_{red}}{m_0}\frac{1}{\epsilon_r^2}Ry \tag{5.25}$$

where m_{red} is the reduced mass ($1/m_{red} = 1/m_e + 1/m_{hh}$), ϵ_r is the relative permeability of the semiconductor and $Ry = 13.6$ eV is the Rydberg energy of hydrogen, which leads to an exciton binding energy of 1.4 meV (0.7 meV) in InAs (InSb). Thus it is small correction and was neglected in the calculations.

Apart from the present work, there are few comparisons in the literature of InAsSb/InAs SLS type II measured and calculated transition energies. However there are several theoretical and experimental results for growth on InAs substrates. Despite the wide theoretical consensus for type IIb band alignment of InAsSb QWs in InAs [47, 51, 58], previous experimental works have argued for alternative alignments including type I [52] and type IIa [53] (the conduction band of InAs above the conduction band of InAsSb). Both claim electron confinement in the InAsSb, based on the measurement of PL energies as a function of well width, in conjunction with magnetophotoluminescence measurements. Kurtz et al. [52] interpret their results in terms of a type I band alignment, however they did not explain the significantly lowered bandgap energy, while Tang et al. [53] argued for a type IIa band alignment. It is not possible to conclusively distinguish between the two type II cases from the data presented in this section nor from the work of Huang et al. [9], thus more direct measurements of the band offsets are required. It should be pointed out that type IIa alignment is not consistent with the fact that the electron affinity of InSb is accepted to be ≈ 300 meV less than InAs [60]. This open question will be addressed again in Sec 5.3.2, where the quantization energy as a function of quantum well width is considered (see Fig. 5.9) and found to be in accordance with our claim of type IIb behaviour.

sample	x_{Sb} (%)	type	t_{InAsSb} (nm)	t_{InAs} (nm)
1	4	SQW	20	104
2	6	SQW	21	103
3	8	SQW	21	105
4	10	SQW	21	108
5	12	SQW	21	107
6	3	MQW	21	21
7	6	MQW	21	21
8	7.5	SQW	61	199
9	7.5 (5.5)	DQW	16, 5	52, 102
10	7.5	DQW	31, 10	52, 102

Table 5.3: Summary of the PL samples grown on InAs substrates. Thicknesses and compositions were measured by HR-XRD.

5.3.2 Photoluminescence of QW Samples Grown on InAs Substrates

InAsSb can easily be grown on InAs substrates and some challenges, like the GaSb-InAs(Sb) interface, are avoided. Due to the lattice mismatch, only thin films or layers with very low Sb content can be grown before relaxation occurs. The calculated critical thickness of InAsSb on InAs is plotted in Fig 3.10. A superlattice consisting of InAsSb and InAs layers cannot be strain balanced; however, structures with only a few periods for PL measurements can be grown without strain relaxation. In this work a series of InAsSb single quantum wells (SQWs) were studied to measure the PL transition energy as a function of Sb content and quantum well width in order to provide another check of the modelling results.

The samples, listed in Table 5.3, were grown on InAs (100) exact substrates under standard growth conditions. The SQW samples consist of a 20 nm InAsSb layer sandwiched between a 100 nm layer of InAs on either side, while the MQW samples consist of 6 periods of a 20 nm InAsSb and a 20 nm InAs layer grown on an InAs buffer. The double quantum well (DQW) samples consist of a buffer, the first QW, 50 nm barrier, the second QW and a 100 nm cap. The Sb content as well as layer thicknesses were measured and it

was determined that none of the layers showed strain relaxation.

Figure 5.6(a) shows the 004 x-ray rocking curves of the single quantum well samples (1-5) with increasing Sb content in the well. The strong pendellosung fringes are a sign of good structural layer quality and sharp growth interfaces. Figure 5.6(a) shows the 004 x-ray rocking curve of the MQW sample 6. This is compared to a simulated xrd curve which was offset for clarity. The measured fringes are hardly broadened compared to the simulation and all pendellosung fringes are clearly visible over a wide diffraction angle range, which indicates good layer quality and very little Sb segregation into the InAs wells.

Fig 5.7 shows 4 K PL spectra for InAs/InAsSb QW and MQW samples with various Sb compositions. The energy position of the peak is strongly dependent on the Sb content and the intensity decreases with increasing Sb mole fraction due to the reduced overlap of the wavefunctions of electrons in the InAs layers and the heavy holes in the InAsSb layers of the spatially indirect transition. Fig 5.8 shows a comparison between the PL peak energies as a function of Sb content and the calculated transition energies. The theoretical prediction using the parameters found in Sec 5.3.1 is in good agreement with the measured data. Thus a single set of parameters, listed in Table 1, can be used to describe the type II transition energy for Sb compositions between 3% and 27%, on two different substrates, InAs and GaSb.

Also a PL study of the confinement energy as a function of InAsSb well width was conducted in order to distinguish between a type IIa and type IIb band alignment (see inset Fig 5.9). The PL transition energy was compared to the nextnano^3 transition energy simulation for two cases: the type IIb case, expected from theory [47, 51, 58] as well as consideration of the electron affinities of InAs and InSb [60], and a type IIa alignment as suggested by experimental work by Tang et al. [53]. For the type IIa case, the parameter of the vacuum energy level of InAs was overridden, so that the calculated transition energies agree with Fig 5.8. As the confinement energy scales with the inverse effective mass ($1/m^\star$), the case of the type IIa alignment, where the electrons are confined, has a significantly higher energy dependence on the well width compared to the type IIb case, where the (heavy) holes are in the well. The observation that the change in energy for QW widths >10 nm is insignificant, strongly supports the expected type IIb transition and is in good agreement with the simulation.

The measured PL energy of the 5 nm QW cannot be simulated by any parameter set

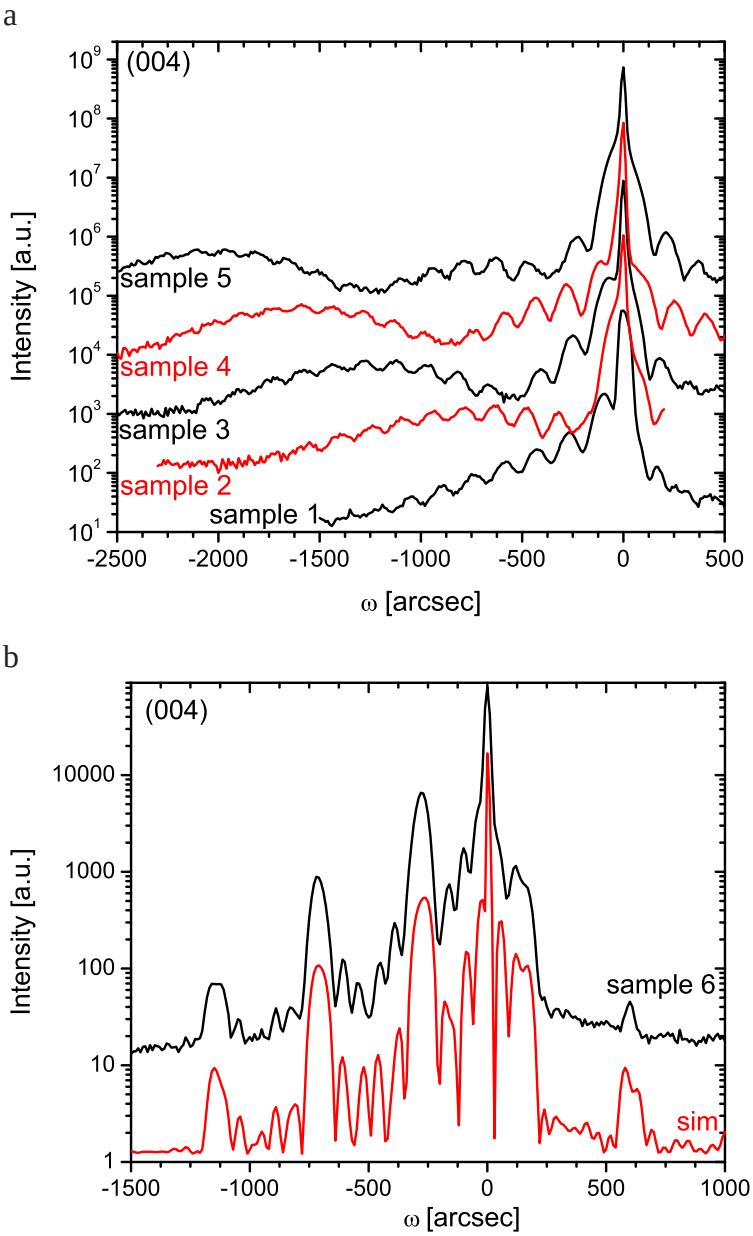

Figure 5.6: HR-XRD spectra of the 004 reflection. (a) Measured data of the SQW samples 1-5. The scans are offset for clarity. (b) Comparison between measured data of the MQW sample 6 and a simulation.

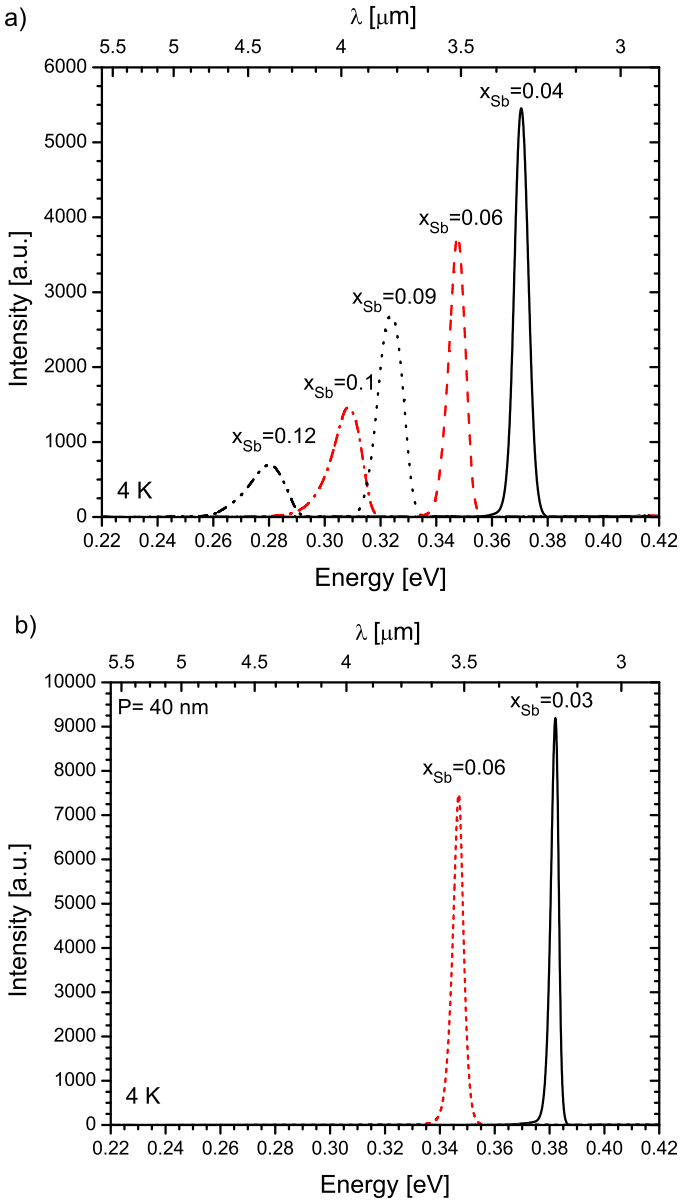

Figure 5.7: The PL spectra recorded at 4 K of the InAsSb QW samples grown on InAs substrates are plotted as a function of energy and labeled by the Sb content in the QWs. a) Spectra of samples 1–5 consisting of one SQW with a width of 20 nm embedded in InAs. b) 6 period SL structures with InAs and InAsSb layer thickness of 20 nm (samples 6&7).

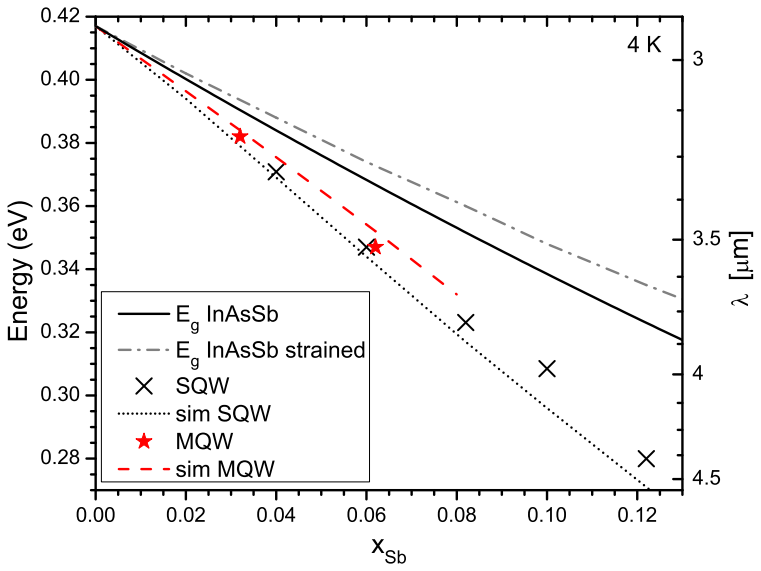

Figure 5.8: The PL energies of InAsSb layers grown on InAs recorded at 4 K are plotted as a function of Sb content in the QWs. × (★) denotes the SQW (MQW) samples, respectively. The InAsSb unstrained bandgap is displayed as a solid line. The dash-dotted line shows the bandgap of InAsSb strained on the InAs substrate. The dotted (dashed) line is the result of the type IIa transition energy simulation for the case of the SQW (MQW) samples.

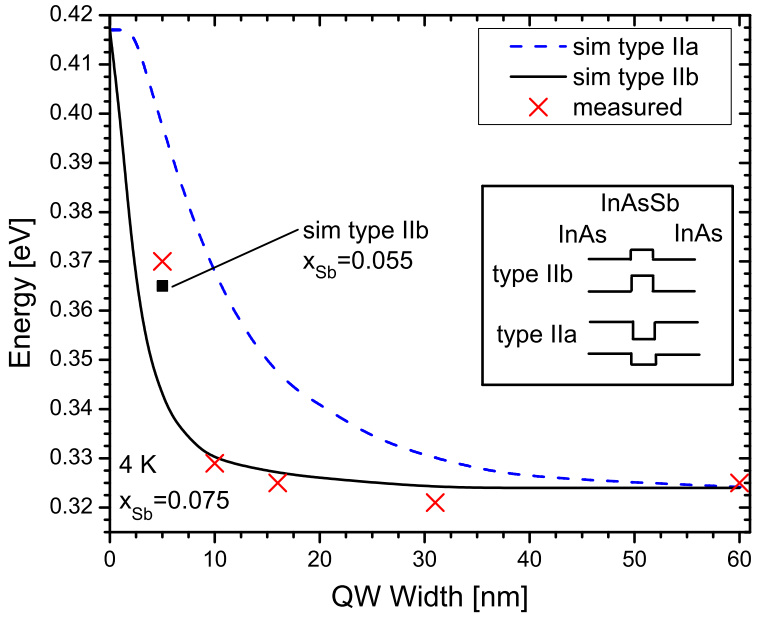

Figure 5.9: PL energy as a function of $InAs_{0.925}Sb_{0.075}$ QW width on InAs substrates compared with simulation. The solid (dashed) line is computed with a type IIb (IIa) alignment where the heavy holes (electrons) are confined in the well. The data strongly suggests the type IIb alignment. Note that for the smallest QW, the composition seems to have changed to x_{Sb}=0.055 instead of the intended value of x_{Sb}=0.075. The fact that for a QW width <10 nm, there is very little change in confinement strongly suggests the type IIb alignment. The inset depicts a sketch of the two different band alignment cases considered.

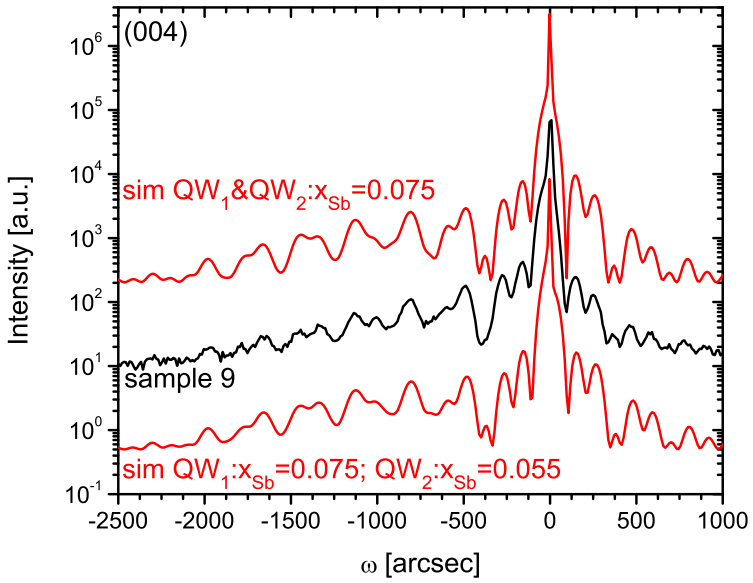

Figure 5.10: HR-XRD (004) measurement of sample 9 (Table 5.3) compared to two simulations; top: assuming both InAsSb QWs (16 nm, 5 nm) have a Sb content of 0.075. Bottom: different compositions where the Sb content of the 5 nm QW is changed to 0.055. Unfortunately the XRD measurement is not very sensitive to a small composition change in a single quantum well of this width, however the bottom simulation does appear to be closer to the measured data. The spectra are offset for clarity.

that is in good agreement with the data points between 10 nm and 60 nm QW-width when assuming the same composition. Thus it is concluded that the composition must have changed to x_{Sb}=0.055 for the 5 nm sample. In that case it is in agreement with the model. Unfortunately the HR-XRD is not sensitive to a small composition change in a thin QW. The HR-XRD measurement of the DQW sample 9 (5 nm & 16 nm) is shown in Fig. 5.10 in comparison with two simulation assumptions: constant composition for both QWs (top) and different compositions (bottom). The composition shift has very little effect on the spectra, however the simulation on the bottom does give a slightly better fit which is in agreement with the above assumption.

Chapter 6

Detector Results

In this chapter, the measured results of the fabricated optical devices will be presented. As a first step in developing the detector, results of a p-n junction InAsSb detector lattice matched to GaSb will be discussed. Then it will be shown how a InAsSb/InPSb heterojunction detector lattice matched to GaSb, can overcome limitations and improve the performance of the simpler homojunction devices. Simulation results regarding the lowest optical transition energies and the optical matrix elements of the transitions of the superlattices as a function of period and Sb composition in the InAsSb layers will be presented as a design guide for future work. The optical matrix elements of type II InAsSb/InAs superlattices are compared to short period InAs/(In)GaSb superlattices and found to be greater or equal. Finally, initial results of a detector with a superlattice absorber will be shown and the cutoff energy of 150 meV (8.5 μm) is found to be in accordance with the simulations.

6.1 Bulk Detectors

InAsSb absorber layers lattice matched to GaSb absorber layers can be an alternative to HgCdTe detectors for the 3-5 μm wavelength regime [61–63]. The focus of this work is on the strain-balanced InAsSb/InAs superlattice detectors. Bulk InAsSb detectors were grown, processed and measured as a development step, for test and optimization purposes for the more complex structures where the lattice matched absorber is replaced with a strain balanced superlattice structure. It has been shown that the performance of InAsSb detectors, especially at higher temperatures, can be improved by wider bandgap barrier

layers [62, 63]. The barrier layer reduces the thermal diffusion currents. Wider band gap layers lattice matched to GaSb can typically be grown by alloying Al or P to form ternary or quaternary layers [62–64]. In this work the use of ternary $InP_{0.63}Sb_{0.37}$ was explored, which is lattice matched to GaSb and has a bandgap at room temperature of 0.46 eV [4]. The bandgap of $InP_{0.63}Sb_{0.37}$ is significantly larger than the bandgap of $InAs_{0.91}Sb_{0.09}$ which is only 0.27 eV [4] at room temperature.

6.1.1 InPSb Growth and Device Fabrication

The homojunction and heterojunction devices were grown at $500^{\circ}\mathrm{C}$ on GaSb:Te (100) miscut 2° towards (111)B wafers which were deoxidized by immersion in HCl before growth. The n-type InAsSb layer was non-intentionally doped, while the p-type top layer was doped with Zn from a DEZn source. InAsSb was grown at a V:III ratio of six.

It took special effort to grow $InP_{0.63}Sb_{0.37}$. A strong preferential incorporation of Sb was found; an Sb content of 0.37 only required a mole fraction of $[\mathrm{Sb}]/([\mathrm{P}]+[\mathrm{Sb}])$ in the vapor phase of 0.13. Also a V:III ratio of ≥ 60 was needed to achieve a specular surface morphology. As the TBP flow was limited by the mass flow controller, the carrier flow had to be reduced to 1 SLM from 6 SLM during the InAsSb growth in order to keep such a high group V partial pressure.

The heterojunction and homojunction samples were processed in New Mexico as follows. By photolithography, mesas were defined with a dry etch technology using a inductively coupled plasma (ICP) of BCl_3 gas. Both evaporated metal contacts were made of Ti/Pt/Au (50 nm/50 nm/300 nm). No passivation was applied to the sidewalls. A device schematic is displayed in Fig 6.1

In 4D-Labs at SFU, mesas were defined by photolithography. The homojunction device was etched by citric acid:hydrogen peroxide = 2:1. The etching rate of InAsSb was 40 nm/min. Metal contacts were thermally evaporated with both contacts on the top-side of the sample made of Cr/Au (100 nm/100 nm) as shown in Fig 6.1. For the InPSb devices, a two step wet etching process was employed. The InPSb top-layer was etched by phosphoric acid:H_2O_2:H_2O = 1:1:8, while all other processing steps were the same as for the homojunction device.

In summary, there are electrical data (I-V) from both types of devices fabricated in SFU

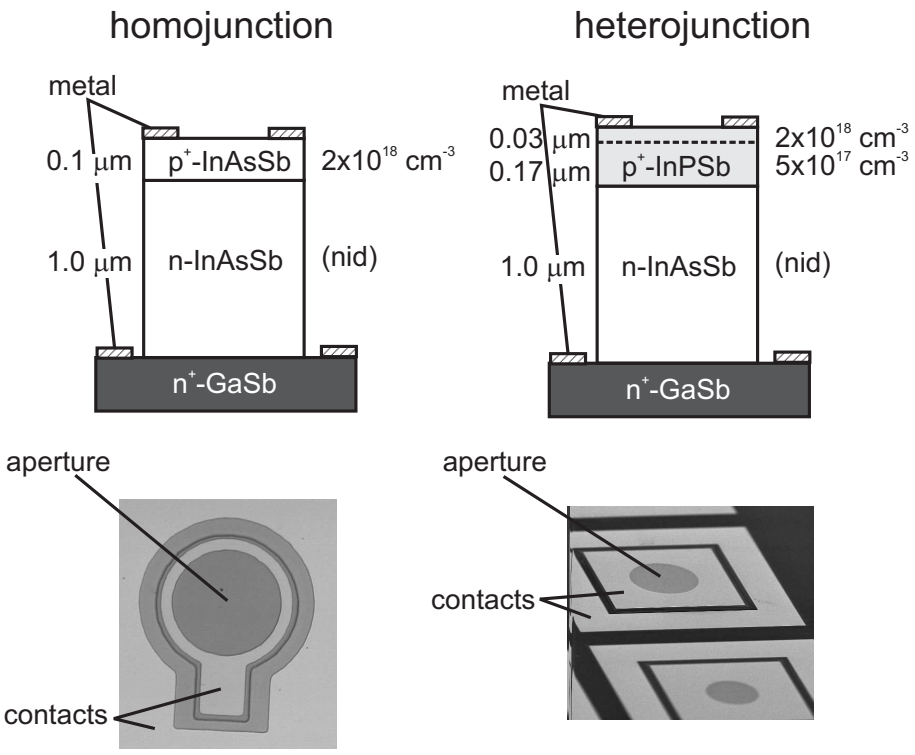

Figure 6.1: Schematic of a homojunction and heterojunction bulk detector after processing. The 1 μm thick InAsSb absorber layer is non-intentionally doped (nid) which results in low n-type doping. The same ohmic metal contacts were used for the GaSb bottom and the InPSb or InAsSb respectively top contact. The metal contacts were connected by wire-bonding. Variable mesa sizes were fabricated for variable array diode analysis (VADA); these samples did not have an opening (aperture) in the top contact. The devices for optical measurements had a circular opening in the top contact (aperture) with a varying diameter for optical excitation. Below are microscope images of a processed device at SFU (homojunction) and New Mexico (heterojunction).

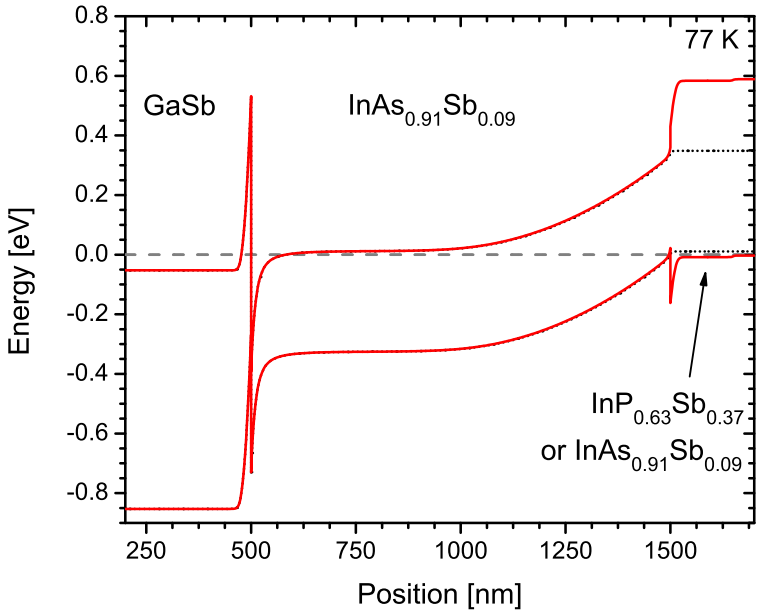

Figure 6.2: Simulation of the band structure at 77 K of a homojunction and a heterojunction device lattice matched to GaSb. An n-InAsSb/p-InPSb heterojunction (solid line) compared to an InAsSb homojunction (dotted line) device. The dashed line is the Fermi level. All layers are lattice matched to the GaSb substrate. The doping levels of the simulations are n=1×10^{18} cm^{-3} (GaSb), n=2×10^{15} cm^{-3} (InAsSb) and p=5×10^{17} cm^{-3} (InPSb) or p:1×10^{18} cm^{-3} (InAsSb) for the homojunction.

and New Mexico. However, optical response data is only available for a SFU fabricated homojunction sample and for a heterojunction device fabricated in New Mexico.

6.1.2 Electrical Characterization

An energy band diagram of both the homojunction and heterojunction devices is shown in Fig 6.2. The simulation was done with nextnano^3 [45]. The simulation clearly shows how the wider band gap forms a diffusion barrier for electrons. A big advantage of the heterojunction design is the fact that InPSb does not have a surface accumulation layer as will be discussed below.

Fig 6.3 shows the I-V characteristics of typical bulk devices for a device area of

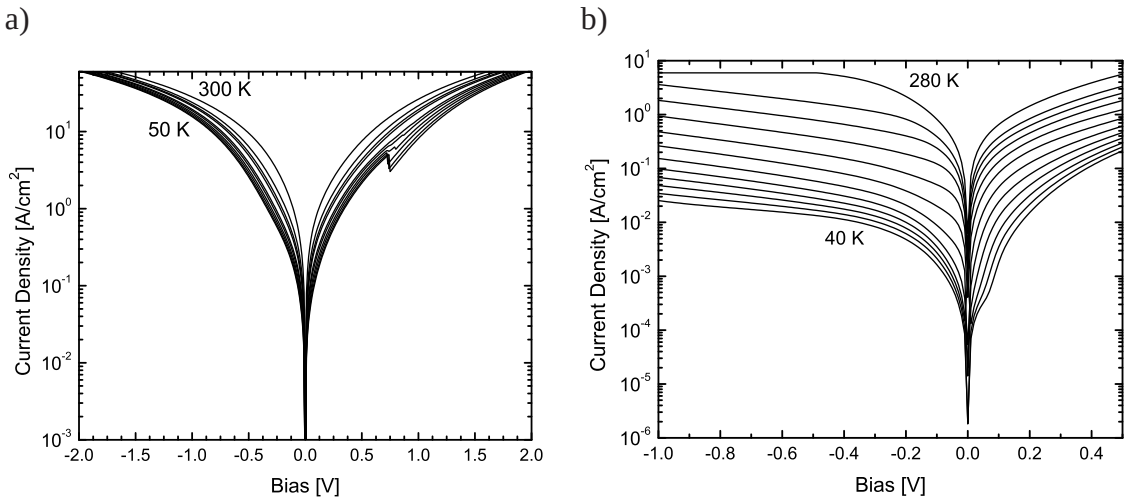

Figure 6.3: Dark current as a function of bias voltage at different temperatures for a device area of 400 μm$\times$400 μm. a) Homojunction device at temperatures from 50 K to 300 K in 25 K steps. b) Heterojunction device at temperatures from 40 K to 280 K in 20 K steps. The data was taken at the University of New Mexico.

	R_0A [Ωcm^2]			
	homojunction		heterojunction	
Temperature	UNM	SFU	UNM	SFU
77 K	0.7	0.6	65	17
300 K	0.12	0.1	0.2	0.6

Table 6.1: Resistance area product at 0 V bias (R_0A) of the hetero- and homojunction detectors for devices fabricated at SFU and the University of New Mexico (UNM) . The values were measured for devices with an area of 0.16 mm^2 (UNM) and 1 mm^2 (SFU).

0.16 mm^2. The homojunction shows hardly any rectifying behaviour at all temperatures. The heterojunction design improves the performance significantly and the device is clearly rectifying. As a figure of merit, the area-resistance product (R_0A) was measured. R_0A is defined as:

$$R_0A = \left(\frac{\mathrm{d}j}{\mathrm{d}V}\right)^{-1}_{|V=0} \tag{6.1}$$

where j is the current density and V the applied voltage. For photodiodes, R_0A is related to the detectivity (D^*) by [65]

$$D^* = \frac{\eta\lambda q}{2hc}\sqrt{\frac{R_0A}{kT}} \tag{6.2}$$

where η is the quantum efficiency, λ is the wavelength, h is Planck's constant, c is the speed of light, q is the elementary charge, k is Boltzmann's constant and T is the temperature.

At 77 K, R_0A is larger by a factor of ≈100 (see Table 6.1). The likely reason for this enormous improvement is that InAsSb forms an electron accumulation layer at the surface due to Fermi-level pinning [37, 66]. This electron accumulation layer, which is present for n- and p-type InAsSb, forms a surface leakage path that shunts the p-n junction of the homojunction device. The InPSb however has a higher conduction band compared to InAsSb (see Fig 6.2) and does not suffer from an electron gas at the surface. Here, surface states are inside the gap resulting in a surface depletion rather than accumulation as is the case for narrow gap InAsSb. Thus the shunt channel is blocked. This assumption is supported by the variable diode area analysis (VADA) results displayed in Fig 6.4. The dark current density under a negative bias of -0.1 V was measured on diodes with different areas. The dark current density is plotted as a function of perimeter divided by area (P/A). The measurement was conducted at a sample temperature of 77 K. The large positive slope of the homojunction sample is due to the surface leakage current. By switching to the heterojunction design, this leakage path across the junction is blocked, as indicated by the flat VADA curve. Another way to improve the homojunction devices would be sidewall passivation. Shafir et al. [67] report an argon plasma treatment in combination with a tartaric acid etch which resulted in a leakage current decrease of 5 orders of magnitude. So far this has not been investigated for the present material.

The 77 K values of R_0A for the heterojunction device are smaller than the highest value of ≈400 Ωcm^2 reported by Shao et al. [68] for a MBE grown p$^+$-i-n$^+$ $InAs_{0.91}Sb_{0.09}$ diode on a GaSb wafer with a p-$In_{0.88}Al_{0.12}As_{0.80}Sb_{0.20}$ barrier layer. Both electrical contacts

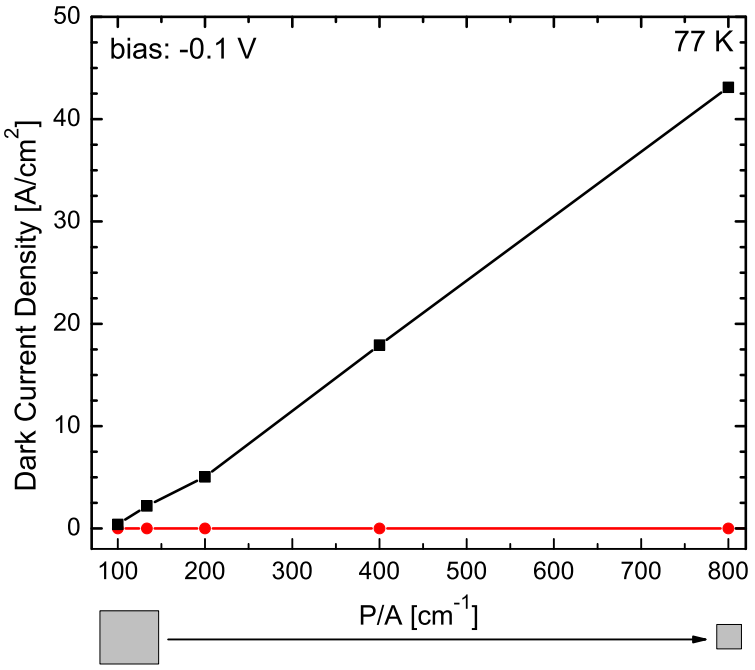

Figure 6.4: VADA analysis of a homojunction (■) and heterojunction (●) detector at 77 K. The dark current density is plotted versus the perimeter to area ratio. The size of the square mesa devices range from 50 μm to 400 μm . The homojunction devices suffer from severe surface leakage which shunts the pn-junction. This is eliminated by the heterojunction design.

were made to InAsSb. The non-intentionally doped absorber thickness was 2 μm. Other authors report R_0A values of ≈10 Ωcm^2 for different MBE grown InAsSb heterojunction diode designs on GaSb at 77 K [62, 69]. A much larger value of $R_0A = 10^9\Omega$cm^2 at 77 K however was reported by Bubulac et al. [61] in 1980 for InAsSb homojunction device grown by liquid phase epitaxy lattice matched to a GaSb substrate. The layer thickness was 10 μm. It is unclear, why this homojunction device does not seem to suffer from surface leakage as no surface passivation treatment was applied. It can only be speculated why such a high R_0A value was achieved as neither the chemicals used for the etching, nor the GaSb substrate doping level are specified in the paper.

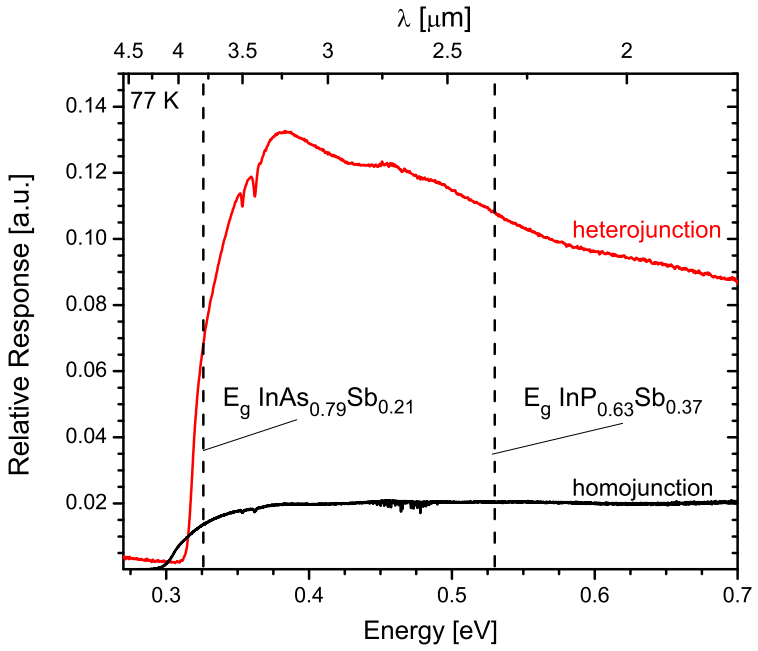

Figure 6.5: Optical response of an InAsSb/InPSb heterojunction detector grown on GaSb at 77 K in comparison with a comparable InAsSb homojunction design. The heterojunction detector was fabricated in New Mexico, while the homojunction detector was processed at 4D-labs at SFU. The diameter of the circular aperture of the homojunction device was 300 μm while the aperture diameter of the heterojunction sample was 100 μm. The heterojunction design shows a significant performance improvement compared to the simpler homojunction design.

6.1.3 Optical Response of Bulk Detectors

In order to measure the optical response of the detectors, the devices were glued onto a chip carrier with silver paint and the device contacts were wirebonded to the pins on the chip carrier. The carrier was mounted on the cold finger of a dewar with a CaF_2 window in the case of the bulk samples and a ZnSe window for the superlattice detector. The sample was cooled to liquid nitrogen temperature and placed on the detector port of a Bomem DA8 FTIR spectrometer. A globar was used as the infrared light source.

Fig 6.5 shows the comparison of the optical response of a heterojunction and a homo-

junction diode. The recorded raw spectrum was divided by a fit to the system response which was measured with a MCT photoconductive detector. The difference in cut-off energy is due to the slightly different Sb composition in the absorber layer. The measurements were taken on different days, which explains why the water vapor lines around 460 meV were not present in the heterojunction response. The steeper turn on and higher signal intensity of the heterojunction device is significant. This improved performance is due to suppression of the shunt path around the diode. Assuming that the signal scales with the aperture area, the heterojunction design leads to an improvement of signal intensity by a factor of 6 which is comparable to a commercially available InAs "J12" diode by Judson. The increased signal intensity shows an improvement in η. At the same time the R_0A value of the heterojunction device, which is related to the noise current, is improved up to a factor of $\approx$100 at 77 K compared to the homojunction design (see Table 6.1). Thus the detectivity of the heterojunction design is expected to be improved by more than an order of magnitude (see Eq 6.2). Unfortunately actual detectivities could not be measured, as the measurement set-up was not calibrated. Further it is noticed that the heterojunction signal starts to drop for energies above the InPSb band-gap, while the signal from the homojunction device is constant in this energy region. This could be an indication, that some carriers absorbed in this material are not extracted. This shows that either the doping was too high, or more likely that quality of the material was too low. The heterojunction detector was taken from a corner of a wafer where due to the poor composition uniformity of InPSb, a crosshatch pattern was visible under the optical microscope. These defects that relieve strain can act as carrier recombination centres. Overall, the heterojunction design shows a great improvement compared to the simpler homojunction which should especially increase the performance at higher temperatures.

6.2 Strained Layer Superlattice Detector

6.2.1 Strained Layer Superlattice Modelling

As seen from the PL results in Sec 5.3, the lowest optical transition energy is strongly dependent on the Sb composition in the InAsSb layers. Since the electrons in the conduction band are confined in the InAs layer, while the heavy holes are confined to the InAsSb layer,

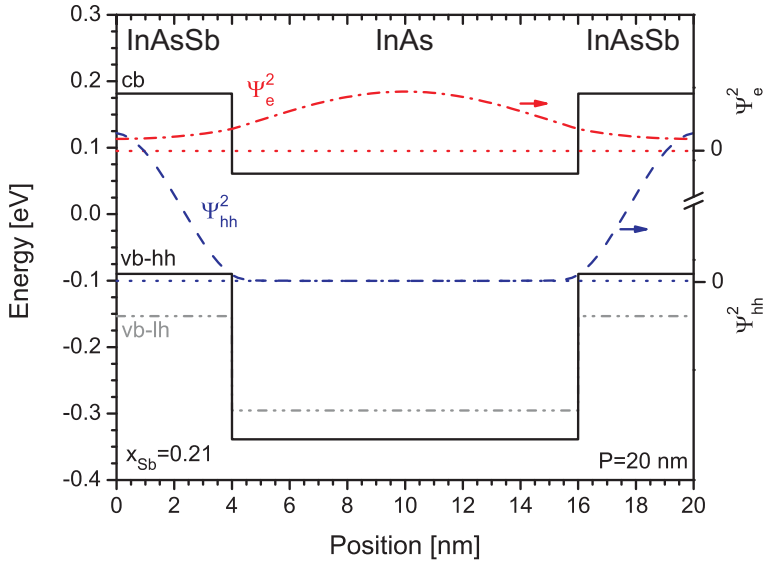

Figure 6.6: Band structure simulation of one period of an InAs/InAsSb superlattice with a 20 nm period at 77 K with periodic boundary conditions. The Sb composition in the InAsSb layers is 0.21. This structure is strain balanced on a GaSb substrate. The dotted lines are the 1^{st} quantized energy levels of the electron confined in the InAs layer and the heavy hole in InAsSb. Ψ_e^2 (Ψ_{hh}^2) is the probability distribution function of the electron (heavy hole).

the transition occurs only where the probability distribution functions overlap (see Fig 6.6). Thus the likelihood of such a transition depends on the wave function overlap. The overlap can be increased by shortening the period of the superlattice, as shown in Fig 6.7, which also results in an increase of transition energy.

In order to predict the transition energy and, as a figure of merit, the optical matrix element for a strain balanced superlattice of a specific Sb composition and period, a number of 77 K simulations were conducted with nextnano[3]. The same parameters (see Table 1) that successfully predicted the PL transitions at 4 K (see Sec 5.3) were used and the carriers were again treated within the effective mass framework.

Fig 6.8a shows the lowest transition energy (cb-hh) as a function of Sb composition in the InAsSb layers for a SL period between 40 nm and 5 nm. Note that all calculated SL structures are strain balanced on GaSb, and thus the InAsSb layer thickness (t_{InAsSb}) as

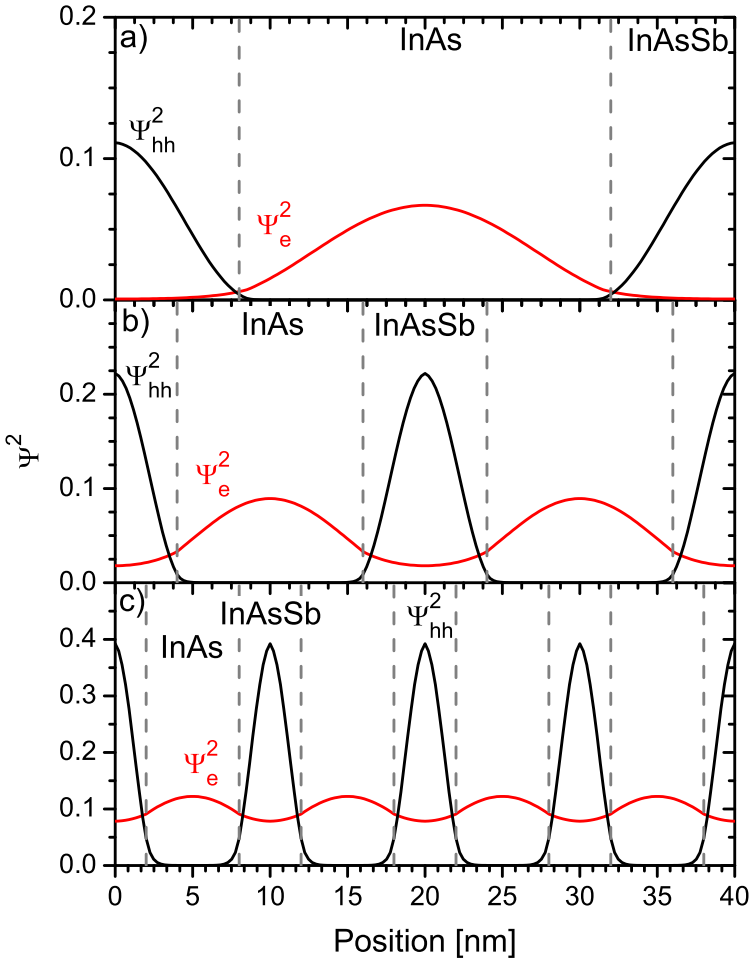

Figure 6.7: Probability distributions for electrons and heavy holes in InAsSb/InAs SLS structures at 77 K for an Sb content of 0.21 and a period of 40 nm (a), 20 nm (b), and 10 nm (c). Periodic boundary conditions were chosen to simulate the SL. The probability distribution functions are normalized over one period. With decreasing period, the wavefunction overlap strongly increases. While electrons (holes) are confined in the InAs (InAsSb), only the electron wavefunction penetrates significantly into the barrier.

a function of the Sb composition (x_{Sb}) and SL period (P) can be calculated according to Eqn 5.2:

$$t_{InAsSb} = 0.090 \left(\frac{P}{x_{Sb}} \right) \tag{6.3}$$

With increasing Sb composition or longer periods, in order to reach further into the infrared region, the carrier overlap decreases and thus the transition probability is also reduced. The transition probability is proportional to the square of the optical matrix element per period (M_p). This is used as a figure of merit here and for comparison to the (In)GaSb/InAs short period SL system. The optical matrix element (M) can be expressed as:

$$M = \int \Psi_e^{\star}(\mathbf{r})(\boldsymbol{\epsilon} \cdot \hat{\boldsymbol{p}})\Psi_{hh}(\mathbf{r})\mathrm{d}^3\mathbf{r} \tag{6.4}$$

where $\boldsymbol{\epsilon}$ is the unit vector of polarization and $\hat{\boldsymbol{p}}$ is the momentum operator.

According to Weisbuch and Winter [70] the electron and hole wave functions can be expressed as Bloch states with the standard Bloch function ($U_{c\mathbf{k}_e}$) multiplied by an envelope function $F(z)$ for the particle in the well:

$$\Psi_e = F_e(z)U_{c\mathbf{k}_e} \tag{6.5}$$

Within the so called envelope-function approximation the matrix element of one period is then approximated by [71]:

$$M_p \approx \langle cb|p|hh\rangle_{bulk} \int_{-P/2}^{P/2} F_{hh}^{\star}(z)F_e(z)dz \tag{6.6}$$

where $\langle cb|p|hh\rangle_{bulk}$ is the bulk optical matrix element. Since the heavy holes are very well contained in the InAsSb wells and it is only the electron wave function that considerably spills into the barriers (see Fig 6.7), only the bulk optical matrix element of InAsSb was chosen for the approximation in equation 6.6. It was linearly interpolated from the values of InAs and InSb reported in Vurgaftman et al. [4] which are displayed in Table 6.2.

The results of the simulations are presented in Fig 6.8. Part a shows the predicted transition energy for a temperature of 77 K as a function of Sb composition for different periods. With decreasing period more Sb is needed in the InAsSb layers to achieve a certain cutoff wavelength. For a period of 5 nm, the lowest transition energy that can be reached for an Sb composition <50% is 0.21 eV (6 μm), for a 7 nm period 0.12 eV (10 μm) and for 10 nm period <0.6 eV (>20 μm).

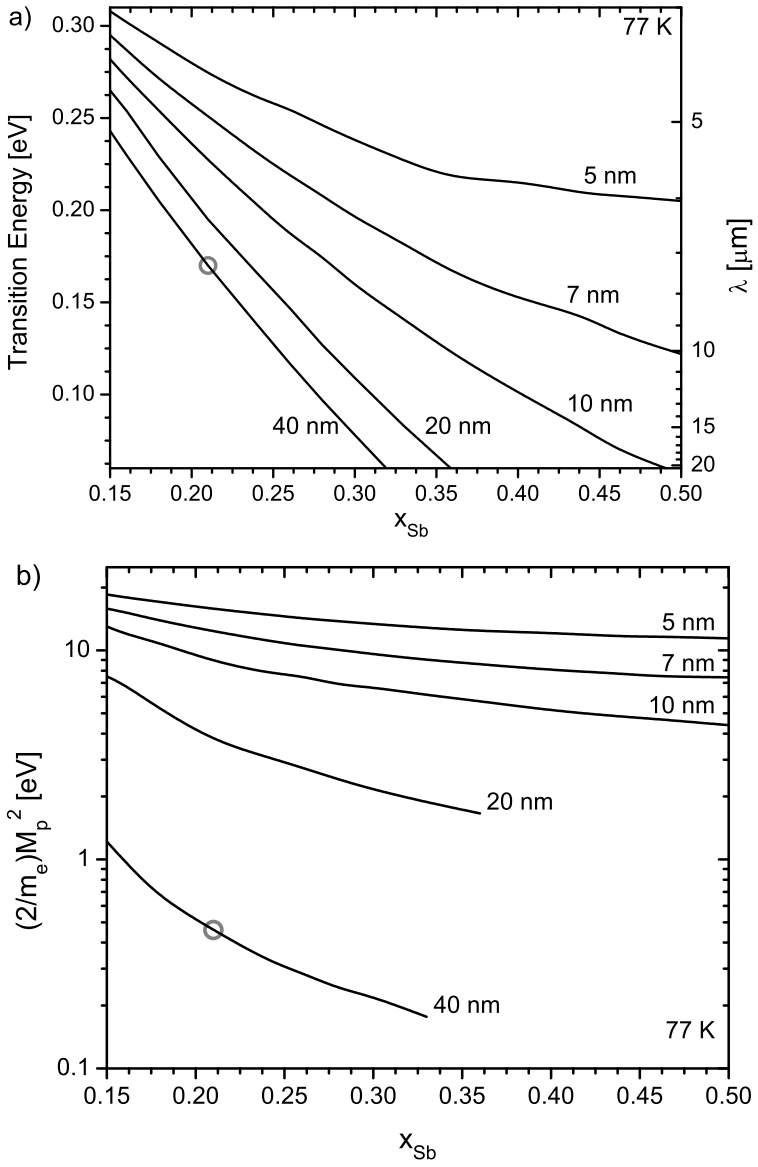

Figure 6.8: Simulation results for InAsSb/InAs strain balanced SL structures on GaSb at 77 K. a) Expected transition energy as a function of Sb composition in InAsSb for different SL periods. b) Calculated optical matrix elements squared for one period as a function of Sb composition in InAsSb for different SL periods. m_e denotes the mass of an electron. The circle marks the position of the superlattice detector discussed in section 6.2.2 in this graph.

bulk	$(2/m_e)\langle cb\|p\|hh\rangle^2$
InAs	21.5 eV
InSb	23.3 eV
GaSb	27 eV

Table 6.2: Value of the squared bulk optical matrix elements according to [4]. Multiplication with the prefactor $2/m_e$ leads to units of eV.

The transition probability however is proportional to the optical matrix element squared, which is plotted in Fig 6.8 b. By decreasing the period from 40 nm, which is the period of the detector presented in section 6.2, to 20 nm, M_p^2 can be increased by a factor of 10. A further decrease of the period to 10 nm would lead to another factor of 5 in the expected detector signal. This explains the poor performance of the SL detector presented in this work and at the same time shows the potential for improvement.

The calculation of M_p^2 also makes it possible to compare the expected performance of InAsSb/InAs type II strain balanced superlattice detectors to the more common InAs/(In)GaSb superlattice detectors grown on GaSb. The growth and control of InAs/GaSb or GaSb/InSb-ML/InAs interfaces and thin layers is extremely difficult when done by OMVPE [9] and thus is usually done by MBE. The simulations in Fig 6.9 do not include interface layers and are only for the case of equal layer thicknesses of InAs and (In)GaSb at 77 K grown on GaSb (001). In Fig 6.9a), the transition energy is plotted as a function of period for the case of InAs/GaSb, InAs/$In_{0.2}Ga_{0.8}Sb$ and InAs/$In_{0.4}Ga_{0.6}Sb$ superlattices. Part b) shows the squared optical matrix element per period as a function of the period. Again the optical matrix element was approximated by the overlap integral multiplied by the optical matrix element of bulk (In)GaSb.

As examples, two cutoff wavelengths (5 μm and 10 μm) were selected for comparison of their squared optical matrix elements as shown in Table 6.3. For the InAsSb system, the Sb content required in the InAsSb layers for different SL periods is also displayed; for the InAs/GaSb system, the SL period needed, assuming equal thickness layers of InAs and (In)GaSb is tabulated. The optical matrix elements of these two systems can now be compared. InAsSb/InAs can be designed with a higher optical matrix element and longer period for both wavelengths when compared to the more common InAs/GaSb approach.

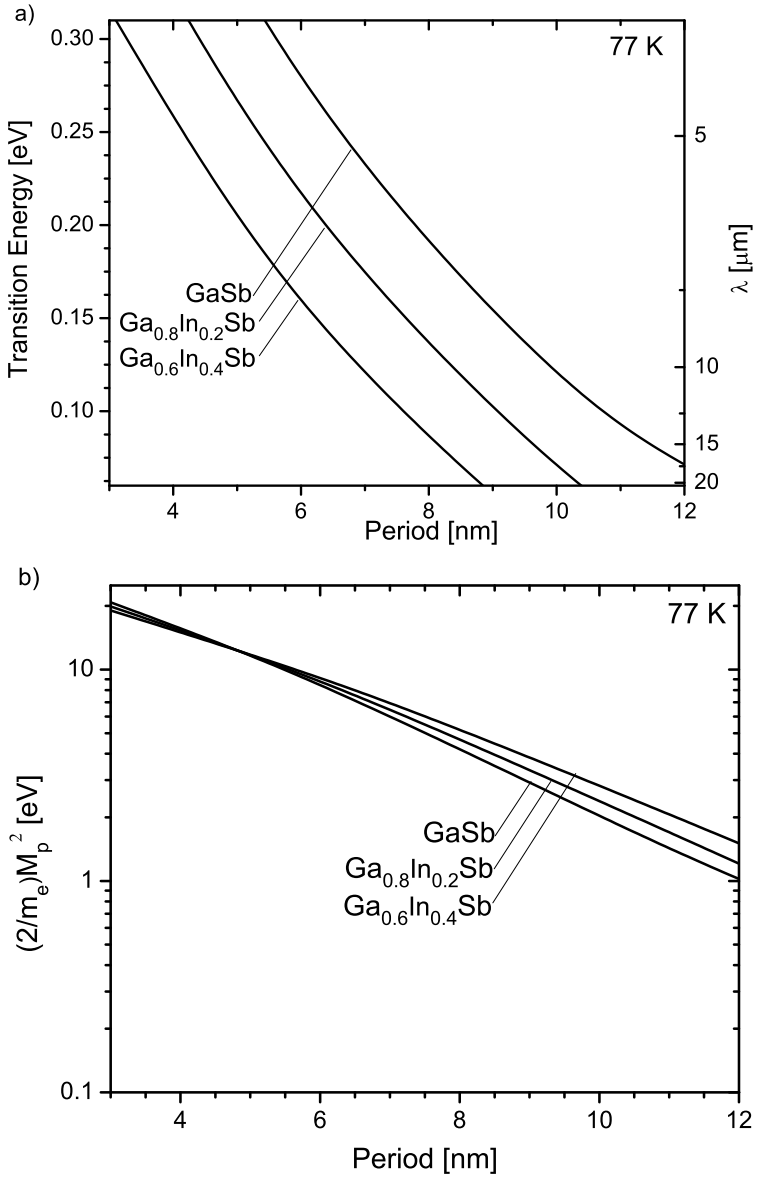

Figure 6.9: Calculated transition energy (a) and optical matrix element for one period (b) of InAs/(In)GaSb SL structures at 77 K as a function of period. InAs and (In)GaSb layers are of the same thickness.

	InAsSb/InAs					**InAs/(In)GaSb**			
		Period [nm]					x_{In} in InGaSb		
target λ		5	7	10	20		0	0.2	0.4
10 μm	x_{Sb}	–	0.49	0.35	0.28	Period [nm]	10.5	9	7.5
	$(2/m_e)M_p^2$ [eV]	–	7.5	5.9	2.3	$(2/m_e)M_p^2$ [eV]	1.7	3.3	6.1
5 μm	x_{Sb}	0.28	0.21	0.18	0.16	Period [nm]	6.7	5.4	4.2
	$(2/m_e)M_p^2$ [eV]	14	12.5	10.8	6.8	$(2/m_e)M_p^2$ [eV]	6.6	10.5	14

Table 6.3: Comparison of an InAsSb/InAs with an InAs/(In)GaSb SL for the case of a detector cutoff at 10 μm and 5 μm at an operating temperature at 77 K. Note that InAs/(In)GaSb superlattices discussed here are not strain balanced.

Also InAsSb/InAs can easily be grown strain balanced and thus it is easier to realize with the OMVPE growth technique. This makes InAsSb/InAs strain balanced SL-structures a promising approach for infrared detection in the wavelength range between 5 μm and 20 μm based on III-V technology.

6.2.2 Optical Response of a SL detector

A strain-balanced SL device sample was grown on a GaSb:Te (100) substrate miscut 2° towards (111)B, with a V-III ratio of 6 and a growth rate of 3 Å/s at 500 °C. A 50 nm $InAs_{0.91}Sb_{0.09}$ lattice matched buffer was grown on the GaSb wafer, followed by a 1 μm thick InAsSb/InAs strain balanced SL absorber with an Sb composition of 0.21 and a period of 40 nm. A 100 nm p-doped (Zn:2×10^{18} cm^{-3}) $InAs_{0.91}Sb_{0.09}$ top layer was then grown to form the p^+n junction, as the non-intentionally doped layers are n-type (typically 2×10^{15} cm^{-3}). The doping concentration of the GaSb substrate was n=1×10^{18} cm^{-3} which forms a tunnel junction with low n-doped InAsSb as shown in chapter 4. HR-XRD was employed to verify layer composition, thickness and strain state.

Device fabrication was achieved using optical photolithography to define 410 μm $\times$ 410 μm square mesa devices with apertures ranging from 20–300 μm. Etching was performed using an inductively coupled plasma (ICP) of BCl_3 gas. Ohmic contacts were evaporated on the bottom and top contact layers using Ti (500 Å)/Pt (500 Å)/Au (3000 Å) in both cases. The device was fabricated at the University of New Mexico. The lattice matched homojunction detector, plotted for comparison in Fig 6.10 was described in section 6.1.

A Bomem DA8 Fourier transform spectrometer was used for the optical response measurements of the detector samples. The InAsSb based detector sample was mounted on a leadless ceramic chip carrier attached to a coldfinger in a dewar with a ZnSe window, which was cooled to liquid nitrogen temperature. A globar was used as the IR source. A KBr beam splitter was used in the interferometer for the SL sample, while a CaF_2 beam splitter was employed for the measurement of the lattice matched device. No bias was applied to the photodiodes.

Figure 6.10 shows the uncalibrated optical response of the strain balanced SL detector (black) and a comparable lattice matched structure (gray). The spectra were normalized

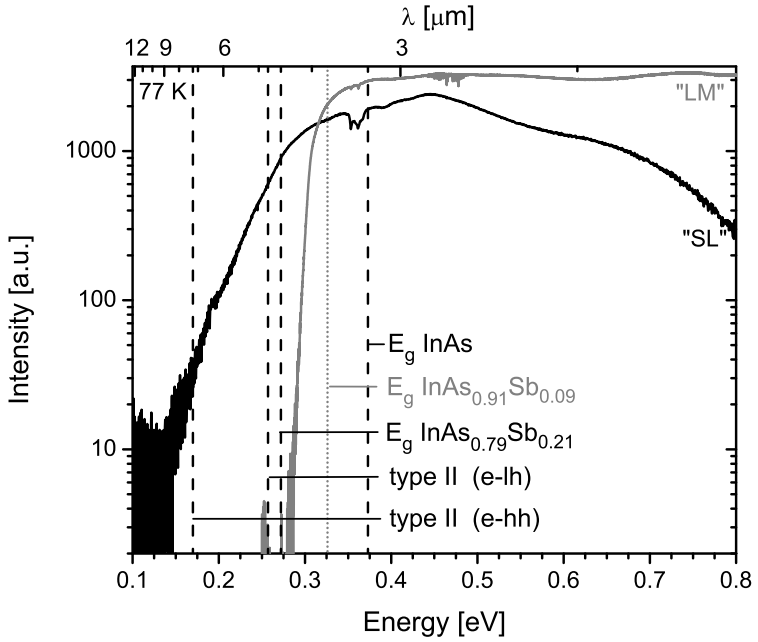

Figure 6.10: Optical response of a strain balanced $InAs_{0.79}Sb_{0.21}$/InAs SL detector ("SL") with a period of 40 nm. The significant sub-band gap response is due to the type II transitions. Due to the low matrix element , resulting from the long period, the type II response is very weak, as predicted (see Fig 6.8). For comparison, the response of an $InAs_{0.91}Sb_{0.09}$ n-p^+ homojunction lattice matched to GaSb ("LM") with a 1 μm thick absorber layer is shown in gray. The diameter of the circular aperture of this detector is 300 μm. Both measurements were done under zero bias condition. The calculated transition energies, shown as dashed vertical lines, include strain and quantization energies in all cases.

by the system response as measured with a HgCdTe photo-conductive detector. The SL detector shows, as predicted, a significant sub-bandgap signal. Its cutoff lies just below the predicted type II transition at 170 meV (7 μm). This cut-off energy is much lower than what can be reached by the lattice matched InAsSb composition at 280 meV (3.9 μm).

The response of the lowest type-II transition is significantly weaker than of the InAsSb direct transition due to the small matrix element of such a relatively large period SL (see Fig. 6.8b). Also below the band gap is the type II transition between the electrons in the InAs and light holes in the InAsSb (e-lh), which exhibits an overlap roughly 4 times larger than than the lowest type II (e-hh) transition. To increase the low energy signal the period of the SL needs to be decreased: i.e. a reduction from 40 nm to 20 nm should result in an order of magnitude intensity increase (see Fig 6.8b). The devices were measured under zero bias, as they suffer from a surface accumulation layer in the InAsSb which shunts the pn-junction and leads to large leakage currents under bias conditions. This can be avoided by either passivation of the surface or by changing to an InPSb heterojunction design (see Sec. 6.1). Overall, this unoptimized SL diode serves as proof of principal and the measured data is in good agreement with the predictions.

Chapter 7

Conclusions and Outlook

This thesis presented the first investigation of InAsSb/InAs type II superlattices for mid infrared optical detector applications. InAs/InAsSb single and multi quantum well structures and strain-balanced SL structures with InAsSb compositions of $0.04 \leq x_{Sb} \geq 0.27$ were grown by OMVPE on InAs and GaSb wafers without strain relaxation. Detailed XRD and electron microscopy measurements indicate good overall structural quality, but with some evidence of Ga and Sb memory effects attributed to susceptor carryover and surface segregation. 4 K PL from such structures was measured and the transition energies were compared to simulations made with energy band simulations using a simple effective mass approach for the carriers. By attributing 30% of the band-gap bowing parameter to the conduction band and 70% to the valence band, good agreement between theory and experiment was found. Further experimental evidence was gathered to support the theoretical prediction of the exact nature of the band lineup. The dependence of the PL energy versus InAsSb QW width supports the type IIb lineup, where the InAsSb conduction band is above the InAs conduction band. For the first time, the theoretical predicted type IIb band offset could be confirmed experimentally. The same set of parameters were then used to simulate the type II transition energies and transition matrix elements for a variety of InAsSb compositions and periods of InAsSb/InAs strain balanced SL absorber structures on GaSb at 77 K. Due to the lower band discontinuities between InAsSb and InAs compared to InAs/GaSb, higher matrix elements can be achieved for the same transition energies at longer period lengths. As a proof of concept, uncalibrated optical response data of an unoptimized $InAs_{0.79}Sb_{21}$/InAs strain balanced SL detector was presented with a cutoff very

close to the predicted type II transition energy of 170 meV (7 μm). The devices grown with a simple homojunction design were measured under zero bias, as they suffer from a surface accumulation layer in the InAsSb which shunts the pn-junction and leads to large leakage currents under bias conditions. It was shown that this problem can be overcome by changing to an InPSb/InAsSb heterojunction design. InAsSb detectors with InPSb top contact layers exhibited improved performance compared with InAsSb homojunction designs. The InAsSb/InAs strain balanced SLs is considered to be a promising alternative material system for infrared detection using III-V materials in the range of 2 μm to 20 μm, which are much more suitable for high volume production by OMVPE than the InAs/(In)GaSb material system.

Also it was shown, that the electrical behaviour of a n-InAsSb/n-GaSb junction can be tuned from rectifying to ohmic by increasing the GaSb doping level. Further it was shown, that for low GaSb doping levels, this junction behaves similar to a Schottky diode which can also be used as a GaSb photodetector. For high forward bias levels however, an optical response can also be measured from the InAsSb layer. This was explained by a simple model, and by measuring two different current directions for the response from the InAsSb and the GaSb layer, an earlier explanation [49] was ruled out.

As the SL simulations have shown, the SL detector structures achieved so far suffer from very small electron-hole wave function overlaps due to large layer widths. SL detector structures with a reduced period of 20 nm are predicted to improve the optical response by an order of magnitude. The heterojunction design needs to be grown with an improved SL absorber to show the full potential of this approach. Then, the detectivity of a certain wavelength needs to be measured, so the detector performance can be compared to the performance of InAs/GaSb short period superlattice and MCT detectors. Another way to increase the wave function overlap is to decrease the conduction band offset between the two alternating layers. This can be achieved by growing GaInAs instead of the InAs layers with low Ga contents. The GaInAs/InAsSb system can also be strain balanced on GaSb. It is also possible to use InPAs/InAsSb superlattices with low P contents instead. However, from a practical point of view, there is downside of having the superlattice consisting of two ternary layers: XRD-measurements alone are not sufficient to measure the composition of both ternary semiconductors and their thicknesses. At the same time, further research regarding the passivation of the InAsSb surface should be carried out, as promising

concepts have recently been published and should be tested on the homojunction detectors and on Hall samples. The greatest effect is expected on Hall samples. The passivation of the surface accumulation layer should enable the direct observation of p-type properties by eliminating the surface electron conduction channel. Passivation of the InAsSb surface should lead to a reduced dark current and thus an increased R_0A value of detector. Further, two reduce the dark currents, wide gap diffusion barrier layers on both sides of the p-n junction should be included.

Also the growth of InAsSb on exact GaSb substrates should be revisited, maybe with an improved reactor design, in order to minimize Sb carryover effects. Structurally higher quality material of InAsSb/InAs superlattice structures with lower surface roughnesses have recently been grown by Huang et al. in a close coupled showerhead reactor [9]. The heterojunction diode design allows for C-V and possibly also deep level transient spectroscopy measurements of the InAsSb material, which could give feedback on the possible relationship between growth conditions and concentrations of deep level defects and on the background doping level in the absorber layer.

The next step in the detector technology would be to fabricate two colour detectors by combining one SL detector with a bulk InAsSb lattice matched to GaSb, GaSb or another SL detector with a different cutoff, all grown in sequence on the same substrate. Two colour detection enables absolute temperature measurements of sources with unknown emissivity and further enables high-contrast imaging over a wide range of source temperatures.

Appendix A
Parameters used for nextnano^3 Simulations

Table 1: Parameters used for simulations. Parameters taken from Vurgaftman [4] unless stated otherwise. The bandgap (E_g) as function of temperature (T) is given in the Varshni form: $E_g(T) = E_g - \alpha T^2/(T+\beta)$. γ describes the linear expansion coefficient of the lattice parameter. For the ternary materials, the parameters entered are the non-zero bowing coefficients (c_{bow}) defined as: $Y(ABC) = xY_{AB} + (1-x)Y_{AC} - x(1-x)c_{bow}$. Note that parameters like band gap and carrier masses are regarding the Γ-point.

				bowing parameter	
	InAs	InSb	GaSb	InAsSb	InGaSb
a[Å]	6.0583	6.479	6.0959		
γ/(10^{-5} Å/K (T-300 K))	2.75	3.48	4.72		
E_g [eV]	0.417	0.235	0.812	0.67	0.415
α [meV/K]	0.276	0.32	0.417		
β [K]	93	170	140		
$E_{v,vac}$ [eV]	1.39[a]	1.75[a]	1.77[a]	-0.47[b]	
Δ_{so} [eV]	0.39	0.81	0.76	0.0[c]	0.1
m_e^*	0.026	0.0135	0.039	0.035	0.009
m_{hh}^*	0.41[d]	0.405[e]	0.34[e]		
m_{lh}^*	0.026[d]	0.016[d]	0.045[d]		0.011
a_c [eV]	-6.66[a]	-6.4[a]	-9.33[a]		
a_v [eV]	-1.0	0.31[f]	-1.32[a]		
b [eV]	-1.8	-2.0	-2.0		
d [eV]	-3.6	-4.7	-4.7		
c_{11} [GPa]	832.9	684.7	884.2		
c_{12} [GPa]	452.9	373.5	402.6		
E_p [eV]	21.5	23.3	27		

[a]Wei et al. [72] [c]Cripps et al. [46] [e]Landolt-Börnstein [73]
[b]present work [d]Yu and Cardona [74] [f]Qteish et al. [75]

Bibliography

[1] "NIST chemical database including IR absorption spectra: http://webbook.nist.gov/chemistry/,"

[2] A. Rogalski, J. Antoszewski, and L. Faraone, "Third-generation infrared photodetector arrays," *J. Appl. Phys.*, vol. 105, p. 091101, 2009.

[3] M. Razeghi, D. Hoffman, B.-M. Nguyen, P.-Y. Delaunay, E. K. Huang, M. Z. Tidrow, and V. Nathan, "Recent advances in LWIR type-II InAs/GaSb superlattice photodetectors and focal plane arrays at the Center for Quantum Devices," *PROC. IEEE*, vol. 97, p. 1056, 2009.

[4] I. Vurgaftman, J. R. Meyer, and L. R. Ram-Mohan, "Band parameters for III-V compound semiconductors and their alloys," *J. Appl. Phys.*, vol. 89, p. 5815, 2001.

[5] D. L. Smith and C. Mailhiot, "Proposal for strained type II superlattice infrared detectors," *J. Appl. Phys.*, vol. 62, p. 2545, 1987.

[6] E. H. Aifer, J. G. Tischler, J. H. Warner, I. Vurgaftman, W. W. Bewley, J. R. Meyer, J. C. Kim, L. J. Whitman, C. L. Canedy, and E. M. Jackson, "W-structured type-II superlattice long-wave infrared photodiodes with high quantum efficiency," *Appl. Phys. Lett.*, vol. 89, p. 053519, 2006.

[7] H. Mohseni, J. Wojkowski, M. Razeghi, G. Brown, and W. Mitchel, "Uncooled InAs-GaSb type-II infrared detectors grown on GaAs substrates for the 8-12 μm atmospheric window," *IEEE J. Quantum. Electron.*, vol. 35, p. 1041, 1999.

[8] Jmol:, "an open-source java viewer for chemical structures in 3d. http://www.jmol.org/,"

[9] Y. Huang, J.-H. Ryou, R. Dupuis, V. D'Costa, E. Steenbergen, J. Fan, Y.-H. Zhang, A. Petschke, M. Mandl, and S.-L. Chuang, "Epitaxial growth and characterization of InAs/GaSb and InAs/InAsSb type-II superlattices on GaSb substrates by metalorganic chemical vapor deposition for long wavelength infrared photodetectors," *J. Cryst. Growth*, vol. 314, p. 92, 2011.

[10] D. Lackner, O. J. Pitts, S. Najmi, P. Sandhu, K. L. Kavanagh, A. Yang, M. Steger, M. L. W. Thewalt, Y. Wang, D. McComb, C. R. Bolognesi, and S. P. Watkins, "Growth of InAsSb/InAs MQWs on GaSb for mid-infrared photodetector applications," *J. Cryst. Growth*, vol. 311, p. 3563, 2009.

[11] Z. M. Fang, K. Y. Ma, D. H. Jaw, R. M. Cohen, and G. B. Stringfellow, "Photoluminescence of InSb, InAs, and InAsSb grown by organometallic vapor-phase epitaxy," *J. Appl. Phys.*, vol. 67, p. 7034, 1990.

[12] Y. Guo, O. J. Pitts, W. Y. Jiang, and S. P. Watkins, "Numerical optimization of an optical showerhead reactor design for organometallic vapor phase epitaxy," *J. Cryst. Growth*, vol. 297, p. 345, 2006.

[13] G. B. Stringfellow, *Organometallic vapor-phase epitaxy : theory and practice*. Academic Press, San Diego, 2nd ed., 1999.

[14] G. Stringfellow, "Reaction mechanisms in OMVPE growth of GaAs determined using D2 labelling experiments," *Prog. Crys. Growth and Characterization*, vol. 19, p. 115, 1989.

[15] W. Burton, N. Cabrera, and F. Frank, "The Growth of Crystals and the Equilibrium Structure of their Surfaces," *Philo. Transac. Royal Soc. London A* , vol. 243, p. 299, 1951.

[16] R. M. Biefeld, "The metal-organic chemical vapor deposition and properties of III-V antimony-based semiconductor materials," *Mat. Sci. Eng. R*, vol. 36, p. 105, 2002.

[17] M. A. Herman, W. Richter, and H. Sitter, *Epitaxy - Physical Principles and Technical Implementation*. Springer Verlag, Heidelberg, 2004.

[18] B. E. Warren, *X-Ray Diffraction*, pp. 16–21. Dover Publications, Inc, New York, 1990.

[19] D. K. Bowen and B. K. Tanner, *High Resolution X-ray Diffractometry and Topography*. Taylor & Francis, London, 1998.

[20] D. K. Bowen and B. K. Tanner, *High Resolution X-ray Diffractometry and Topography*, p. 64. Taylor & Francis, London, 1998.

[21] D. K. Bowen and B. K. Tanner, *High Resolution X-ray Diffractometry and Topography*, p. 136. Taylor & Francis, London, 1998.

[22] B. E. Warren, *X-Ray Diffraction*. Dover Publications, Inc, New York, 1990.

[23] O. J. Pitts, *Growth and Characterization of Ultrathin InAs/GaAs and GaSb/GaAs Quantum Wells*. PhD thesis, Simon Fraser University, 2004.

[24] D. K. Schroder, *Semiconductor Material and Device Characterization*, p. 61ff. John Wiley & Sons, Inc. Hoboken, New Jersey, 3^{rd} ed., 2006.

[25] B. Streetman and S. Banerjee, *Solid State Electronic Devices*, pp. 202–205. Prentice Hall, New Jersey, 2000.

[26] J. Nelson, *The Physics of Solar Cells*, p. 151. Imperial College Press, London, 2003.

[27] A. Polyakov, M. Stam, A. Milnes, and T. Schlesinger, "Electrical properties of GaSb Schottky diodes and p-n junctions," *Mat. Sci. Eng: B*, vol. 12, p. 337, 1992.

[28] L. J. van der Pauw, "A method of measuring specific resistivity and hall effect of discs of arbitrary shape," *Philips Res. Repts.*, vol. 13, p. 1, 1958.

[29] D. K. Schroder, *Semiconductor Material and Device Characterization*. John Wiley & Sons, Inc. Hoboken, New Jersey, 2006.

[30] D. Karaiskaj, *Photoluminescence Studies of Isotopically Enriched Silicon*. PhD thesis, Simon Fraser University, 2002.

[31] M. Steger, "Impurity absorption spectroscopy of the deep double donor sulfur in isotopically enriched silicon," Master's thesis, Simon Fraser University, 2007.

[32] B. Fultz and J. Howe, *Transmission Electron Microscopy and Diffractometry of Materials*. Springer Verlag, Berlin Heidelberg New York, 2nd ed., 2002.

[33] K. M. Yu and M. Cardona, *Fundamentals of Semiconductors*, pp. 217–222. Springer, Berlin, 3rd ed., 2001.

[34] P. M. Petroff, R. A. Logan, and A. Savage, "Nonradiative recombination at dislocations in III-V compound semiconductors," *Phys. Rev. Lett.*, vol. 44, p. 287, 1980.

[35] J. W. Matthews and A. E. Bakeslee, "Defects in epitaxial multilayers: 1. misfit dislocations," *J. Cryst. Growth*, vol. 27, p. 118, 1974.

[36] R. People and J. C. Bean, "Calculation of critical layer thickness versus lattice mismatch for Ge_xsi_{1-x}/Si strained-layer heterostructures," *Appl. Phys. Lett.*, vol. 47, p. 322, 1985.

[37] T. Krug, L. Botha, P. Shamba, T. Baisitse, A. Venter, J. Engelbrecht, and J. Botha, "Electrical properties of undoped and doped movpe-grown InAsSb," *J. Cryst. Growth*, vol. 298, p. 163, 2007. Thirteenth International Conference on Metal Organic Vapor Phase Epitaxy (ICMOVPE XIII).

[38] A. Nedoluha and K. Koch, "Zum mechanismus der widerstandsänderung im magnetfeld," *Zeitschrift für Physik*, vol. 132, p. 608, 1952.

[39] V. W. L. Chin, R. J. Egan, and T. L. Tansley, "Carrier concentration and compensation ratio dependence of electron drift mobility in $InAs_{1-x}Sb_x$," *J. Appl. Phys.*, vol. 72, p. 1410, 1992.

[40] A. K. Srivastava, J. L. Zyskind, R. M. Lum, B. V. Dutt, and J. K. Klingert, "Electrical characteristics of InAsSb/GaSb heterojunctions," *Appl. Phys. Lett.*, vol. 49, p. 41, 1986.

[41] M. Mebarki, A. Kadri, and H. Mani, "Electrical characteristics and energy-band offsets in n-$InAs_{0.89}Sb_{0.11}$/n-GaSb heterojunctions grown by the liquid-phase epitaxy technique," *Solid State Commun.*, vol. 72, p. 795, 1989.

[42] D. Lackner, M. Martine, Y. T. Cherng, M. Steger, W. Walukiewicz, M. L. W. Thewalt, P. M. Mooney, and S. P. Watkins, "Electrical and optical characterization of n-InAsSb/n-GaSb heterojunctions," *J. Appl. Phys.*, vol. 107, p. 014512, 2010.

[43] O. Dier, C. Lin, M. Grau, and M. C. Amann, "Selective and non-selective wet-chemical etchants for GaSb-based materials," *Semicond. Sci. Technol.*, vol. 19, p. 1250, 2004.

[44] S. Sridaran, A. Chavan, and P. S. Dutta, "Fabrication and passivation of GaSb photodiodes," *J. Cryst. Growth*, vol. 310, p. 1590, 2008.

[45] nextnano^3, "http://www.nextnano.de/nextnano3/,"

[46] S. A. Cripps, T. J. C. Hosea, A. Krier, V. Smirnov, P. J. Batty, Q. D. Zhuang, H. H. Lin, P. W. Liu, and G. Tsai, "Midinfrared photoreflectance study of InAs-rich InAsSb and GaInAsPSb indicating negligible bowing for the spin orbit splitting energy," *Appl. Phys. Lett.*, vol. 90, p. 172106, 2007.

[47] C. G. Van de Walle, "Band lineups and deformation potentials in the model-solid theory," *Phys. Rev. B*, vol. 39, p. 1871, 1989.

[48] Y. Sharabani, Y. Paltiel, A. Sher, A. Raizman, and A. Zussman, "InAsSb/GaSb heterostructure based mid-wavelength-infrared detector for high temperature operation," *Appl. Phys. Lett.*, vol. 90, p. 232106, 2007.

[49] Y. Sharabani, Y. Paltiel, A. Sher, A. Raizman, and A. Zussman, "GaSb/InAsSb heterostructure MWIR detector for high temperature operation," vol. 6940, p. 69400D, SPIE, 2008.

[50] D. Lackner, O. J. Pitts, M. Steger, A. Yang, M. L. W. Thewalt, and S. P. Watkins, "Strain balanced InAs/InAsSb superlattice structures with optical emission to 10 μm," *Appl. Phys. Lett.*, vol. 95, p. 081906, 2009.

[51] S. H. Wei and A. Zunger, "InAsSb/InAs - a type-I a type-II band alignment," *Phys. Rev. B*, vol. 52, p. 12039, 1995.

[52] S. R. Kurtz and R. M. Biefeld, "Magnetophotoluminescence of biaxially compressed InAsSb quantum-wells," *Appl. Phys. Lett.*, vol. 66, p. 364, 1995.

[53] P. J. P. Tang, M. J. Pullin, Y. B. Li, C. C. Phillips, R. A. Stradling, S. J. Chung, W. T. Yuen, L. Hart, D. J. Bain, and I. Galbraith, "A magneto-photoluminescence investigation of the band offset between InAs and arsenic-rich $InAs_{1-x}Sb_x$ alloys," *Appl. Phys. Lett.*, vol. 69, p. 2501, 1996.

[54] S. Kurtz, L. Dawson, R. Biefeld, D. Follstaedt, and B. Doyle, "Ordering-induced band-gap reduction in $InAs_{1-x}Sb_x$ (x-approximate to 0.4) alloys and superlattices," *Phys. Rev. B*, vol. 46, p. 1909, 1992.

[55] T. Y. Seong, G. R. Booker, A. G. Norman, and I. T. Ferguson, "Atomic ordering in molecular-beam epitaxial $InAs_ySb_{1-y}$ natural strained-layer superlattices and homogeneous layers," *Appl. Phys. Lett.*, vol. 64, p. 3593, 1994.

[56] P. J. P. Tang, M. J. Pullin, S. J. Chung, C. C. Phillips, R. A. Stradling, A. G. Norman, Y. B. Li, and L. Hart, "4-11 μm infrared-emission and 300 K light-emitting-diodes from arsenic-rich $InAs_{1-X}Sb_x$ strained-layer superlattices," *Semicond. Sci. Technol.*, vol. 10, p. 1177, 1995.

[57] K. Alberi, J. Wu, W. Walukiewicz, K. M. Yu, O. D. Dubon, S. P. Watkins, C. X. Wang, X. Liu, Y. J. Cho, and J. Furdyna, "Valence-band anticrossing in mismatched III-V semiconductor alloys," *Phys. Rev. B*, vol. 75, 2007.

[58] C. E. Pryor and M. E. Pistol, "Band-edge diagrams for strained III-V semiconductor quantum wells, wires, and dots," *Phys. Rev. B*, vol. 72, p. 205311, 2005.

[59] P.-W. Liu, G. Tsai, H. H. Lin, A. Krier, Q. D. Zhuang, and M. Stone, "Photoluminescence and bowing parameters of InAsSb/InAs multiple quantum wells grown by molecular beam epitaxy.," *Appl. Phys. Lett.*, vol. 89, p. 201115, 2006.

[60] S. Adachi, *Properties of Group-IV, III-V and II-V Semiconductors*, p. 196. John Wiley & Sons Ltd, Chichester, 2005.

[61] L. O. Bubulac, A. M. Andrews, E. R. Gertner, and D. T. Cheung, "Backside-illuminated InAsSb/GaSb broadband detectors," *Appl. Phys. Lett.*, vol. 36, p. 734, 1980.

[62] A. Krier and W. Suleiman, "Uncooled photodetectors for the 3–5 μm spectral range based on III–V heterojunctions," *Appl. Phys. Lett.*, vol. 89, p. 083512, 2006.

[63] M. Carras, J. L. Reverchon, G. Marre, C. Renard, B. Vinter, X. Marcadet, and V. Berger, "Interface band gap engineering in InAsSb photodiodes," *Appl. Phys. Lett.*, vol. 87, p. 102103, 2005.

[64] O. Pitts, D. Lackner, Y. Cherng, and S. Watkins, "Growth of InAsSb/InPSb heterojunctions for mid-IR detector applications," *J. Cryst. Growth*, vol. 310, p. 4858, 2008.

[65] A. Rogalski, *Infrared Detectors*. CRC Press, Amsterdam, 2000.

[66] L. F. J. Piper, T. D. Veal, M. J. Lowe, and C. F. K. K. McConville, "Electron depletion at InAs free surfaces: Doping-induced acceptorlike gap states," *Phys. Rev. B*, vol. 73, p. 195321, 2006.

[67] I. Shafir, M. Katz, A. Sher, A. Raizman, A. Zussman, and M. Nathan, "Suppression of leakage currents in InAsSb MWIR photodiodes by chemical treatment and illumination," *Semicond. Sci. Technol.*, vol. 25, p. 045004, 2010.

[68] H. Shao, W. Li, A. Torfi, D. Moscicka, and W. Wang, "Room-temperature InAsSb photovoltaic detectors for mid-infrared applications," *Photon. Technol. Lett. IEEE*, vol. 18, p. 1756, 2006.

[69] A. Rakovska, V. Berger, X. Marcadet, B. Vinter, G. Glastre, T. Oksenhendler, and D. Kaplan, "Room temperature InAsSb photovoltaic midinfrared detector," *Appl. Phys. Lett.*, vol. 77, p. 397, 2000.

[70] C. Weisbuch and B. Vinter, *Quantum Semiconductor Structures*, pp. 57–60. Academic Press, San Diego, 1991.

[71] J. Roslund and T. Andersson, "Tailoring InAs/$Ga_{1-x}In_xSb$ superlattices for long-wavelength IR applications," *Superlattices Microstruct.*, vol. 16, p. 77, 1994.

[72] S. Wei and A. Zunger, "Calculated natural band offsets of all II-VI and Ill-V semiconductors: Chemical trends and the role of cation d orbitals," *Appl. Phys. Lett.*, vol. 72, p. 2011, 1998.

[73] O. Madelung, ed., *Landolt-Boernstein – Physics of Group IV Elements and III-V Compounds*, vol. 17. Springer, Berlin, 1982.

[74] P. Yu and M. Cardona, *Fundamentals of Semiconductors*, p. 75. Springer, Berlin, 3rd ed., 2001.

[75] A. Qteish and R. J. Needs, "Improved model-solid-theory calculations for valence-band offsets at semiconductor-semiconductor interfaces," *Phys. Rev. B*, vol. 45, p. 1317, 1992.